INVESTIGATING THE INFLUENCE OF THERMOMECHANICAL VARIABLES ON RIDGING IN AISI 430 STAINLESS STEEL

A dissertation submitted to the Faculty of Engineering of the University of Cape Town, in fulfilment of the degree of Masters of Science in Applied Science.

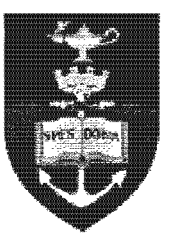

By

Ryan Matthews

Centre for Materials Engineering

Mechanical Engineering

2001

ABSTRACT

The phenomenon of ridging is known to occur in most ferritic stainless steels and is manifested during deformation of sheet material. It results in the formation of a corrugated profile with ridges always elongated in the rolling direction of the sheet and are typically around 1 mm in wavelength. The formation of a ridged profile, while not having a detrimental effect of the mechanical properties, results in the product having an unattractive surface finish. Thus there is a drive to find a thermomechanical process to minimise the severity of ridging in the final sheet product. In this regard, the purpose of this investigation was to establish the influence of three thermomechanical (TMP) variables on the ridging severity. The samples in this investigation represented: two zones of the initial starting structure, with equiaxed or columnar grains; four hot rolling finish temperatures (HRFT), 700°C, 800°C, 900°C and 1000°C; and two cooling methods after hot rolling, quench and slow cool verses slow cool. Each sample completed the TMP cycle, was elongated to 20% strain and the topography on the surface measured and compared.

There is still debate around the underlying mechanism, but there is general agreement that ridging is due to differential strains in the material. Bands composed of many grains, elongated in the rolling direction, which contain textures and/or grain sizes that are different to the homogeneous matrix, are thought to be the cause of these differential strains. It was necessary to compare the ridging results of the samples with their components in their microsturcture to understand the influence of the TMP variables on ridging. Electron back-scattered diffraction was used to identify the ridging constituents in the microstructures and to quantitatively compare them. In the samples with greatest ridging severity, bands of grains with similar grain size as well as bands of similar Taylor factors were observed. Both types of bands and their associated difference in calculated yield strengths to the matrix, satisfy the requirements, with present understanding, of the ridging mechanism. It was noted that ridging severity is dependent not only on the severity of banding but also on the distribution of banding.

The difference in HRFT had the most profound effect on ridging, with the surface quality improving as HRFT increased. As the HRFT increased there was increased

martensite content in the material as it was cold rolled. Martensite, being harder, partitions strain energy to the ferrite regions resulting in a more random orientation distribution in the final material. The equiaxed samples consistently had a better surface quality than the columnar samples. The finer starting structure resulted in higher frequency distribution of austenite and subsequent martensite after cooling from hot rolling. This resulted a finer distribution of heterogeneous bands in the final annealed material. The different cooling methods had no effect on ridging severity.

ACKNOWLEDGEMENTS

I suspect that I would presently be fumbling around the laboratory with a useless project and would not have much hope for the future, had I not received the support that I was blessed with during the past two years. In this regard I sincerely thank the following:

The Lord Jesus for giving me a life, and one with many gracious blessings.

My supervisor, Prof. Rob Knutsen, who has been a great teacher and inspirer while being patient and approachable.

Glen Newins, Mira Topic, Adriaan Loedolf and James Peterson for their excellent technical assistance.

Dane and Miranda together with the rest of the staff at the Electron Miroscope Unit, who have given me valuable knowledge about, and experience on, the SEM.

The NRF, their financial support is greatly appreciated.

Columbus Stainless who have sponsored the project and the assistance of Lucien Matthews and Bruce Muller for the sample preparation is acknowledged.

The students of the Centre of Materials who have been great study companions, and have amongst them a good mix of computer and problem solving skills, gifts of encouragement and superlative humour.

Annie, Blanche, Paul and Simon for proof reading together with the chaps at Two Bare Feet for being great digsmates.

My folks for always being very encouraging and supportive, this goes to you...

TABLE OF CONTENTS

SYMBOLS AND ABBREVIATIONS

BCT – Body-centered-tetragonal.

FCC – Face-centered-cubic.

BCC – Body-centered-cubic.

UTS – Ultimate tensile strength.

M_s – Martensitic start temperature.

M_f – Martensitic finish temperature.

SFE – Stacking fault energy.

γ-loop – Austenite region in Cr-Fe phase diagram

RD – Rolling direction.

TD – Transverse direction.

ND – Normal direction.

R – Strain ratio

HRFT – Hot Rolling Finish Temperature.

TMP – Thermomecanical Process.

SEM – Scanning electron microscope.

ECC – Electron channelling contrast.

EBSD – Electron back-scattered diffraction.

ODF – Orientation distribution function.

1 INTRODUCTION

AISI 430 stainless steel is the most widely used grade of ferritic stainless steels, with applications such as kitchen sinks, washing machines and automobile trimmings, all formed from sheet material. This grade is chosen for these products because it displays good corrosion resistance, adequate formability and is significantly cheaper than its austenitic counterparts. A problem arises, though, when a sheet of 430 is strained during forming as it tends to form a corrugated profile with surface ridges running parallel to the rolling direction. This so-called ridging, while not having a detrimental effect on the mechanical properties, results in an unattractive surface finish.

Research has been published since the late 1950's where models of the ridging mechanism started to be proposed. Yet, still these models are presently being refined with the view to obtaining the definitive ridging model. Technology limited those pioneer researchers who had to extrapolate their results to gain a model of the ridging phenomenon. Today better technology, such as automated electron back-scattered diffraction, which gives spatial orientation information from the microstructure, has enabled this problem to be further investigated.

This investigation aims at observing and understanding various thermomechanical variables on the ridging results of the final sheet product. The three variables are:

- Starting structure; with samples of either completely columnar or equiaxed grains entering the hot roll stage.
- Hot rolling finish temperature; temperatures chosen were 700°C, 800°C, 900°C, 1000°C.
- Cooling rates after hot rolling; either slow cooling or a short quench followed by a slow cool, the latter simulating a water spray in the plant.

The starting structures from the slab were isolated to see how each, with their different starting grain sizes, shapes and orientations, affect the ridging results of the sheet product. The second two variables were introduced to vary the stored deformation energy within the microstructure and observe the effect thereof. Varying the hot rolling temperature also influenced the phases present in the steel.

The experimental matrix was large with a total of 16 samples investigated. The strategy employed, in view of this, was to first observe the ridging severity of each sample and then to concentrate the investigation on some selected samples. Using these samples the investigation would work backward through the thermomechanical route to trace the evolution of the final microstructure that led to the ridging observed.

2 LITERATURE REVIEW

2.1 Introduction to AISI 430 Stainless Steel

When attempting to solve a single problem in a material, a collection of unfavourable influences may result if not all its properties, uses and advantages are considered in their entirety before tackling the problem at hand. Such a solution is not a progressive one. Thus before the specific problem of surface roughening in 430 stainless steel is discussed, the context of this grade of stainless steel in relation to others must be considered.

A discussion follows which attempts to place the grade of stainless steel concerned in this project in its context, and will highlight its uniqueness and advantages for its present applications.

2.1.1 Stainless Steel

Stainless steel is the class of ferrous metals that have the advantage, through the major alloy addition of chromium, of being resistant to the crippling effects of corrosion. The chromium content is generally above 12wt% and with other alloying elements can produce a series of stainless steels resistant to attack by atmospheric oxygen, aqueous solutions, chlorides as well as more aggressive attack by acids or alkalis[1]. The corrosion protection offered by chromium is by means of an adhering, self healing impenetrable layer of chromium oxide which forms on the surface.

A historical date cannot be quoted as the discovery of stainless steel. They rather evolved as the product of 90 years of experimentation[2]. It was the work of Berthier in 1821 who first observed that a steel with the significant addition of chromium, increased its resistance to acids[2]. He obtained this material by reducing a combination of ferrous and chromium oxides. At that time, however, the carbon content of the steels was too high, and an optimum chromium content that gave good corrosion resistance while still maintaining formability had not been

discovered[2]. It was the lack of successful alloys and inadequately defined corrosion testing that discouraged scientific research into this seemingly futile field[2].

Much later, between 1900 and 1915, stainless steels were discovered almost simultaneously by several metallurgists[2]. The catalyst to this discovery was probably the development of the alumino-thermical technique by the German H. Goldschmidt for preparation of low-carbon ferro-chromium as well as chromium metal[2]. Goldschmidt and fellow countryman W. Giessen, as well as other French metallurgists L. Guillet and A. Portevin, all made very significant contributions to the research into these new low carbon chromium rich steels. Together, by 1909, their combined research enabled the three main classes of stainless steels to be identified according to their structure. These are the martensitic, austenitic and ferritic structures.

2.1.2 Martensitic Stainless Steels

The martensitic family offers a steel with a good combination of high strength, and corrosion resistance[2]. Good mechanical strength is an inherent quality of the body-centered-tetragonal (BCT) structure which offers a high resistance to dislocation mobility. Its corrosion resistance is obtained by the significant addition of chromium.

Their typical composition contains 12-18% Cr, 0.1-1.0% C as well as other small additions of Ni, Mo, V, Nb, Al, Ti, Cu, and Si[2,3]. The carbon percentage is relatively high but is necessary for the phase transformation from austenite, which has a face-centred-cubic structure (FCC), to the metastable martensite phase. When the steel is cooled sufficiently fast, the carbon is prevented from diffusing out of solution preventing the stable transformation to ferrite. Ferrite cannot hold as high a carbon content in solution as austenite. The trapped carbon causes the FCC structure to shear to BCT, with an accompanied increase in volume[2]. This transformation from the martensitic start temperature (M_s) to the finishing temperature (M_f) is temperature and not time dependent[2]. This allows material with large section sizes to be transformed fully to the martensitic phase[3].

The mechanical strength of this group of stainless steels is its best quality, and thus should be optimised. To ensure this, the structure of the material must be completely austenitic before cooling, in order for a fully hardened martensitic structure to result. Carbon here acts as a cheap austenite former to extend the gamma loop to higher Cr levels in the Fe-Cr binary phase diagram[3]. Its use is restricted because it reduces the weldability, the toughness as well as the corrosion resistance of the steel[3]. Nickel, although a lot more expensive, is a powerful austenite former without the associated embrittling effect as with carbon and is used up to 4.0%[3]. The effects of both carbon and nickel on the extension of the gamma loop are shown in Figure 2 below. To reduce the loss of strength while tempering, additions of Mo and V are used which are ferrite formers and thus must be compensated for when considering their effect on the gamma loop[3]. A subset within the martensitic steels are the age-hardened steels, which gain greater hardness by the age-hardening precipitation effects from additions such as copper[2].

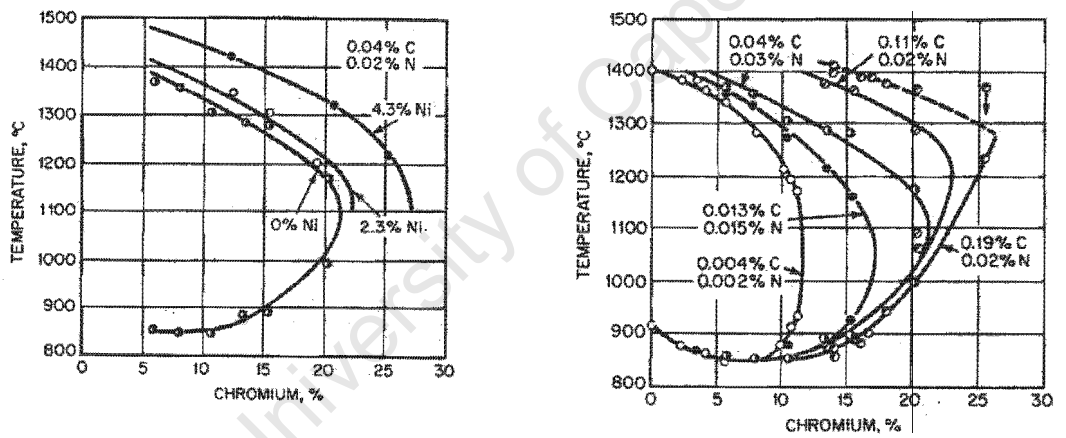

Figure 1 Effect of austenite formers (a) nickel and (b) carbon on the gamma loop in Fe-Cr phase diagram[4].

These steels are chosen for applications where moderate corrosion resistance, strength and fatigue resistance is required. Such applications include bolts and machine parts, springs, hand tools and knife blades[5]. With their high hardness, they can also be used where abrasion and wear resistance is required such as valve parts and equipment for coal mining[5].

2.1.3 Austenitic Stainless Steels

This family has by far the highest production of all the fundamental types of stainless steel[1]. The addition of 8-20% Nickel with the high chromium content of 18-25% make these grades more expensive than others that contain significantly less nickel[3]. Nickel serves a twofold purpose in the steel, firstly to expand the gamma loop resulting in a higher percentage of austenite at the solution treated temperature, and secondly to lower the M_s[3]. If the M_s is below room temperature, to which the steel is to be cooled, then stable austenite will be the room temperature structure[3].

Austenite is a FCC structure that gives the steel its unique properties. It does not experience a ductile to brittle transition temperature like its ferrite counterpart. Therefore low temperature applications such as liquefied gas storage tanks are possible using austenitic grades[2]. These steels are also more suited to higher temperature applications because of their higher intrinsic creep strength compared with ferrite[2]. FCC steel has a lower stacking fault energy (SFE) than BCC steel. Dislocations tend to separate into two partial dislocations when the SFE is low, producing a stacking fault separating the two partials. These partial dislocations cannot readily slip past each other or cross-slip to adjacent planes. Consequently, dislocations pile-up at crystal boundaries giving austenitic steels a high work hardening potential[3].

After cooling from a solution treatment, these steels are softer than the other martensitic and BCC structures, due to the low dislocation glide friction of the FCC structure. The strength, however, may be vastly improved by three independent methods. Firstly, solid solution strengthening by alloying elements has an important strengthening effect especially the interstitial elements of nitrogen, carbon and boron[2]. The effect of relative amounts of these constituents on their proof stress can be seen in Figure 2 below. These elements produce lattice distortions that pin dislocations and inhibit their movement[2].

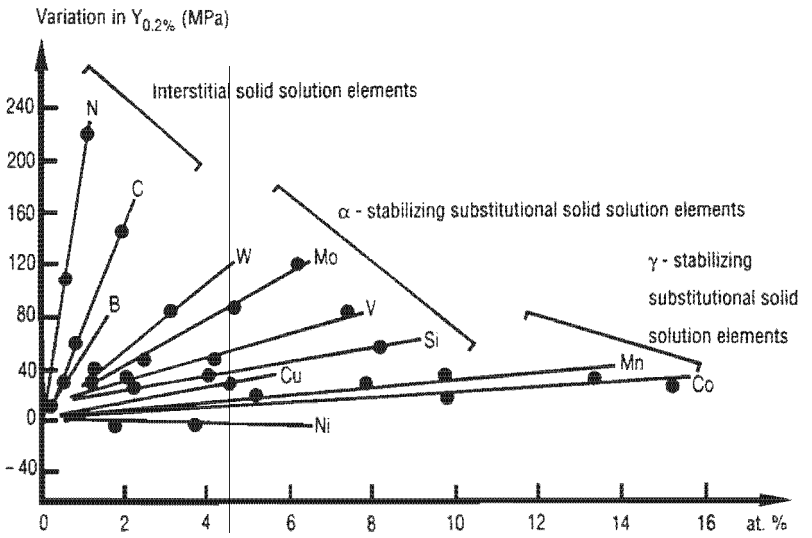

Figure 2 Effect of solid solution strengthening in austenite[2].

Secondly these steels lend themselves very favourably to being cold worked. They are able to be elongated by a percentage twice that of ferritic steels while work hardening to strengths beyond those typical of ferritic stainless steels, as shown in Figure 3 below[1]. The major contributor to the strength in the cold worked state is the formation of deformation induced martensite[4]. The amount of martensite produced by deformation is dependent upon the stability of the austenite at ambient temperature[3]. Increasing the nickel content would further stabilise the austenite. The third useful method of strengthening austenitic stainless steels is by introducing fine intragranular precipitates. High carbon contents as well as cold work encourage precipitation of $M_{23}C_6$ carbides at nucleation sites such as stacking faults[2,4].

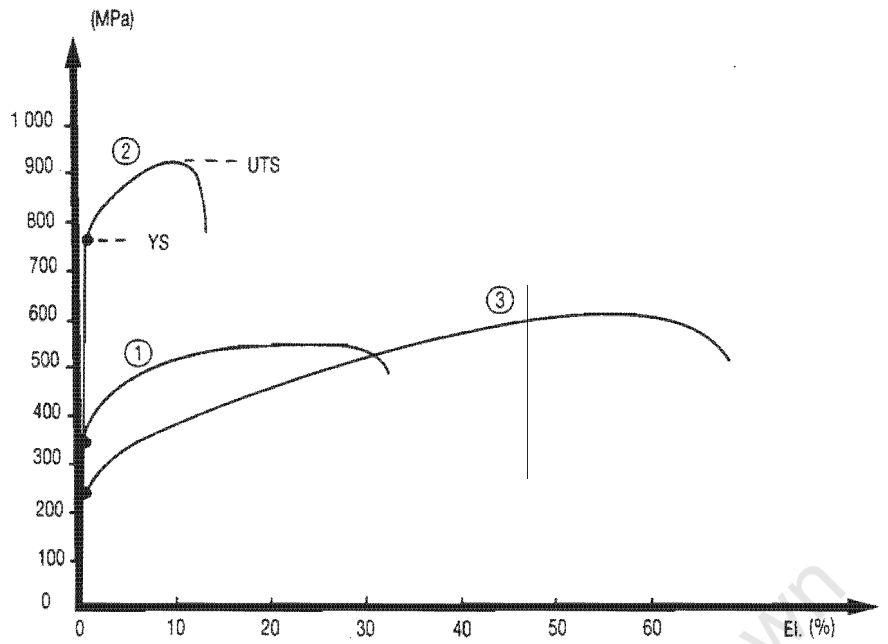

Figure 3 A comparison of tensile curves for (1) AISI 430 steel in annealed condition, (2) AISI 420 martensitic steel treated to obtain a hardness of 940 Mpa and (3) AISI 304 in a solution treated condition[2].

Within the austenitic family there are many subgroups of steels, differentiated according to their composition for their specific applications[2]. Relatively high nickel grades are used for cryogenic applications and deep drawability while a lower nickel content encourages work hardening[2].

The austenitic family has the advantage of being the most corrosion resistant of all stainless steels due to their high chromium and nickel contents[4]. They are ductile but have the ability to be strengthened above typical ferritic strengths. Both low and high temperature applications are possible using the steels from this family. The specific applications are too numerous to mention, but the major drawback with these steels is their expense. Nickel is the constituent that results in high prices since it is roughly four times as much as the second most expensive major alloying element, chromium[6].

2.1.4 Ferritic Stainless Steels

With little to no nickel present, this family becomes a cheaper alternative to austenitic grades. The ferrite structure is obtained by the exclusion of nickel and low percentages of carbon (<0.08%) which are both strong austenite formers[1]. It can be maintained throughout all temperature ranges encountered, though, with some compositions, the γ-loop is entered at high temperatures[2]. The chromium contents vary in these steels from 12% to 28%[2]. The most commonly produced ferritic stainless steel is the AISI 430 grade which has a chromium content of 17%[2]. Molybdenum can be added to improve the stability of the chromium oxide passive film[3]. Titanium and niobium complement the ferrite formation together with chromium, and are added in some grades as strong ferrite formers. They remove interstitial elements from solution, which in turn protects the steel against intergranular corrosion as well as improving the ductility[3].

Ferrite has a body-centered-cubic structure. This structure has no truly close-packed planes and has a low packing factor of 0.68 as opposed to FCC with a packing factor of 0.74[7]. Forty-eight slip systems are operational on planes that are nearly close packed. Without close-packed planes, the critical resolved shear stress for BCC is typically one magnitude greater than for FCC[7]. Thus ferrite usually has a higher yield point than austenitic structures[7].

The gamma loop's extension towards higher chromium levels is retarded due to the low content of the austenite formers, carbon and nitrogen, both kept typically under 0.1%. Quench hardening of ferritic stainless steels may only cause a small increase in hardness due to a small, if any, portion of the material transforming from austenite, in the dual phase region to martensite[4]. The ferrite matrix has a very low solubility for interstitial elements such as carbon and nitrogen and they will precipitate out as carbides predominantly at the grain boundaries[4]. This reduces the ductility of the steels.

The major disadvantage of these steels is the embrittling effects that they display. Grain coarsening is rapid in ferritic stainless steels at high temperature when compared to austenitic grades since the mobility of grain boundaries is greater in BCC structures, starting to coarsen at around 600°C compared with 900°C for

austenite[3]. This can become problematic in the heat affected zone around a weld for example[1]. Therefore only thinner sections of these steels may be welded, to ensure rapid cooling of the zone. This prevents excessive grain growth and carbon segregation to grain boundaries, which both lead to a brittle structure. Thus the Ti and Nb stabilised steels are better for welding purposes[3]. Slip in BCC structures is dependent on thermal energy to overcome the jump distance and this leads to another embrittling effect, the ductile to brittle transition. This occurs at a particular temperature where slip no longer is thermally activated rendering these steels unsuitable for low temperature applications. The transition temperature, however, is significantly reduced by decreasing the carbon content[2]. There is also an effect known as 475°C embrittlement, for which several proposed theories attempt to explained[3,4]. However, as in the other embrittlement problems, a reduction in interstitial contents reduce the severity of this problem[3].

With the embrittling effects aside, the ferritic stainless steels have the advantage of having good corrosion resistance, strength with large measure of ductility, and are resistant to stress corrosion cracking[4]. The latter being a major advantage over its austenitic counterparts.

2.1.5 AISI 430 Stainless Steel

This grade is the most widely used of the ferritic family. With good corrosion resistance, the reasonable formability and its affordability, this steel has become important for cold drawn products[1]. It is selected for applications such as kitchen sinks, catering equipment, washing machines and automobile trimmings[3,4]. Due to its susceptibility to intergranular corrosion it is not selected for parts that require welding, neither is it chosen for structural applications due to its poor toughness[3]. The titanium and niobium stabilised ferritic steels are selected above 430 for welding applications. The phase diagram for this steel is shown below in Figure 4.

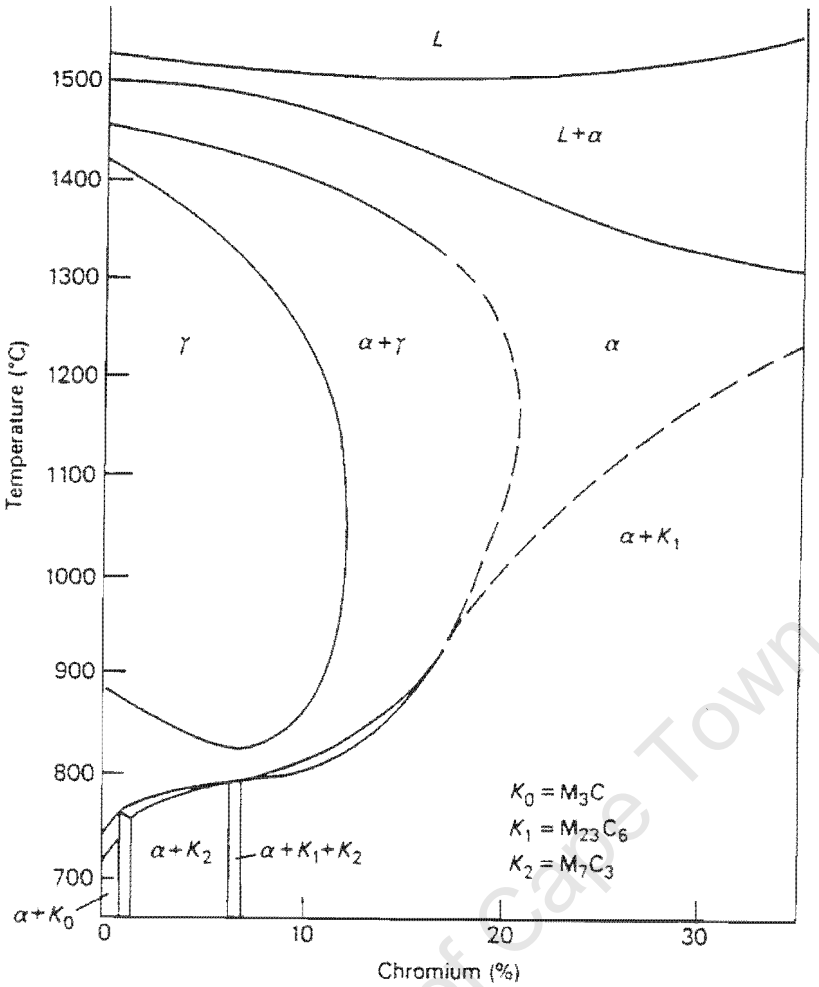

Figure 4. Phase diagram for a typical AISI 430 stainless steel with 0.05 wt% C[4].

An important property of the steel is its high SFE. This high SFE prevents dislocations from separating to two partials and allows the dislocations to cross-slip across planes, when thermally activated during annealing. With this mobility they are able to glide and entangle themselves producing cell walls. This arrangement of dislocations into cell walls has a lower energy configuration than a random distribution after straining and thus it can recover induced strain energy. This process described above is called recovery and is the preferred mode of stress relaxation in these steels[8]. In an investigation of the hot band annealing behaviour, an AISI 430 steel was observed to recover without fully recrystallizing once subjected to 95% rolling reduction finishing at 800°C and annealing temperature of 840°C for 6 hours[9]. In order for recrystallization to occur there must be a higher strain driving force. The structure has a very low interstitial solubility for carbon and nitrogen compared to FCC structures and these elements can diffuse through the lattice with relative ease even at room temperature[2].

force. The structure has a very low interstitial solubility for carbon and nitrogen compared to FCC structures and these elements can diffuse through the lattice with relative ease even at room temperature[2].

2.2 Ridging and Roping in AISI 430

2.2.1 Introduction

The terms ridging and roping have been used interchangeably[10,11] to describe the same surface roughness phenomenon found in ferritic stainless steels[12]. Although 'roping' has become less frequently used over the last decade. These steels are principally used for applications where the aesthetics of the product are important, for example a hubcap of a motorcar, therefore a severely ridged surface is unacceptable. The uneven reflections are caused by the undulating ridged profile, with the product having to be subjected to expensive grinding and buffing for the surface to regain its smooth, attractive appearance[12]. Besides the poor appearance, the material would otherwise satisfy the requirements of corrosion resistance, toughness, and formability with the advantage of being cheaper than the austenitic grades that could be used.

The ridges have a wavelength typically of the order of a millimetre, a peak to trough height of around 50μm in severe cases. The undulations always run parallel to the rolling direction (RD) because it is during the rolling procedure that the constituents for ridging are created within the microstructure[12]. The ridges form a corrugated profile where the peaks on one surface correspond with the troughs of the other surface[11]. No strength is lost in a corrugated sheet because there is no localised necking.

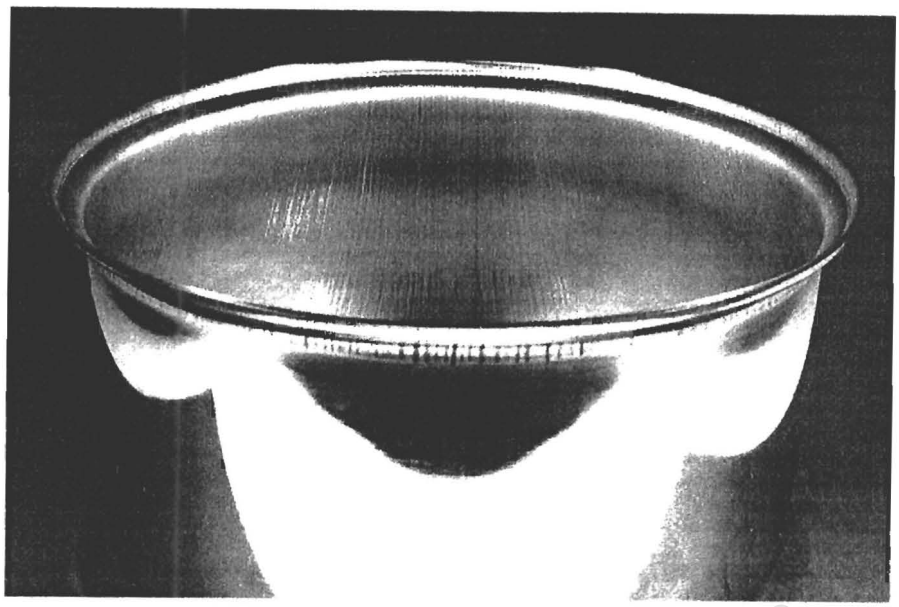

Figure 5. A deep-drawn pot with ridging on the inside and rims. The ridging has been buffed away on the outer surfaces.

As the material is strained at different angles to the RD, the ridging still develops parallel to the RD but the severity decreases as the direction of tensile straining deviates away from the RD[13,14].

With closer inspection of the ridged profile, smaller elongated undulations have been observed superimposed on the large visible ridges[15,16,17]. These smaller ridges are on a micrometer scale but are still too large to be attributed to the effects of single grains[16]. They may be due to collections of grains in the material that act together during deformation to form a single micro-ridge. The macro-ridges may be the observed net effect of a multitude of such collections of grains distributed in the bulk material[17], or an entirely different cause altogther[16].

Figure 6. Schematic showing the superposition of different frequencies of undulations observed.

Ridging is different from other surface roughening effects such as the orange peel effect. Whereas the orange peel effect is due to individual grain rotations on the surface, the topography of ridging is widely accepted to be due to heterogeneous strains[12,11]. There is some debate around what causes this behaviour, but the most convincing evidence lies in the effects of the heterogeneous texture distribution in the material, this detailed in the following section 2.3. Long colonies of grains, elongated in the RD, with a preferred orientation (texture) are found in these steels[18]. Each colony having a different straining behaviour dependent on its preferred orientation.

To aid understanding of the occurrence of the ridging phenomenon in this steel, its properties must be examined to find what makes it unique when compared to other non-ridging ferritic steels with a similar structure. Takechi points out that this steel, together with the properties inherent of other BCC structures, has a ferrite-austenitic transformation that plays a role in the thermal history of sheet products[21]. Another property is the steel's greater density of precipitates that form at a high dissolution temperature[21].

Research has been conducted since the 1960's to understand the mechanism involved and thus try to solve the ridging problem, which at that time became of economical importance. Although much research has been conducted on this topic, some say that ridging and roping is an inherent problem that can only be minimised but never fully eliminated[19].

2.3 Proposed Ridging Models

This section outlines the models that were proposed through time to understand the mechanism that produces ridging.

2.3.1 Mechanism by Chao

In 1967 Chao proposed the first mechanism to explain the ridging phenomenon. He explained the formation of the ridges by considering the plastic strain ratios of the different texture components measured in the sheet[20]. Below is the equation defining the plastic strain ratio, R.

Equation 1 $$R = \frac{\varepsilon_{TD}}{\varepsilon_{ND}}$$

Where TD is the transverse direction and ND is the normal direction to the sheet.

Existing data available to Chao suggested that there were three main texture groups found in commercial ferritic stainless steels. They are definited according to their orientations given below.

CC (cube-on-corner) → mainly {111}<011> and {111}<112> orientations,
CE (cube-on-edge) → {011}<001> orientation,
CF (cube-on-face) → {001}<011> amongst other similar orientations.

The R values for each of the three above groups were calculated using Schmid's law for uniaxial tension in the RD, neglecting any lattice rotation. The findings for each of the three groups of textures are given below.

CC → R = 2 to ∞ depending on which slip planes will be favoured,
CE → R = 1, isotropic flow,
CF → R = 0, i.e. no deformation would occur in the transverse direction.

The plastic strain calculations revealed a significant difference in plastic strain behaviour between the three different textures. Chao argued that this difference in

R values was not in itself sufficient to explain the ridging effect. Chao argued that the yield point values of each texture must accompany the R values, since one texture may yield at a much lower stress than another texture. The yield point will effect the amount of strain each texture will experience. Therefore, the relative yield points for each of the texture groups using the resolved shear stress and Schmid's law were calculated. The yield points are dependent upon the direction that slip would occur. The results of the calculations are given below. The symbol, σ_{hkl}, is the yield stress when uniaxial load is applied in the [hkl] direction (the rolling directions for CE are [001], and for CC and CF are [011]), and τ_{111} is the shear stress for yielding on the slip systems which each act in the [111] direction.

$$\text{CE} \rightarrow \sigma_{001} = \sqrt{6}\,\tau_{111} = 2.45\tau_{111},$$

The above calculation is true for both single and polycrystalline specimens since the CE orientation always flows isotropically. Below is the calculation for anisotropic flow for both the CC and CF orientations.

$$\text{CC and CF} \rightarrow \sigma_{011} = \sqrt{6}\,\tau_{111} = 2.45\tau_{111},$$

Yet the CC and CF orientations, when in a polycrystalline material, will not always flow anisotropically. The boundary induced stress from neighbouring grains impedes anisotropic flow, and with the threshold stress of approximately 50% and greater than the anisotropic shear stress, isotropic flow will be induced.

Therefore, initially as the stress is applied there would be anisotropic flow in CC and CF regions while in the regions of CE isotropic flow will occur. As the stress increases, a point will be reached where all parts of the material will flow isotropically. Chao thus postulates that during the anisotropic flow stage the differential strains cause ridging but once the whole of the material flows isotropically the severity of the ridging will not increase.

According to Chao, whenever there is a strong CF or CE texture, distributed as clusters of grains elongated in the RD in a predominantly CC matrix, then ridging will

occur due to plastic anisotropy. Below is a simplified diagram to explain the mechanism.

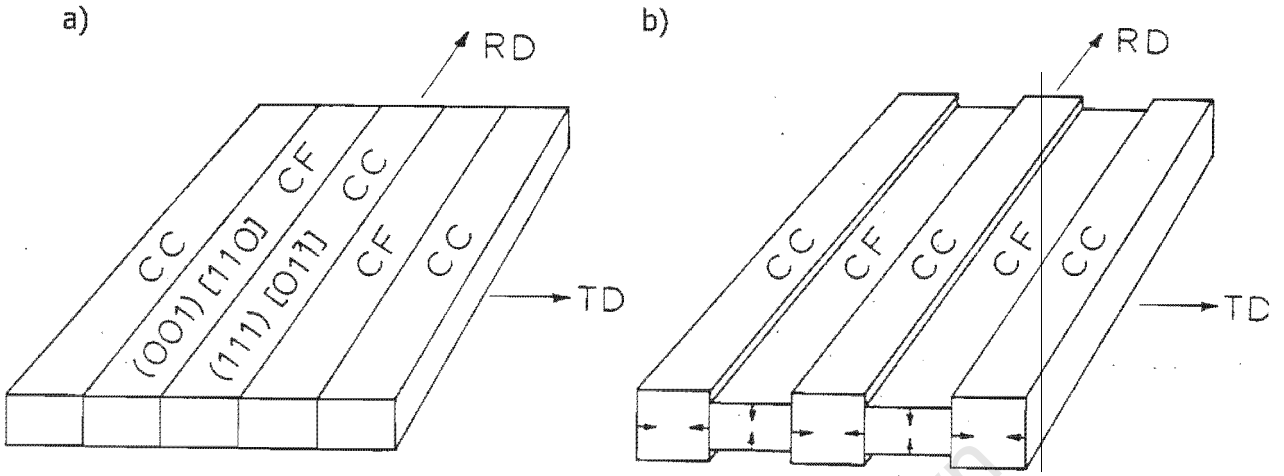

Figure 7. Schematic diagram showing Chao's mechanism explained by plastic anisotropy of alternating elongated texture components, a) before and b) after elongation in the RD, showing ridging.

He also noted that from this mechanism, it would follow that a material with a well developed CF texture within a CC matrix would exhibit severe ridging. If the CE texture is developed in place of the CF texture ridging would not be as intense. These predictions were substantiated by attaining pole figures for a number of different BCC materials. The results concluded, although not quantitatively so, that the mechanism's predictions were verified in practice.

A strong criticism of Chao's theory was that while the mechanism gave a ridged profile, where the thickness varied between ridges, in practice it was found that the thickness did not vary. Instead the ridging resulted in a corrugated profile[11]. This mechanism was thus deemed unsatisfactory and an improvement on this theory was required.

2.3.2 Mechanism by Takechi *et al.*

Later in the same year that Chao's mechanism was published, Takechi[21] *et al.* published their paper, which was the second and arguably improved mechanism of ridging formation. Although they do not reference the model proposed by Chao, they refer to other authors who had suggested that ridging was due to either plastic anisotropy or differential yielding. Takechi *et al.* recognise that all previous models and suggestions cannot explain the corrugated profile of the ridges. This important characteristic of ridging is addressed in their model.

They considered that the major texture component in 17% chromium stainless steels is the fibre texture with <011> parallel to the RD (now known as the α-fibre[22,23]). Knowing the slip systems available to the BCC crystals they calculated the crystal's strain in different directions when stress is applied in the RD. These calculations were similar to the strain ratio calculations made by Chao[20], with similar results. A crystal with a α-fibre orientation, when strained in the RD, changes its shape and will thin out in the <100> direction normal to the RD. Below is a diagram of the change of shape in two crystals perpendicular to each other but still both within the α-fibre texture after being strained in the RD.

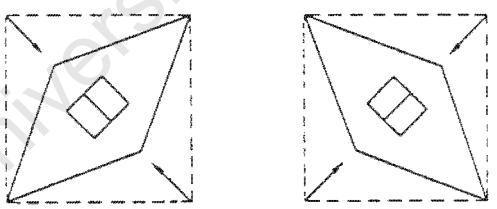

Figure 8. Cross section in the Rolling-Normal plane showing two crystals orientated with the α-fibre texture. The change of shape is seen after being strained in the RD[21].

The mechanism thus proposed by Takechi *et al.* is one where alternate bands extended in the RD are of differently orientated α-fibre texture. Heterogeneous strain would occur if the material is strained in the RD. This results in a corrugated profile schematically shown in the figure below.

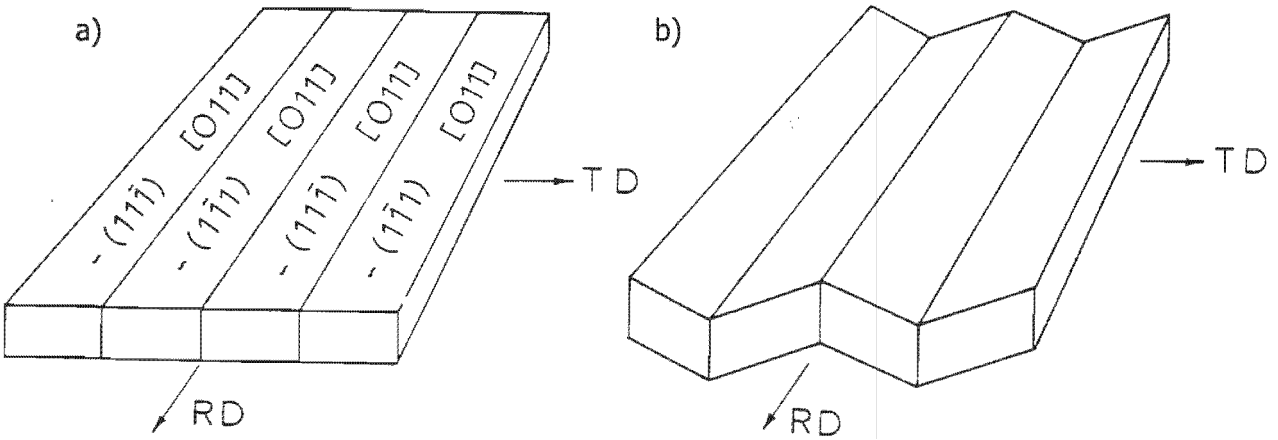

Figure 9. Mechanism of ridging by Takechi *et al.*[11].

To support the mechanism the authors needed to find a strong α-fibre texture in the final cold rolled and annealed sheet. Secondly, they had to prove that the sheet had arrangements of the α-fibre texture in differently orientated bands. They also needed to show that the spatial distribution of these bands corresponded to that of the ridges.

The bulk texture of the cold rolled material was measured where the α-fibre was the preferred orientation. An etch pitting method was used to reveal the orientation of material at the surface where ridges would form. The orientation is revealed by the direction in which the rhombic shaped pit develops, where the sides are in the <110> and <100> directions of the crystal. Good correlation between alternating bands of α-fibre oriented material and the ridges was reported.

Wright, however, criticises the Takechi mechanism since the etch pits were measured on cold rolled material which may have significantly changed after final annealing[11]. The pole figure after final annealing does not show dominance of either of the two textures of $(1\bar{1}1)[011]$ and $(11\bar{1})[011]$ that the mechanism fundamentally requires[11]. These criticisms lead R. Wright lead to propose another mechanism .

2.3.3 Mechanism by R. N. Wright

In 1972, Wright's model was published to improve on the existing models of ridging due to heterogeneous texture distribution. Wright argued that the explanation by Chao[20] did not correlate with the ridging morphology, and the mechanism by Takechi

et al.[21] was not adequately supported by texture measurements in the material's annealed state.

Wright begins by stating that although there are many textures found in AISI 430 steels, nearly all of them fall into two fibre textures. The first is where [100] is parallel to RD, this is the α-fibre. The second fibre texture has [122] parallel to the RD. The strain tensors for both of these textures were calculated. The results confirmed the strains predicted by Chao[20] when the material is elongated in the RD. Chao's CF, CC and CE all fall within the α-fibre texture.

Wright's theory is differentiated from the previous two not in the type of strains that occur in the different texture components or in their spatial arrangements, but rather in the dynamics of the material as it elongates. Wright proposes a buckling mechanism to explain the corrugated ridging profile. This buckling develops as a result of a non-random texture distribution and their associated non-random straining behaviour. An example of a (001)[110] texture component, CF, in a matrix of $(111)[11\bar{2}]$, CC, is given in the diagram below to present the mechanism.

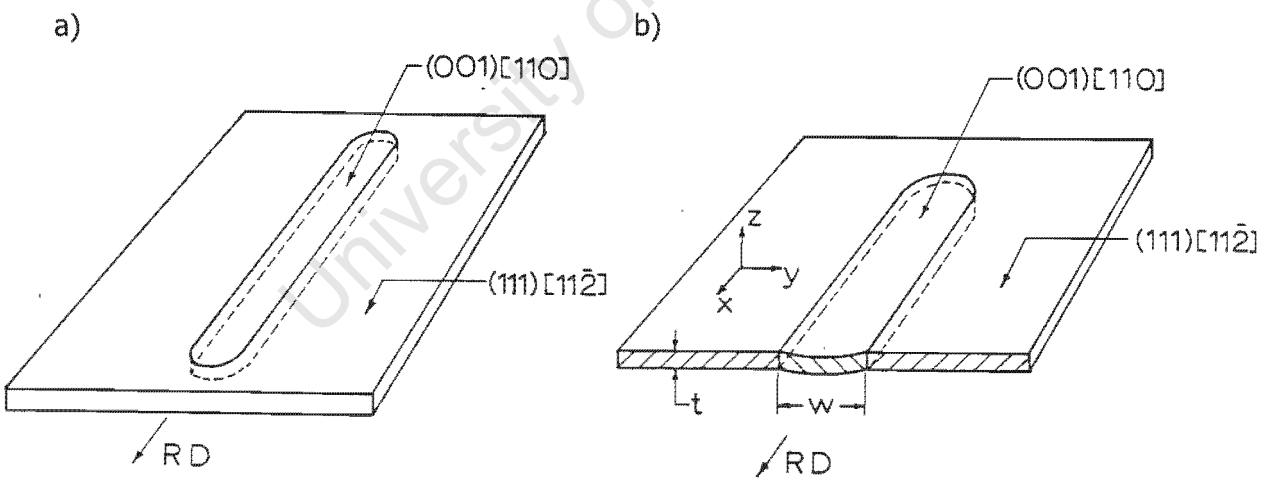

Figure 10. The mechanism of Wright's plastic buckling mechanism, with material (a) before and (b) after elongation[11].

In this example the (001)[110] texture would decrease its dimension predominantly in the ND as it is elongated, while the $(111)[11\bar{2}]$ narrows in the TD. Therefore since the (001)[110] texture does not experience a change of thickness in the TD, as its surrounding matrix does, it begins to buckle and protrude above the sheet.

The requirements for this model are thus longitudinal through-the-thickness bands of material elongated in the RD. These bands should mainly consist of grains with a preferred orientation that contracts in the ND under strain in the RD. These bands should also be surrounded by a matrix which contracts in the TD under the same strain. Wright refers to textural and ridging data taken from another report, which seems to suggest that the material that ridged the most severely had the above required textural components present.

After these three pioneer mechanisms were proposed, all published within six years of each other, other mechanisms were proposed that were essentially improvements on the pioneer models. With time, the development of better technology enabled reliable interpretation of the microstructure; for example electron back-scattered pattern indexing ultimately replaced the etch pitting method used to reveal the topological arrangement of textures. Technology thus enabled researchers to better measure the textures and their distribution on a microstructure scale, which aided their understanding to produce more accurate models. These new mechanisms differed mainly in types and topological arrangement of textures that gave rise to the differential strains[18,23,17,14]. The most recent of these mechanisms (1998), was proposed by Wittridge and Knutsen and will be discussed below[14,24].

2.3.4 Wittridge and Knutsen Mechanism.

This mechanism is the result of a detailed microstructure, microtexture and plasticity analysis. In an investigation of ridging behaviour after processing with different hot rolling temperatures, Wittridge and Knutsen were able to correlate the different ridging topography of the samples with the observations in the microstructure[14,24]. They noticed that there were significant variations in grain size, and that these variations were clustered in bands extending into the rolling direction. Clusters of grains having preferred orientation were also observed in some samples. Both of these variations, however, were on a scale far smaller than the scale of the ridging undulations. A mechanism was thus proposed that requires a material to have a heterogeneous distribution of plastic properties, where these heterogeneities are elongated in the rolling direction. If such a distribution results in an asymmetric distribution of plastic flow properties, then upon deformation transverse strains will

result leading to localised bending events and ultimately the ridged profile. This mechanism is schematically represented below in Figure 11.

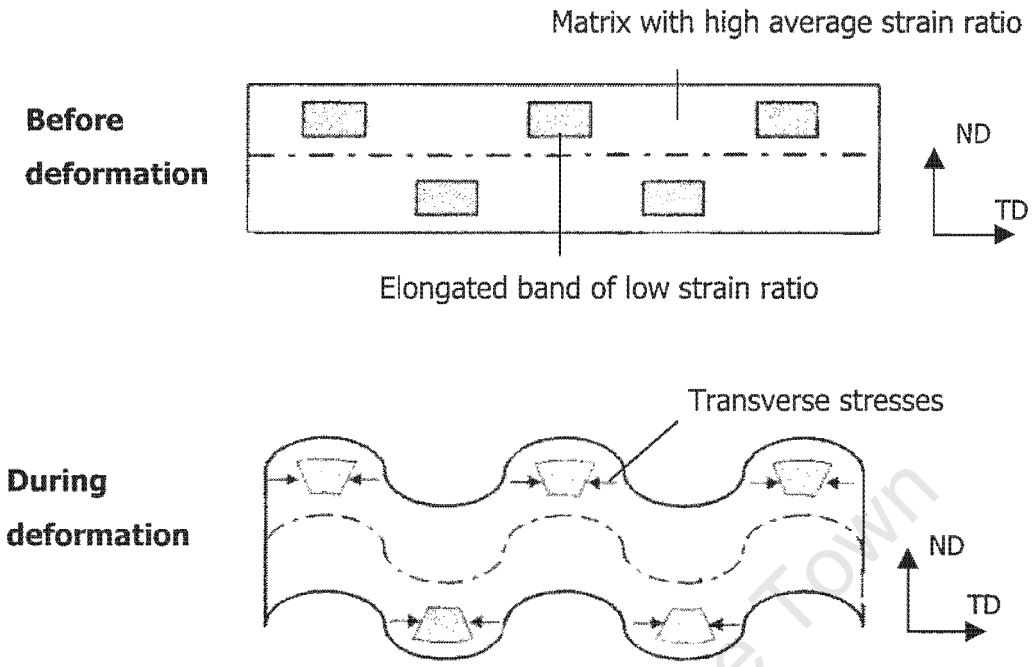

Figure 11. Ridging mechanism by Wittridge and Knutsen, indicating the transverse strains resulting from an asymmetric distribution of plastic properties.

This mechanism distinguishes itself from others in that it does not specify a particular texture responsible for the ridging. It also acknowledges the macro effect of several clusters of preferred orientations that can produce asymmetrical plastic properties about the centre line, rather than a single elongated cluster of textured grains. It also suggests that the bands of various grain sizes may at least be partly responsible for the distribution in plastic yield behaviour. This mechanism also has the advantage of being supported by finite element models, which predicted the same corrugated profile after prescribing such a distribution of plastic properties.

2.4 Methods for Reducing Ridging Severity

In order to reduce or eliminate ridging in the material, the development of heterogeneous bands in the material that causes ridging must be prevented or at least weakened. Since it is the rolling procedure that produces these heterogeneous bands there could be many solutions, alternative to the standard rolling, which would

eliminate ridging yet still flatten the material into sheets. For example, the sheet could be rolled in many different directions to prevent uniaxial elongation of bands. This, however, would produce a sheet of an awkward disk shape[25]. Such solutions are not feasible for a plant that is required to produce sheet products in the cheapest and quickest manner, while still maintaining the highest possible quality and consistency. A summary of the successful attempts to reduce the ridging severity that could be employed in practice follows.

2.4.1 Production Methods

These methods require specific equipment in the mill but are effective in reducing the ridging phenomenon. The first method employs a strip casting mill as opposed to the more conventional continuous casting for the production of stainless steel sheets[26,27]. This method was developed in the early 1990's[26] as a more economically efficient way of steel production[28]. The continuous casting method produces a slab of approximately 200mm thick, a significant portion of which solidifies dendritically. This slab undergoes a homogenisation heat treatment, is hot rolled, often receives a hot band anneal before being cold rolled and finally annealed for a recrystallization treatment. The strip cast method, however, casts a steel band of equivalent dimensions to the hot rolled material in conventional practice, thus eliminating two stages of conventional processing. This is achieved by feeding the liquid metal through two casting rollers where it is solidified and slightly deformed into a uniformly thick band. The procedure is diagrammatically represented in Figure 12 below.

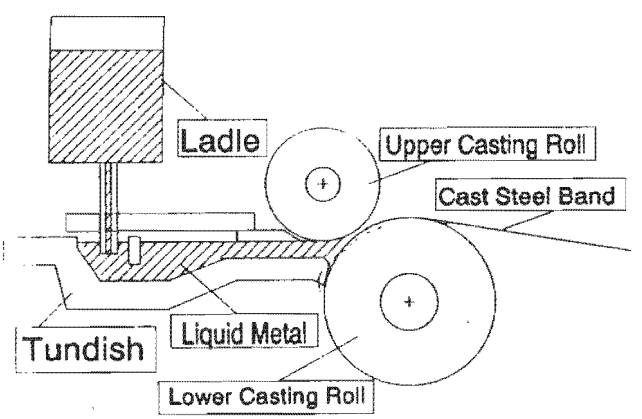

Figure 12. Diagram the strip casting process[27].

During hot rolling, friction of the rolls against the material causes a strong shear texture to develop at the surface of the conventional sheets. This texture gradient is absent in strip cast materials[27]. Without the heavy deformation of hot rolling, the strip cast material, in comparison, has a very weak texture without an elongated structure[27]. The cast structure is also better controlled with the strip casting technique. Ueda[28] reported that with a reduction in casting temperature and the addition of small amounts of alloying additions such as Ti and Nb, a fine equiaxed structure was achieved. This method reduces the ridging severity by producing an equiaxed fine homogeneous structure ready to enter the cold rolling procedure[27,28]. Material produced by the continuous casting method at the equivalent stage of processing would have an inhomogeneous elongated structure with preferred orientation after hot rolling. The strip casting technique does not detrimentally compromise the mechanical properties of the material, they are in fact very similar for both methods[27].

Another method reducing the strength of the texture gradient in the thickness direction, is the use of a planetary mill[29]. Instead of a single roll applying the force required to deform the material in a rolling pass, the planetary mill has several smaller rolls attached to the perimeter of a larger roll. These smaller rolls are able to roll independently and act much like a roller bearing between the larger roll and the material. Consequently there is less friction between the rolls and the material during rolling and thus the shear textures that develop in conventional tandem or steckel mills are not developed[29]. Another distinction between the planetary mill and other methods is that in a single pass the material can be deformed by greater than 90%, far higher than the reduction imposed by passes in other rolling methods. The use of a planetary mill, which results in a uniform texture distribution throughout the material, is thus implied by Omori[29] to improve the ridging phenomenon. This, however, was not experimentally verified.

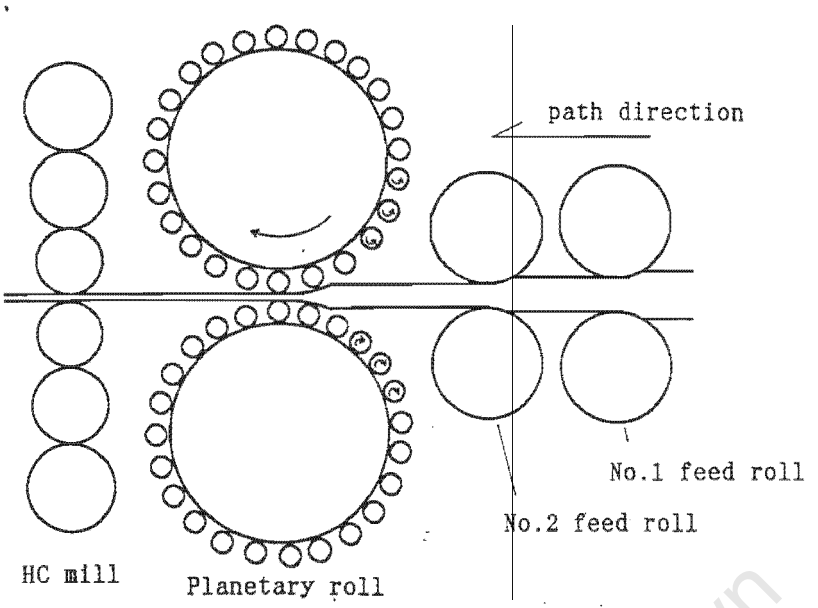

Figure 9. Schematic illustrating hot rolling with the use of a planetary mill[29].

Before a technique is discussed that involves reducing the columnar grain fraction of the cast slab, the alleged reason for the columnar fraction's detrimental effect is discussed. The columnar region grows dentritically with a preferred orientation of {001}<uvw> which, during rolling, rotates to form a strong {001}<110> textural component within the α-fibre[30]. It is this orientation that Harase[18] observed to occur as large colonies in the final microstructure. Harase thus attributed ridging to the asymmetrical distribution of colonies of {001}<110> orientation, the grains of which have a similar r-value, in a randomised matrix[18]. Columnar grains in the cast slab thus set up an initial microstructure that has a greater tendency to form preferred orientation colonies in the final microstructure than the equiaxed portion. Furthermore, Tsuji *et al.*[31] have found that the recrystallization kinetics of a columnar structure after deformation is strongly dependent upon its initial orientation. They found, for example, that a (001)[110] orientated grain would have low number of deformation bands after cold rolling and after annealing would have a low driving force for recrystallization[31]. Others, with different initial orientations, may develop a high driving force for recrystallization[31]. Thus, material with an initial columnar structure has been observed to recrystallize into a highly anisotropic grain size due to its strong recrystallization dependence on initial grain orientation.

The equiaxed fraction of a continuous cast slab has been observed to increase to greater than 50% of the thickness when casting with the use of electromagnetic stirring. Electromagnetic stirring has been successfully incorporated into commercial continuous casting plants specifically to combat the ridging problem in 430 stainless steel[32]. Two linear induction motors on either side of the slab's width make use of the material's magnetic properties to stir the melt with alternating magnetic poles rather than letting it stagnantly solidify[32]. The refinement is assumed to be due to the increased number of crystal nuclei created which form sites for solidification to occur. These nuclei are created from the tips of columnar crystals that are sheared off by the current of liquid metal and become suspended in the melt[32]. With careful temperature control to retain the nuclei within the melt, and sufficient control of the alternating flow of material, a high equiaxed fraction (>50%) was achieved. This has reportedly reduced ridging height in the final product[32].

2.4.2 Thermomechanical Methods

These methods involve adjusting the parameters within the thermomechanical process (TMP) in an attempt to destroy the inhomogeneous bands and obtain a homogeneous final microstructure. Almost all of the methods discussed below engineer the TMP and consequently the materials microstructure in order to encourage recrystallization. Recrystallization is the process where a deformed grain is replaced by several new strain free grains that have a relative misorientation of typically above 15°. This is an effective way to refine grain size as well as randomise the textures in the structure. AISI 430 Stainless steel, being a BCC structure, prefers to relax its strain energy by recovery rather than recrystallization, as discussed in section 2.1.5, and this is the difficulty in removing the heterogeneous bands from the microstructure.

Many researchers have found that the presence of the martensite phase in the structure during cold rolling has a dramatic effect of reducing ridging height[12,33,34,35,36]. Sheppard and Koike attribute the improved ridging properties to the martensite phase that causes refinement of the microstructure after final annealing[12,35]. During cold rolling the substantially harder martensite phase resists deformation and partitions the strain energy to the surrounding ferrite matrix[35,36].

Thus during annealing, the highly deformed ferrite matrix has a high driving force to form a fine recrystallized structure. At the same time the martensite will transform to ferrite by nucleation and growth, resulting in ferrite orientations unrelated to the deformation textures[36].

The method to introduce martensite into the structure involves a heat treatment that enters the dual phase $\alpha + \gamma$ loop, causing austenite to form which then transforms to martensite on cooling. Martensite is normally found in the as hot-rolled structure if rolling had occurred within the dual phase region. An anneal after hot rolling can have the benefit of softening the material for cold rolling and improving the r-value of the final sheet, but this transforms the martensite to ferrite plus carbides[34]. Miyaji found that a post hot rolling heat treatment within the single phase α region followed by a short increase in temperature into the dual phase region and then quenching, is beneficial[33]. This procedure enables the elongated martensite produced during hot rolling to transform back into ferrite and carbides, which distribute themselves evenly by diffusion. The carbides, together with the grain boundaries, then form the nuclei for austenite to grow on subsequent heating in the dual phase region. After cooling the structure will have a homogeneous distribution of martensite. From Miyaji's findings, the improved distribution of martensite before cold rolling which is not inherited from the banded hot rolled structure is more effective at randomising the texture[33]. Abbruzzese showed that a series of infracritical anneals before and during cold rolling improves the ridging properties[36]. The purpose of these anneals is to continue randomising the developed textures with the creation and transformation of the martensite phase.

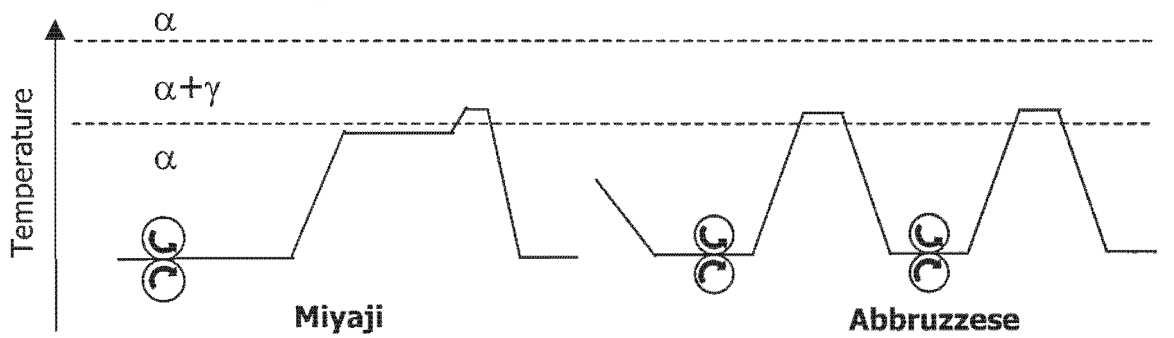

Figure 13. Schematic representations of the strategic annealing treatments of Miyaji, after hot rolling, and Abbruzzese, during cold rolling. Both utilise the formation of austenite in the dual phase temperature range for the reduction of ridging severity.

Hamasaki et al. used the $\alpha \rightarrow \gamma$ transformation in a different way[37]. They used the transformation to grow new, relatively random orientated grains to randomise the texture colonies after final annealing. The final recrystallization anneal involved heating up the material into the dual phase region for a short time, quenching it to a temperature slightly below the γ-loop and slowly cooling it down to room temperature (see Figure 14 below). This has the effect of destroying the banded structure by allowing recrystallization to take place in a dual phase region so that a significant fraction of the new strain free grains are austenitic. The austenitic grains transform back to ferrite after cooling to the lower temperature, and the slow cooling ensures that no martensite is formed, thus retaining the formability. At the temperature within the γ-loop, grain growth is rampant so care should be taken to select a suitable time at this temperature. Final recrystallization is thus performed with the portion of material that transformed having no inherited orientation from the rolling procedures, which fragments the texture colonies.

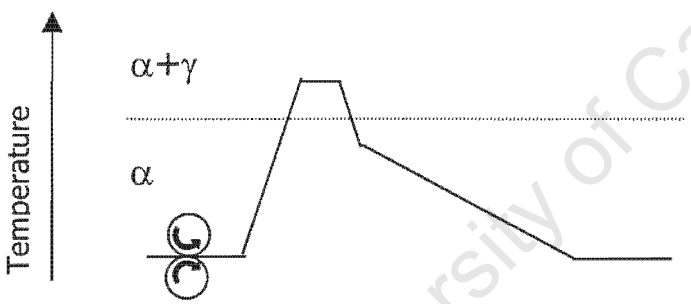

Figure 14. Schematic of Hamasaki et al. use of final recrystallization anneal within the dual phase temperature range to randomise texture colonies.

Hölscher has shown that precipitates can act in the same way as martensite to cause strain partitioning during cold rolling. The precipitates can similarly cause high deformation for recrystallization, even producing different textures to samples with few precipitates[38]. With varying hotband annealing times Hölscher has shown that the size of the precipitates can be controlled with time at high temperatures since their size is dependent on their diffusion through the material. A set of orientation distribution functions taken of the cold rolled samples show the weakening of texture as the size of the precipitates in the samples become larger,

Figure 15. Although no tests on ridging behaviour were done in the same investigation, it is reasonable to speculate that increasing the time during a hotband anneal to increase the precipitate size, would improve ridging properties. They did find, however, that with increasing the size of precipitates, the r-value decreased implying worse formability.

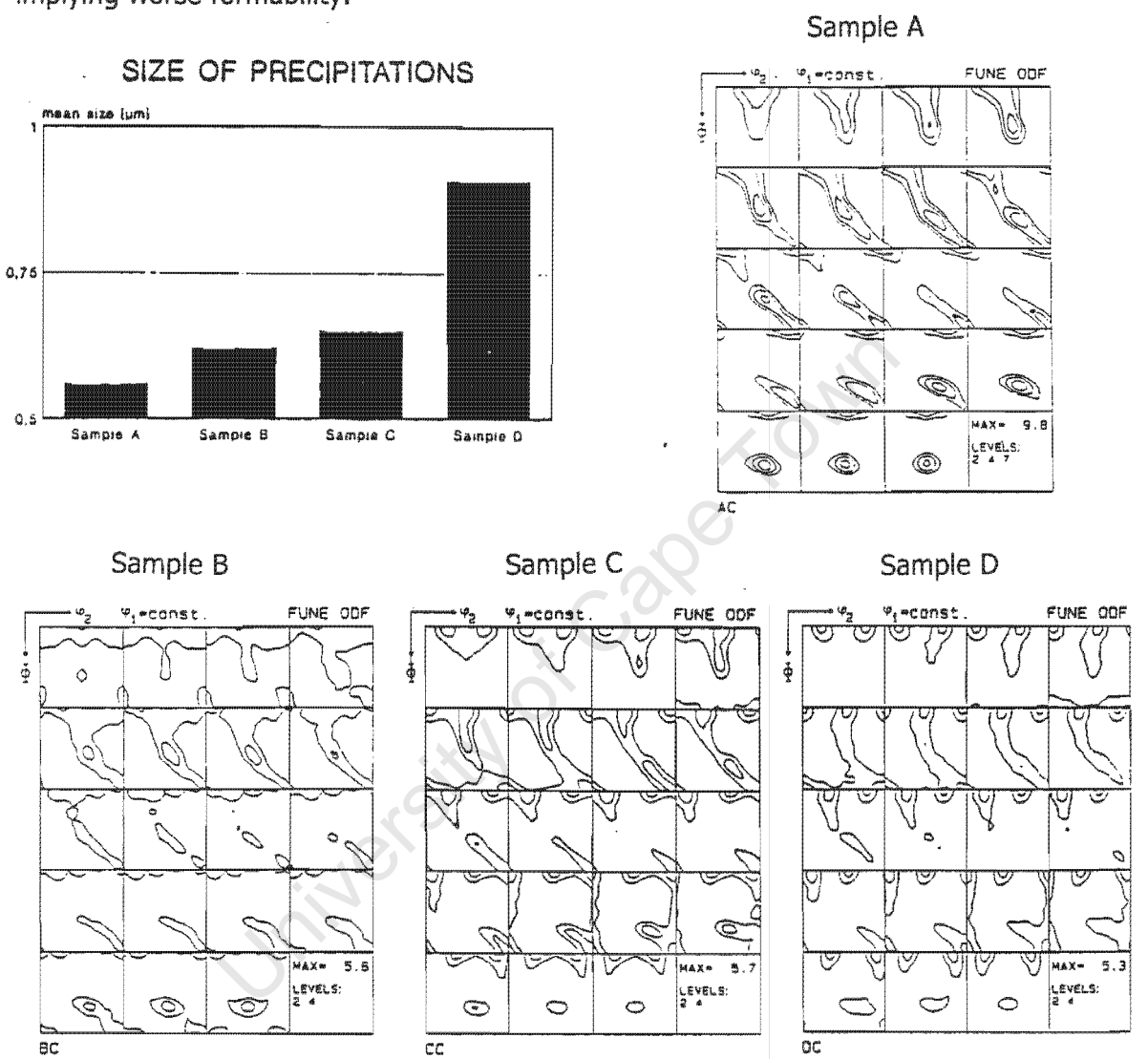

Figure 15. Hölscher's correlation between the size of the precipitates and their randomisation effect on textures seen by each sample's ODF[38].

Studies have found that static recrystallization can be encouraged during hot rolling with a suitable combination of hot rolling temperature, deformation energy and time between passes through the mill[18,34,39]. This has the beneficial effects of producing a structure with a finer grain size and more random texture than one which has not undergone recrystallization during hot rolling. Harase's[18,34] samples showed both these effects after extending the interpass time from 10 to 30 seconds and ultimately

the specimens with greater interpass times showed marked improvement in ridging properties[18]. Since ferritic stainless steels have a greater tendency for recovery due to their high stacking fault energies, the conditions of Harase's observed recrystallization must be noted. Their material was soaked at 1200°C before hot rolling with the last passes receiving heavy reductions of 30-40% and was finished between 1000°C and 1100°C[34]. Rolling at this temperature would produce martensite in the hot rolled structure, but to remove the effect of martensite presence during cold rolling, a low temperature anneal was included to eliminate the martensite[34]. The results still showed good resistance to ridging behaviour after final anneal due to static recrystallization[34].

On the other side of the hot rolling spectrum, some studies show that a low hot rolling temperature with adequate rolling reduction increases the stored deformation and leads to a better refinement of the structure during annealing[9,12,39,14]. When using this method of creating greater stored energy in the structure, an anneal after hot rolling is included to recrystallize the microstructure before entering the cold rolling stage. The material after final annealing has a randomised structure showing low ridging severity after being recrystallized following hot rolling and cold rolling[39].

2.4.3 Compositional Methods

An effective method that has received strong support from a number of different researchers is the addition of minor alloy elements (<1%) of niobium and titanium to the steel[39,40,41,42]. Conventionally these elements are added for their ability to stabilise the steel. They have a strong affinity for carbon and will form precipitates preferentially over chromium carbide formation, lowering the potential for sensitization to occur during processing or welding. However, its rather their effects on recrystallization kinetics that benefit the steel with severe ridging.

With the precipitation of TiC and NbC, the steel's recrystallization kinetics become more sluggish due to the pinning forces they impart on a grain boundary[40,42]. The two graphs below, Figure 16, illustrate the increased driving force required (either temperature or strain energy) to recrystallize a 430 steel of 0.6 wt% Nb compared to a conventional 430 steel[39]. The suppression of recrystallization results eventually in

an accelerated one, after the driving force has been overcome, with many more nucleations within the deformed structure, leading to a finer and more homogeneous microstructure[39,42].

a) b)

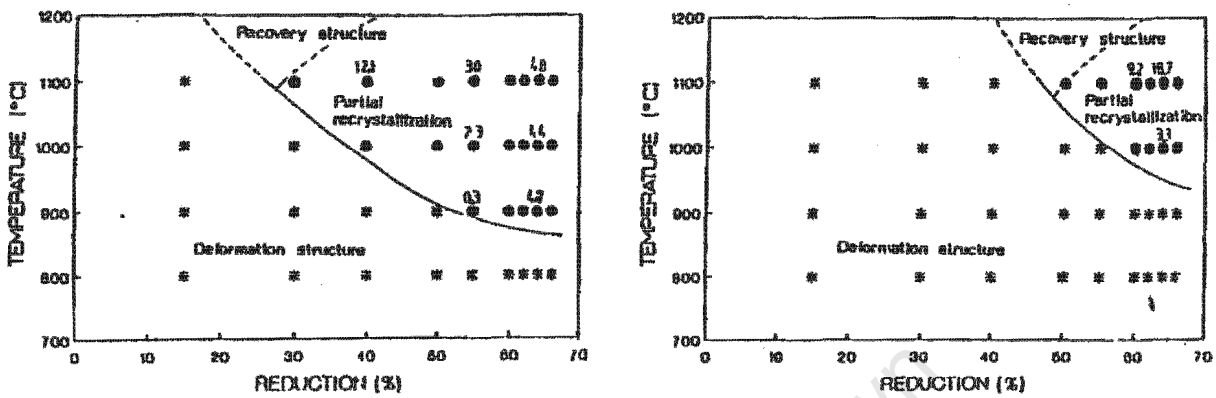

Figure 16. Graphs of the resulting microstructure after annealing as a function of hot roll reduction. They depict the suppresion of recrystallization due to the addition of niobium, a) conventional AISI 430 Steel, b) 0.6 wt% Nb added.

Fortunately the quantity of Nb and Ti required to be effective in reducing ridging severity is small (below 1 wt%). Fujimura[42] found the following equation for dependence of the 50% recrystallization time on the quantity of alloying elements present, the last term being a temperature dependent constant.:

Equation 2:

$$Log(t_{0.5}) = 31[mass\%C] + 4.3[mass\%Ti] + 7.9[mass\%Nb] + d(temp.const.),$$

This shows that Nb is more effective at suppressing recrystallization than titanium. Although niobium is expensive, roughly three times the price of chromium, it only requires around 0.7wt% to be beneficial and thus is an economically viable solution[41].

2.5 Plasticity analysis

2.5.1 Effect of Grain Size

A grain boundary is a hindrance to the propagation of a moving dislocation. The dislocation is trapped at this boundary since the incoherence between two neighbouring crystal lattices does not allow a passage to further propagate. Thus, by refining a metals grain size, which increases the density of grain boundaries, the metal's strength can be increased. The Hall-Petch equation has been widely used to relate grain size to strength in a material and is seen in Equation 3[7].

Equation 3 $$\sigma_y = \sigma_o + k_y.d^{-1/2}$$

Here σ_y represents the yield strength, σ_o is the strength of the material with infinite grain size, k_y is a constant of the material representing grain boundary friction, and d the grain size of the material. With a logarithmic exponent to the grain size the strengthening is more sensitive as the grain size decreases.

2.5.2 Textures

A single crystal will have anisotropic properties due to its symmetry[43]. The higher the symmetry of a crystal the greater will be the anisotropy of its properties. In a similar manner, a polycrystalline material can exhibit anisotropy of properties if there is a preferred orientation within the microstructure. These preferred orientations in a metal are known as textures.

A texture can be produced in a material by several methods. Preferred orientations for growth of crystals during solidification or phase transformations, or by changing their orientations by rotation during deformation can all produce textures[43]. The latter is of particular significance in materials processing where textures can have disadvantages such as earing in aluminium sheets, or advantages such as the improved strain ratio produced by rolling textures for deep drawn products. The

crystal rotates by a process of slip during deformation and will tend to rotate towards a certain orientation. Since the slip systems in FCC materials are different to BCC, their respective rolling textures differ.

The rolling textures in BCC steels consist mainly of fibre textures, where a fibre texture is a range of orientations that are show rotational symmetry about the fibre axis. The direction of the fibre axis for rolling textures will align either in the rolling direction in which direction the material is elongated, or in the normal direction in which the sheet is compressed. These are the common rolling textures found in BCC steels[44,38]:

α-fibre, <110> // RD, {001}<110> to {111}<110>
γ-fibre, <111> // ND, {111}<110> to {111}<112>
η-fibre, <001> // RD, {110}<001> to {110}<001>

The η-fibre texture is a shear texture and forms at the surface of the material due to the friction experienced between the material and the mill[44]. The other two textures are more prominent and found within the centre of the material. After a recrystallization treatment, the relative strengths will differ due to the increased ability of some orientations to grow into others. The higher the misorientation between the parent and new grain, the greater the mobility of the migrating recrystallized grain boundary[8]. By experimentation, the strong {112}<110> component of the α-fibre has been found to weaken after recrystallization with the relative strengthening of the {111}<112> component within the γ-fibre[44].

Some authors claim that severe ridging is associated with a strongly developed α-fibre[20,45], some specifically identify the {100}<110> orientation within the α-fibre as the cause of ridging[18]. A strong η-fibre has also been identified as being associated with severe ridging, since it results in a large through-thickness texture gradient[29,36,46]. While the strengthening of the γ-fibre after recrystallization reportedly results in a better surface finish after deformation[46,45,36].

2.5.3 Taylor Analysis

A texture analysis of the material allows one to assume that together with a strong texture, anisotropic properties will result. A Taylor analysis of the material, however, more directly examines the effect of texturing on the yield properties in a prescribed straining direction. Such an analysis is possible using the electron back-scattered diffraction technique which gains orientation information from the surface of the material. A Taylor factor, M, is an orientation dependent number that describes the ease at which a crystal will deform given a prescribed deformation direction. It is this factor that relates the orientation independent property of critical shear stress, τ, to the orientation dependent yield stress of the material in Equation 4 below[47].

Equation 4. $$\sigma_y = M\tau$$

The equation is derived using the assumption that all grains undergo the same shape change, the same as that of the entire crystal, during deformation. Thus if the crystal is to deform in the x direction:

$$d\varepsilon_y = d\varepsilon_x = d\varepsilon_z$$

Where $d\varepsilon_x$ is the increment of strain in the x direction. The work expended in deforming a volume of material is:

$$dw = \sum_i \tau d\gamma_i = \tau \sum \left| d\gamma_i \right|$$

Where τ is the critical shear stress, and $d\gamma_i$ is the incremental slip on each slip system. This expression is simply:

$$dw = \tau d\gamma$$

The work done by uniaxial deformation is also simply:

$$dw = \sigma_x d\varepsilon_x$$

Therefore these two expressions can be related together by the Taylor factor, M.

Equation 5 $$\frac{\sigma_x}{\tau} = \frac{d\gamma}{d\varepsilon_x} = M$$

Thus a random polycrystal will have a yield stress that can be calculated with the product of the average Taylor factor, $\overline{M}$, and its critical resolved shear stress, τ.

3 EXPERIMENTAL METHODS

This chapter records the material, techniques and equipment used in this investigation. It contains all the information for the techniques to be repeated and the results verified.

3.1 Material

All the samples used for this investigation came from the same AISI 430 slab produced by the continuous casting method. The slab used in this investigation had a composition as seen in Table 1.

Element	C	P	Mn	Si	V	Cu	Co	Ni	Cr	N	Fe
wt%	0.04	0.02	0.65	0.55	0.11	0.08	0.04	0.17	16.51	0.03	Balance

Table 1. Chemical composition of material (only elements with fraction ☐ 0.01wt.% included).

From this slab 16 samples were cut out, each to represent a unique combination of two starting structures, four hot rolling finishing temperatures (HRFT) and two cooling methods after hot rolling. Each sample represented either the columnar starting structure, from the surface of the slab, or the equiaxed structure from within the centre of the slab. The HRFT's approximated 700°C, 800°C, 900°C and 1000°C and the method of cooling involved either slow cooling or a quench down to about 400°C followed by a slow cool. The notation used to describe each unique sample is shown in the table below.

	Columnar		**Equiaxed**	
HRFT (°C)	*Slow Cooled*	*Quenched*	*Slow Cooled*	*Quenched*
1000	C1000s	C1000q	E1000s	E1000q
900	C900s	C900q	E900s	E900q
800	C800s	C800q	E800s	E800q
700	C700s	C700q	E700s	E700q

Table 2. Sample notation.

A large section of the slab was cut out and macroetched to reveal the structure. The etchant was a mixture of nitric acid (HNO_3) and hydrochloric acid (HCl). This

enabled samples that were completely within either the columnar or equiaxed region to be selectively cut out. Figure 17 shows a macroetched view of a section of the slab showing the chill zone at the surface, the columnar region below that and the equiaxed region in the centre of the slab, the latter being the last to solidify.

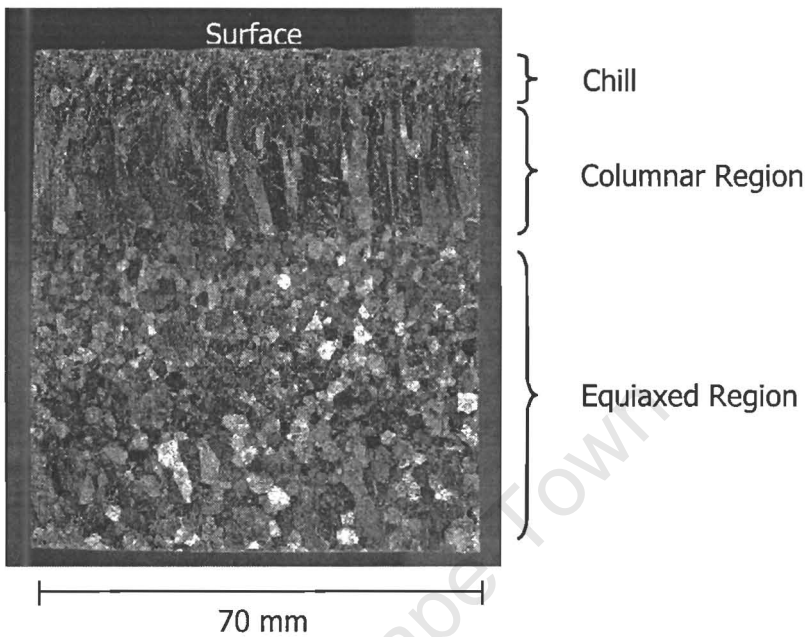

Figure 17. Macro-etched structure of cast slab showing different structure regions.

Eight samples were then cut from each of the two different structural regions. The following schematic outlines how the 16 samples were cut with respect to the original cast slab piece.

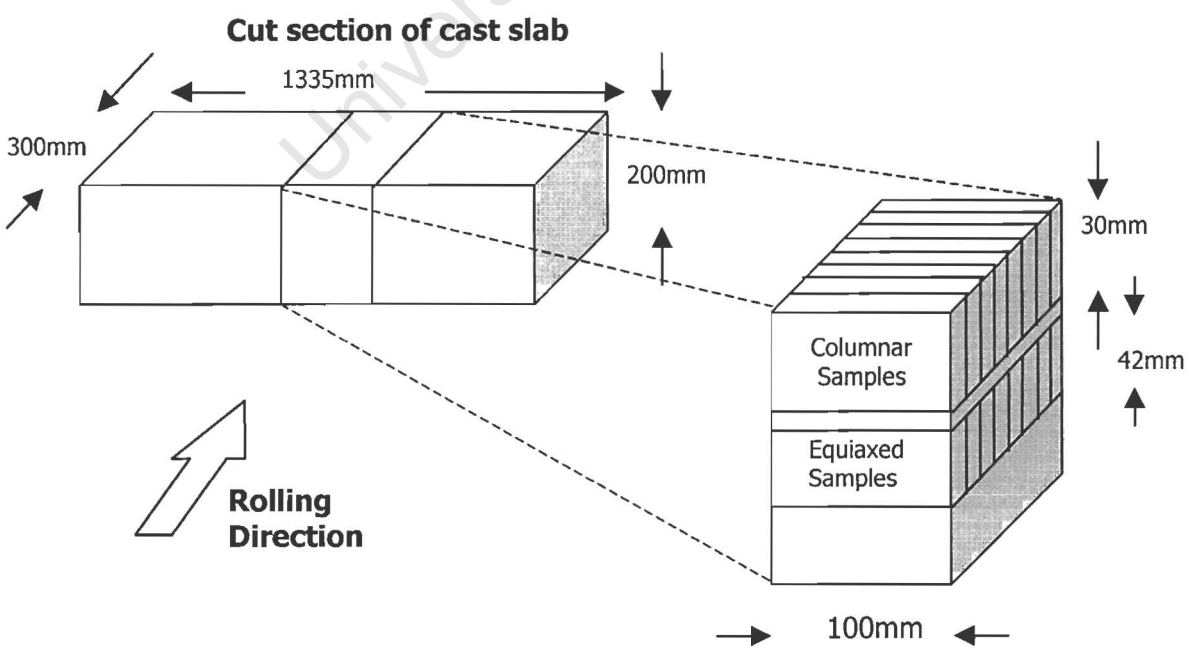

Figure 18. Shematic illustrating the orientation of samples w.r.t cast slab.

These samples were placed in a laboratory furnace as a homogenisation treatment. This began the simulation of the thermomechanical cycle where the two other variables were included.

3.2 Laboratory simulation of TMP

3.2.1 Conventional TMP

The process of reducing a cast slab from around 200 mm thick to a sheet of only a few millimetres in thickness is called the thermomechanical process (TMP), due to the various heating and rolling processes involved. A conventional method used for a continuous cast slab would start with a homogenisation treatment at high temperature of 1100°C for 4 hrs. During solidification, the alloying elements are partitioned unevenly in the material, thus the homogenisation treatment redistributes the alloying elements evenly by diffusion. While the slab is still at high temperature, it is hot rolled with multiple passes, utilising the good formability the material has at high temperatures, with a target finishing temperature of 870°C. The hot roll stage reduces the thickness of the material about 90%. During the latter stages of hot rolling the material is coiled after each pass to maintain its heat through hot rolling. After hot rolling, the material is allowed to cool and is often batch annealed at 800°C for 6hrs to relax the stored energy from hot rolling and to reduce the hardness before cold rolling. After cooling to room temperature the material is descaled and pickled to remove the oxide layers formed from the hot rolling and annealing. The clean material is then cold rolled with a minimum reduction of 65%. A final recrystallization anneal removes the deformation energy in the material and restores ductility. It is then finally pickled once more to regain the clean appearance of the sheet. A schematic illustrating the process is shown below in Figure 19[48].

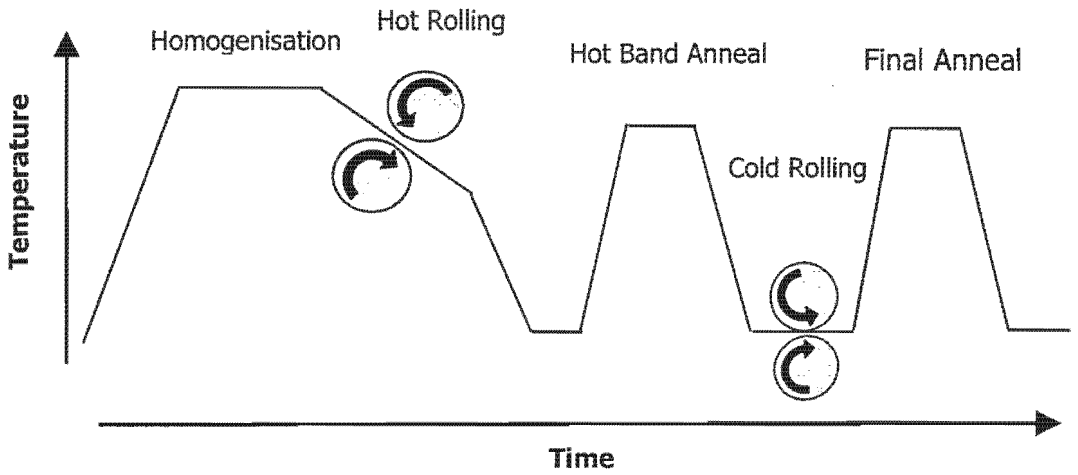

Figure 19. Schematic view of conventional TMP, from cast slab to final annealed sheet.

3.2.2 TMP used in this investigation

The 16 cut samples in this investigation were reheated at 1100°C for 3.5 hrs in a laboratory furnace to homogenise their composition. The hot rolling procedure was carried out in the same laboratory, where the samples were carried from the furnace to the rolling mill for a single pass and back to the furnace again. Several passes were completed before the hot rolling procedure was complete. After each pass through the mill, the samples were reheated in the furnace. The temperature of each sample was controlled in this way to keep the temperature during rolling above the prescribed finishing temperature. An optical pyrometer was used to measure the temperature of the sample immediately before and after each hot rolling pass. The pyrometer used was a Mindta-Land Cyclops S1 that was calibrated against an open furnace and has a reported error of 5% within its recommended temperature range of 700°C -1100°C. A table of recorded temperature readings of the samples as well as a table of their thickness measurements and calculated reductions can be viewed in Appendix 1a and 1b respectively.

Fibre-frax (silica glass wool) was used to slow cool the hot rolled material. The quenched samples were cooled for approximately 1 second in water, where it cooled about 100°C -200°C, before being covered with fibre-frax. The cooling rate within the fibre-frax was slower than air cooling, but faster than the rate in the plant since the hot band is coiled, retaining its heat better than within fibre-frax.

No annealing treatment was performed on the hot rolled samples before they entered the cold rolling mill. The hot rolled samples were pickled to remove the oxide scale that formed during homogenisation and rolling. A clean surface is desired before cold rolling in order to avoid rolling impurities into the steel. A pickling solution of nitric and hydrochloric acid was used to remove the scale. The surfaces were scrubbed to remove the remaining scale and were cold rolled on a separate laboratory mill thereafter. The cold rolled samples' final thickness measurements and their corresponding reductions can be viewed in Appendix 1.b.

The final recrystallization anneal was found experimentally by varying the temperature and time of the treatment and observing the resulting microstructures in the scanning electron microscope (SEM). A treatment that would result in a fully recrystallized microstructure without inducing grain growth was required to optimise the final properties. To this end a series of experimental anneals were done, each one successively increasing the probability for recrystallization. Samples from the 700°C and 800°C HRFT were observed in the SEM using electron channelling contrast (explained in section 3.4.2) to judge the effectiveness of the treatments. The experimental variables are shown in the table below with experiment 4 yielding the desired microstructure.

Experiment	Time (min)	Temperature (^{0}C)
1	5	800
2	5	830
3	5	850
4	10	850

Table 3. Variables in experiments leading to the ideal recrystallization annealing treatment.

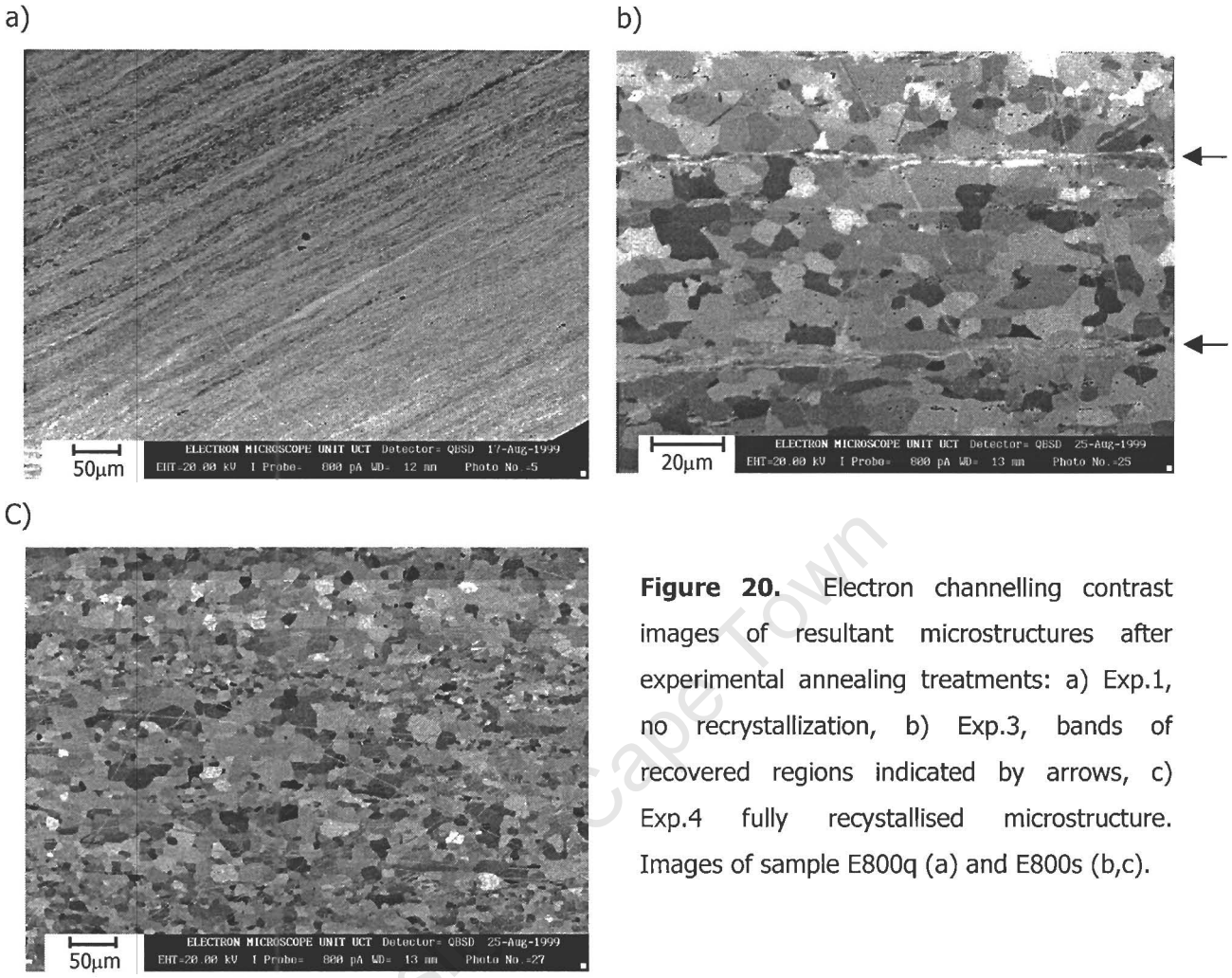

Figure 20. Electron channelling contrast images of resultant microstructures after experimental annealing treatments: a) Exp.1, no recrystallization, b) Exp.3, bands of recovered regions indicated by arrows, c) Exp.4 fully recystallised microstructure. Images of sample E800q (a) and E800s (b,c).

The schematic below, Figure 21, shows the TMP employed.

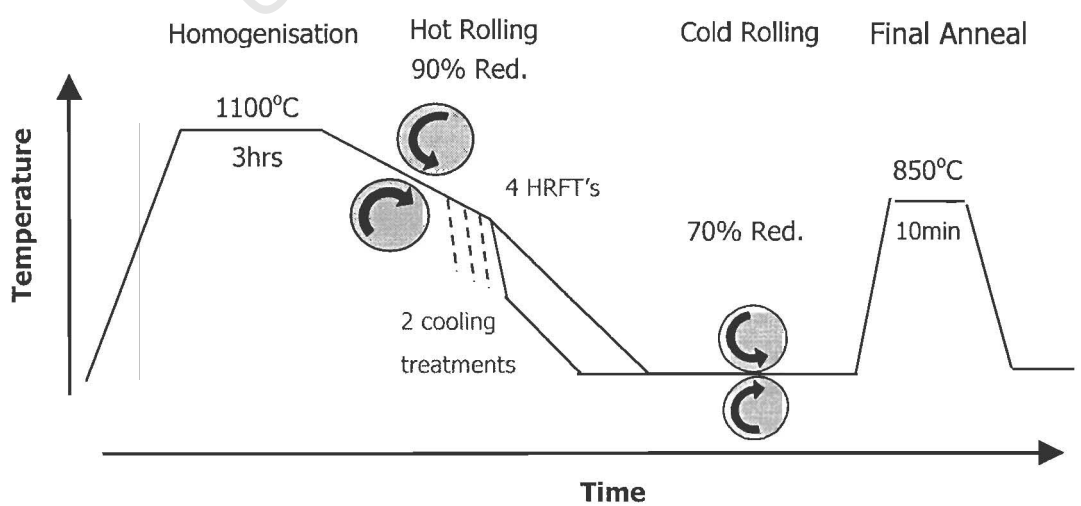

Figure 21. Schematic showing the experimental TMP used in this investigation.

Material in the as-cast condition, after hot rolling, and after cold rolling was cropped to have representative specimens for analysis. Tensile specimens were machined from the final recrystallized material in order to observe the ridging behaviour.

3.2.3 Hardness tests

The bulk hardness of the samples was tested after hot rolling, cold rolling and after final annealing. An Eseway hardness indenter, type SPVR.2, was used to measure the Vickers hardness with a 30 kg load. These measurements added to the interpretation of other analysis results and were useful for comparison between the different samples' microstructures.

A Matsuzawa MXT-cx7 digital microhardness indenter enabled the hardness of separate parts of the microstructure to be measured. It was useful to help identify the features in the hot rolled light micrographs. It employs the Vickers technique with very small loads, 100 gf used in this case, and the indent can be positioned manually while observing the microstructure through an objective lens.

3.2.4 Dilatometry

In order to measure the A_1 and Ms temperatures of the material a dilatometer that was purpose built was used. It is possible to heat a specimen in an airtight chamber to a temperature over 1000°C. The temperature is measured by a K-type thermocouple and the samples extension is recorded by a digital displacement transducer. The signals from each of these instruments are fed to a computer that contains a custom written program, Diladata, which records and converts the measurements to a useable format. The A_1 temperature is estimated at the midpoint temperature between the Ac_1, measured at the start temperature of the ferrite to austenite reaction on heating, and the Ar_1, the start temperature of the reaction on cooling at the same. The heating rate would have to be the same as the cooling rate for the estimation of the A_1 temperature. Therefore the specimen was set to heat at a rate of 2°C/minute, from room temperature to 1000°C, hold the maximum temperature for 10 minutes, and then to cool at the same rate to room temperature.

The Ms was measured by heating to the same temperature and then cooling with the maximum cooling rate allowed, typically around 30°C/minute. During these tests the chamber was pumped to a vacuum of 10^{-1}torr, which minimised the effect of oxidation expansion on the results.

3.3 Ridging Tests of Final Annealed Material

3.3.1 Tensile tests

To measure the severity of ridging that each sample with its unique combination of starting structure and TMP parameters would display, tensile specimens were machined and elongated to 20%. The ridging severity was compared between specimens by measuring the roughness with a stylus and mapping the topography of each specimen to a three dimensional digital surface.

Tensile specimens were machined to the dimensions of the insert on the right. These dimensions were not standard for ASTM tensile tests but were chosen to obtain a specimen with a good representation of the material's ridging behaviour. The thickness of the specimens was that of the final cold rolled thickness, seen in appendix 1.b. The tensile axis was machined to align with the rolling direction. This alignment is reported to result in the most severe ridging[13,14]. Both surfaces of each specimen were ground free of the oxide layer using emery paper. The ground surface was then polished using successively finer polish, finishing with 6μm diamond paste. This gave a mirror finish with a roughness (R_a) of around 0.15μm. Care was taken not to grind away excessive surface material that may prove to influence the ridging behaviour. Each specimen had around 0.07mm ground and polished away from each oxidised surface.

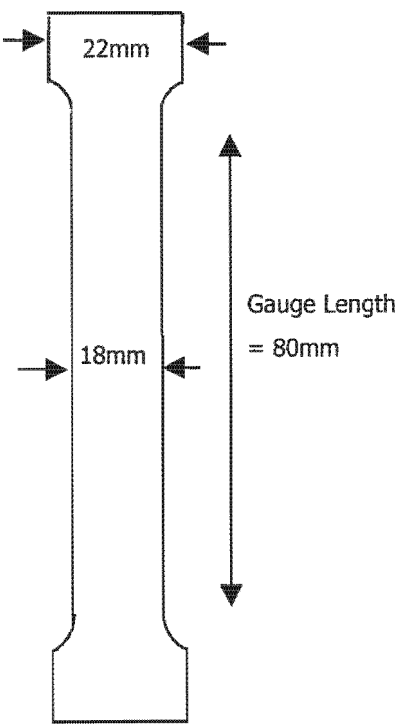

These specimens were elongated to 20% strain (if failure did not occur before) on a Zwick universal tensometer. This machine is a uniaxial tensometer equipped with a 200kN load cell. The strain rate used was 10^{-3} s^{-1} and extensometer arms were used to stop the test once 20% elongation had been reached.

3.3.2 Ridging measurements

The topography of the samples was mapped using a MAHR Perthometer 'Concept'. This machine is a very sensitive surface profiler that stores spatial co-ordinates of points along a line scan into a digital file. Spatial information from adjacent line scans can be stored in a single file as ASCII numbers and used to plot a three dimensional surface in suitable software. The 'Perthometer' uses a stylus on a stiff ceramic arm to traverse the surface of the specimen and records spatial variation in the vertical (z) direction as it moves in the x direction. After it traverses one line it moves in the y direction, by a prescribed amount, and traverses the next line. It has a vertical resolution of 0.01μm, and to obtain this accuracy the instrument can be floated on an air table to dampen the effect of background vibrations.

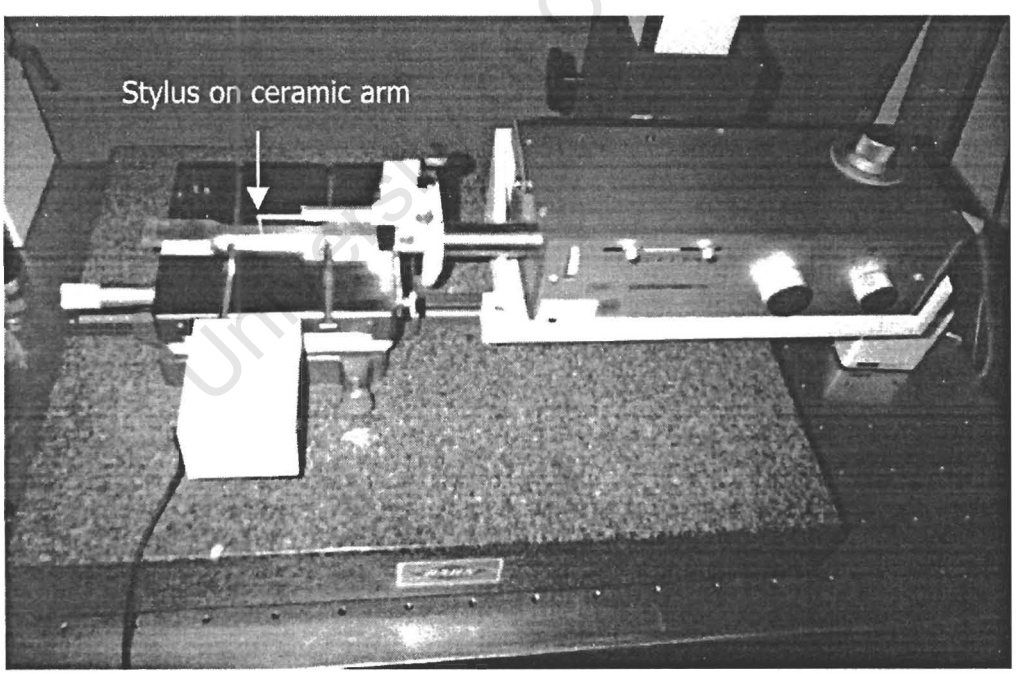

Figure 22. Photo of the Mahr perthometer with stylus over a specimen.

Two types of maps were measured on each specimen. Areas were mapped of 14mm (TD) by 17mm (RD) on the surface of the specimens to capture a large representation of the ridging effect. Smaller areas of 6mm (RD) by 4mm (TD) were

also measured with a higher resolution for each sample. In both cases the area that corresponds to the opposite surface was also mapped in each specimen to observe how the roughening on one surface correlated to that on the other. This is particularly important to investigate the corrugation effect.

The stored data was plotted in SURFER®, a Golden Software product, with the assistance of the Geomatics Department, University of Cape Town. One map of the two from each specimen had to be rotated in order to present them together showing how the ridging on one surface corresponds to that on the opposite surface. To rotate this data about the tensile axis, a program written in MATLAB, was used to manipulate the data before plotting it in SURFER®.

The roughness (R_a) of the specimens was measured using a Taylor and Hobson Surtronic 3P profilometer. At least six traces were measured and averaged for each surface. All the traces ran perpendicular to the rolling direction. The trace length was chosen to maximise the cut-off roughness wavelength, above which the undulation would not be taken into account. This maximum cut-off wavelength was 2.5mm, which was larger than the wavelength of the ridges (about 1-2mm) and ensured the ridging would be reflected in the roughness calculation.

3.4 Microscopy

Once the ridging results were obtained, several microscopy techniques were used to track the microstructural history of the samples. This was to aid understanding of how each starting structure and treatment in the TMP affected the microstructure of the samples. With this understanding, the explanation of how the unique microstructures differentiated, can be grasped. In addition, these techniques aimed to relate the observed microstructures to their corresponding ridging results.

All the specimens for microscopy were, for the first stages, prepared in the same way. Each was hot mounted in resin, and mechanically ground and polished by using a Struers Roto-Pol 22 automatic polisher. The last stage of polishing used a SiO_2 suspension polish.

3.4.1 Light Microscopy

The hot rolled structures were examined using light microscopy after having been electrolytically etched with 65% concentrated nitric acid (HNO_3). The etching revealed areas of martensite, grain boundaries and, in samples in which extended recovery had taken place, subgrain networks.

The electrolytic etching technique was found experimentally. It applied a low voltage of 1 Volt for 5 seconds across the sample and a stainless steel cathode resulting in a current density around $12mA.cm^{-2}$. The specimens were imaged under bright field mode using a Reichert MeF3A metallograph equipped with a Leica DC 100 to capture digital images.

3.4.2 Electron Channelling Contrast

A technique in the SEM called electron channelling contrast (ECC) was used to reveal the microstructure without relying on the interpretation of etching artefacts. This method employs a back-scatter detector to reveal the microstructure by differences in contrast. The brightness of a point in an ECC image is dependent on the ability of the corresponding point on the specimen to eject back-scattered electrons. An undeformed grain would appear with a single brightness on a greyscale spectrum. A neighbouring grain with a different orientation would be imaged with a different brightness. This technique has shown to be more useful than light microscopy techniques at revealing the structure, although it involves careful specimen preparation and a sensitive SEM set-up, which adds more time to obtain a result[9,49].

A good specimen for ECC needs a flat, clean surface, without uneven topography, and a surface free of distortion that can be subsequently introduced by mechanical polishing. Therefore, specimens were electropolished to remove the surface deformation layer created by mechanical polishing and entered the SEM unetched. A Leica Stereoscan 440 SEM was used with a solid state back-scatter detector (KE Developments Ltd.). The SEM was set-up to encourage maximum contrast between areas, the optimised settings used were: 20kV accelerating voltage; 50μm final aperture; 800pA probe current; 13mm working distance; 0.2 gamma setting and 0° tilt.

A fully recrystallized microstructure, where each grain has a single, undistorted orientation, would be revealed by contrast between grains. Each grain would have one particular shade in the greyscale. Within a deformed grain, there would be patterns of shades because as the orientation differs slightly across the strained grain, the number of electrons that escape from the surface differs. This recognisable pattern of deformation on an ECC image is termed a 'mottled' contrast and is the result of a high dislocation density with very little regular arrangement of dislocations. A recovered grain appears to have a segmented 'mottled' contrast that corresponds to the substructure of the grain. Depending on the degree of recovery in the specimen the subgrains can be distinguished from each other by contrast differences across their low misorientation boundary. A highly dislocated region, such as a highly deformed grain or martensite, appears as a single grainy shade without any distinguishable features. Figure 23. shows three micrographs showing the regions described above.

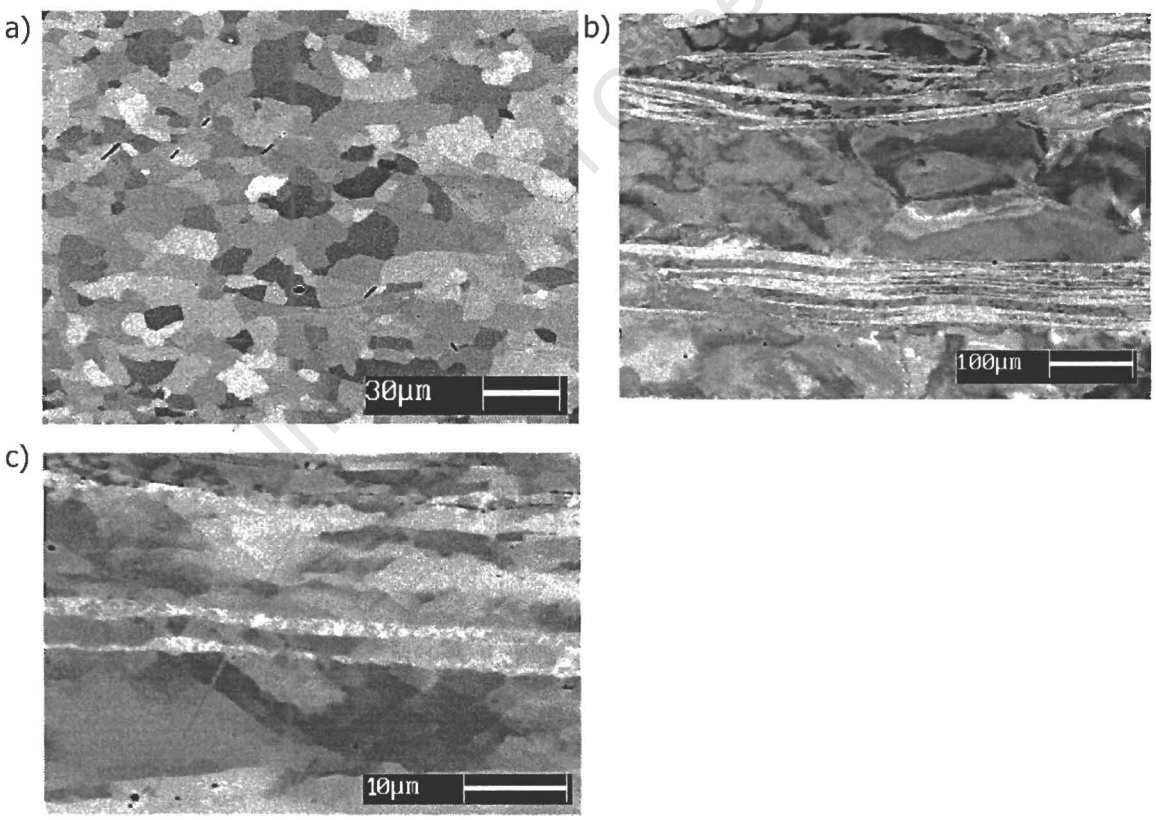

Figure 23. ECC images showing: a) a recrystallized microstructure with clear contrast in each grain; b) a deformed and partially recovered structure showing 'mottled' contrast and martensite stringers running horizontally; c) a recovered substructure with moderately developed subgrain structure and martensite stringers.

3.4.3 Electron Back-Scattered Diffraction

When electrons strike a highly titled specimen in the SEM, some are scattered off the material by Coulomb forces but others are diffracted off crystal planes by satisfying the Bragg diffraction condition. These diffracted electrons produce, what is called, a Kikuchi pattern that is superimposed on the background signal produced by the scattered electrons. The electron back-scattered diffraction (EBSD) technique uses this Kikuchi pattern to calculate the orientation of the crystal where the beam strikes the surface. With information on the SEM settings (accelerating voltage, tilt angle and distance from specimen to detector) and crystallographic data for the specimen's material, a computer can calculate the orientation of the specimen where the beam strikes the surface.

The EBSD system was coupled to a Leica Stereoscan 200 SEM with the settings of 25kV accelerating voltage; 50μm aperture; probe current of 1-5nA; 23mm working distance and 70° tilt. The ESBD system was supplied by HKL technology and consisted of a low light camera that captures images of the Kikuchi pattern illuminated on a phosphor screen. The video signal is passed to a Hamamatsu Argus 20 image processor where it subtracts the average background enhancing the Kikuchi pattern, which is viewed on a TV monitor. The processed signal is then fed via a frame grabber board to a computer where the acquisition and analysis is controlled with HKL software. The software is able to detect the Kikuchi bands and with crystallographic information can index the pattern. This means it recognises the pattern and assigns a set of Euler angles to that point on the image that describes its orientation. An interaction volume is dependent on the beam diameter, which is dependent on probe current, but the penetration depth is typically less than 50nm. The flow diagram below shows the progression of obtaining the Kikuchi image from the SEM, enhancing the image by subtracting the average background signal, and finally indexing the pattern. The orientation information is stored in a data file to be used by the analysis software.

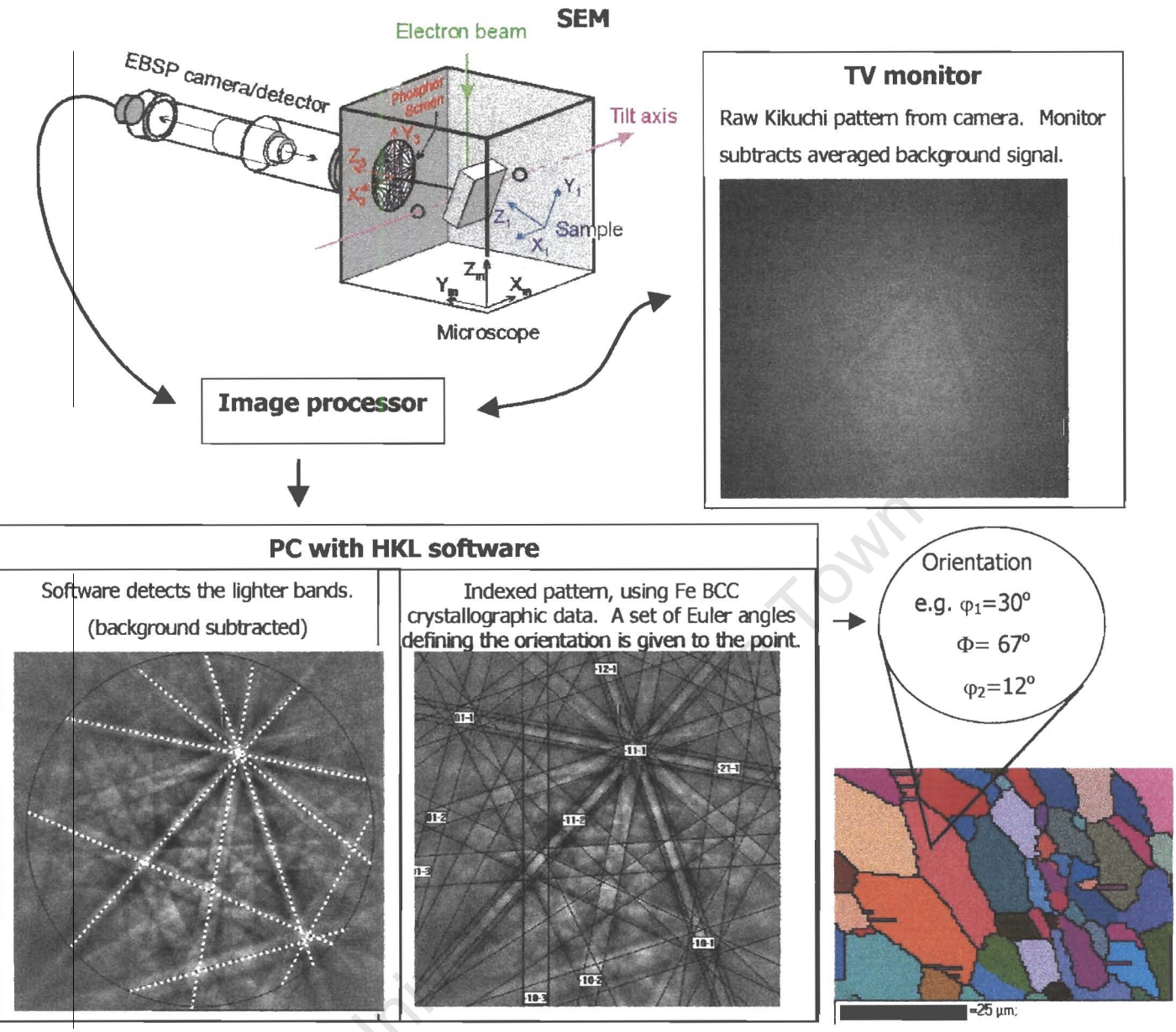

Figure 24. Flow chart of the data acquisition process.

An orientation map can be measured automatically if either the beam or the specimen is shifted and the orientation measured at a stipulated number of points in the X and Y direction. The resolution on the map is dependent on the step size between points and this is chosen by the user together with the number of points in the 'x' and 'y' direction. The software can assign to each set of Euler angles a certain colour and thus a strain free grain with a single orientation will have a single colour. In such a way, the microstructure can be revealed through colour distinction between grains.

The user specifies the size of the map to be measured as well as the step size between points. Resolution is limited to the size of the beam. It is normal for a map to contain a number of unindexed areas where the software was unable to calculate the orientation from the pattern produced at that point. These areas may correspond to points between grains, in pits, areas out of focus or highly deformed regions that produce diffuse patterns. A method of noise reduction is able to assign to these unindexed areas an orientation that is based on a number of neighbouring points being indexed. This number is user defined. The maps produced in this investigation were noise reduced with a conservative six points required to be indexed around the unindexed point. Quantitative information such as textures, grain size, Taylor factors as well as the distribution of each can be computed easily using the data acquired and the associated software. Appropriate work was done on each map.

Maps were acquired to represent the bulk texture in the final annealed state, the detailed microtexture and structure of the through-the-thickness variation in the same material, as well as the latter for the hot rolled material. The size and the step size were adjusted appropriately for each type of map. To gain a clear understanding of the materials characteristics on a micro-scale and how they relate to the ridging results on a macro-scale, a three dimensional image of the microstructure could be developed with a series of two dimensional maps. This, however, would have been too time consuming and a smaller, strategic approach was required. Thus, maps within a single normal/rolling plane were acquired for the investigation of microtexture/microstructure, see Figure 25. This plane would reveal the through-thickness variation as well as the elongation of heterogeneity in the rolling direction.

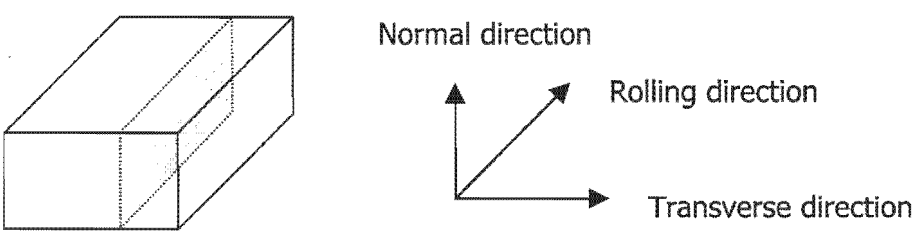

Figure 25. Schematic with shaded plane showing the plane of investigation.

Specimens were prepared in the same way as they were for ECC, since EBSD is also very sensitive to surface deformation that is produced by mechanical polishing.

4 RESULTS

4.1 Ridging Measurements

4.1.1 Tensile Tests

During the tensile tests the specimens of the higher HRFTs did not have sufficient ductility to elongate to 20% strain, with the result that they failed prematurely. The elongation that each specimen achieved, calculated from the elongation within the extensometer where necking did not occur, is shown in Table 4. There was a trend towards lower ductility as the HRFT increased. Ductility is important to these steels considering their applications (see section 2.1.5). Thus, it was decided that since the two higher HRFTs would generally not meet the ductility requirements, the two lower HRFT samples would be examined in detail to explain the different ridging behaviour between them. Results from the 900 samples were also obtained and used for comparisons.

Specimen	Full extension	Strain %	Specimen	Full extension	Strain %
E1000s	✔	20	C1000s	✘	13.3
E1000q	✘	11.8	C1000q	✔	20
E900s	✘	13.5	C900s	✘	19.7
E900q	✘	15.4	C900q	✘	17.8
E800s	✔	20	C800s	✔	20
E800q	✔	20	C800q	✔	20
E700s	✔	20	C700s	✔	20
E700q	✔	20	C700q	✔	20

Table 4. Extensions of the tensile specimens for each sample.

Once the tensile specimens had all been elongated, they were subjected to visual scrutiny to compare the effect of the different variables on the severity of their ridging. Although the visual observation is not quantitative, it was used as an initial comparison since ultimately the ridging quality of the material depends on the aesthetics of the product. From this comparison, it was concluded that there was no

observable difference in surface quality between the samples had been quenched rather than slow cooled. Therefore, the slow cooled samples, as the simpler of the cooling methods, were predominantly used to analyse the influence of other variables on ridging behaviour. Thus, by eliminating the highest HRFT samples and neglecting the quenched samples, the initially large experimental matrix was reduced from 16 to 6 samples to be considered for analysis. The reduced matrix included C900s, E990s, C800s, E800s, C700s and E700s.

The graph below shows the results of the tensile tests on four specimens. These tests were carried out in order to find typical yield strengths of this material. These yield points were used as a guide for calculations involving grain size and Taylor factors in sections 4.2.1 and 4.2.2 respectively. A typical yield value of 340 MPa was used for these calculations.

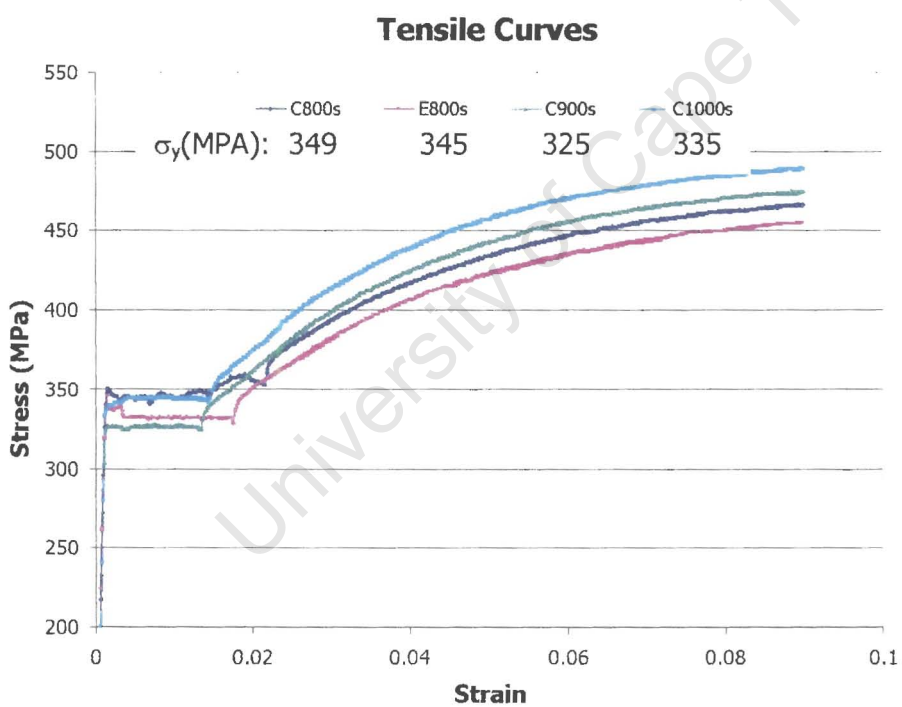

Figure 26. Tensile curves that were used to measure a typical yield strength of this material.

4.1.2 Topography

The measured topography maps are presented in the following figures below highlighting some observations. Firstly, the relative severity of ridging in each of the samples is shown in the maps below, Figure 27, where each map has the same horizontal and exaggerated height scale.

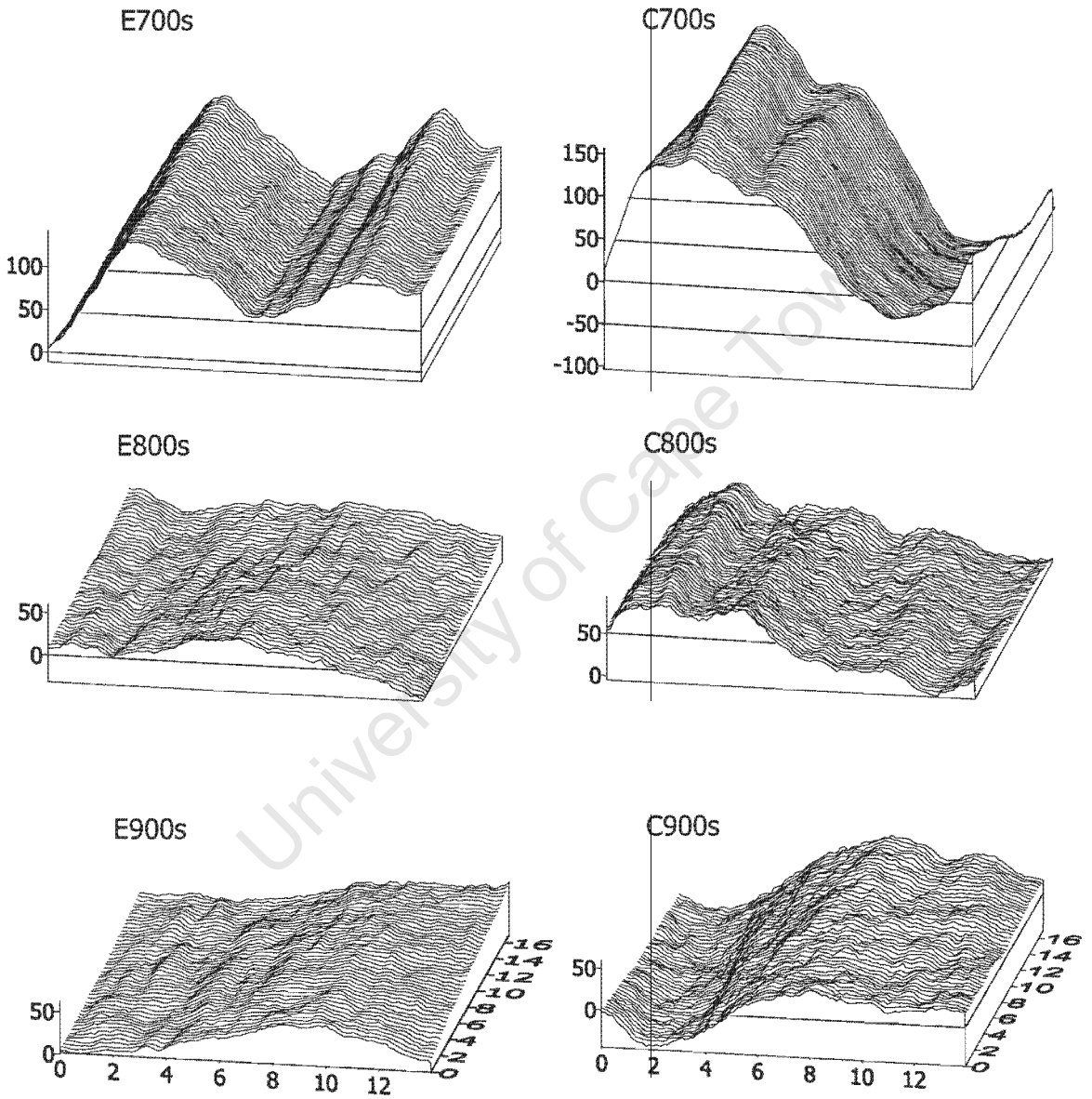

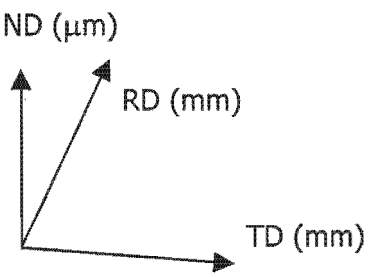

Figure 27. Topography maps representing each of the measured samples, with same exaggerated height scale.

From the above surfaces, a distinction was made between three types of surface roughening effects that were observed. They were distinguished according to their differences in wavelength and length of extension in the rolling direction.

- Warping: In the two 700s samples there is a low frequency, high amplitude distortion of the surface, termed 'warping'. This effect is strongly developed in these two samples but can be noticed, to a lesser degree, in the other samples. The warping effect extends between one and two wavelengths across the measured transverse length (14mm) in the samples.
- Rigding: This distinguishable effect consists of the long parallel undulations superimposed on the warping profile. These undulations extend longer than the measured distance in the rolling direction of 16mm. This effect was called 'ridging' and is observable in the 700s samples as well as the C800s sample.
- Roping: The third effect was termed 'roping' since it resembles the interwoven twine of a rope. It consists of high frequency, low amplitude undulations that extend for a few millimetres in the rolling direction. Roping is developed in all the samples of the two higher HRFTs, 700s and 800s.

All the above effects are extended in the rolling direction. Their combination forms the trend of better surface quality as the HRFT increases.

There is also an observable trend of the columnar samples having more severe ridging than their corresponding equiaxed samples. Together with this trend, the ridging of the columnar samples show a longer wavelength than the equiaxed samples.

The relative roughness was compared on a smaller scale using the smaller detailed maps, Figure 28. The surfaces of the 800s samples are more uneven on the scale of the roping undulations, while the 700s samples both have relativity smooth surfaces on the slopes of their ridges.

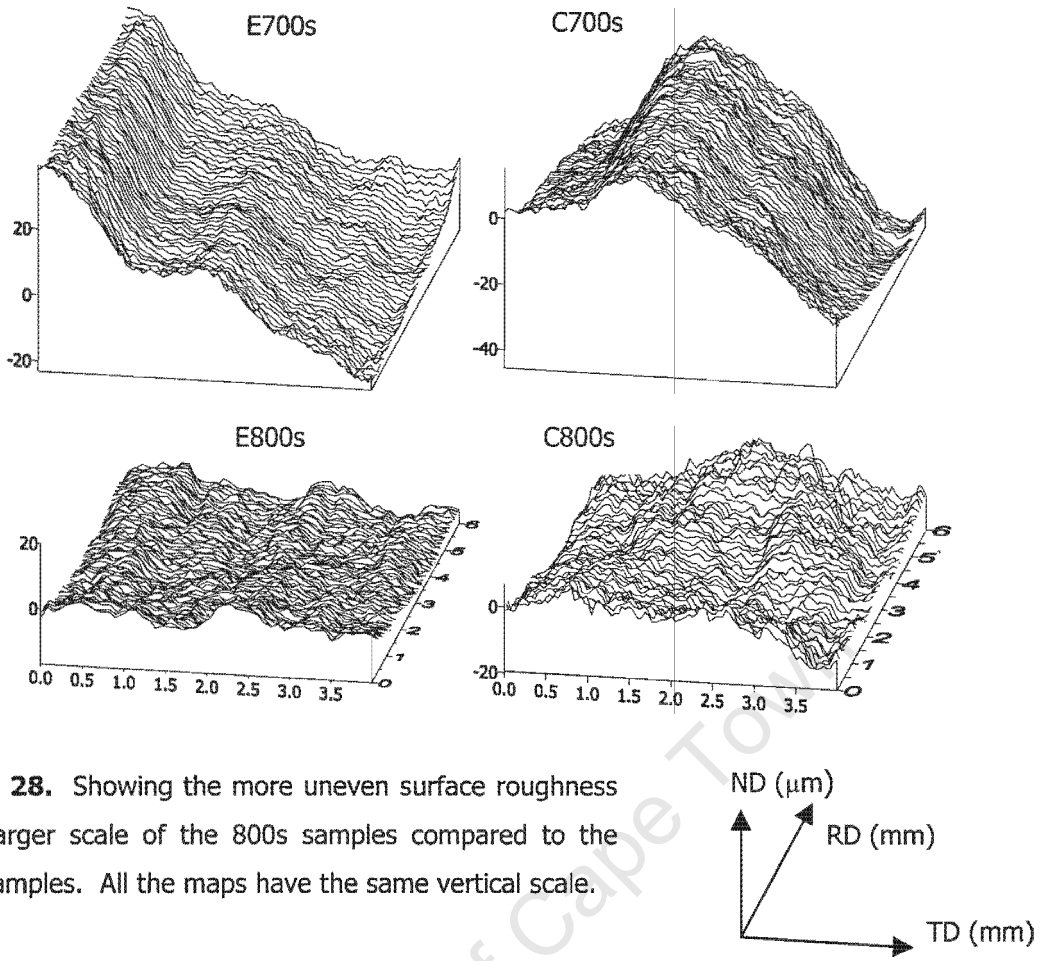

Figure 28. Showing the more uneven surface roughness on a larger scale of the 800s samples compared to the 700s samples. All the maps have the same vertical scale.

The ridging and warping profiles were corrugated effects where the peaks on one surface corresponded to the troughs on the other. The data acquired on the lower surface had to be rotated by 90° around the tensile axis (RD) to compare surfaces. Thus in

Figure 29 below, the maps are aligned so that the material could be imagined to fit between the two surfaces. The fine 'roping' effect, although difficult to observe, did not seem to be an effect that extends through the thickness of the sheet to produce a corresponding profile on the opposite surface.

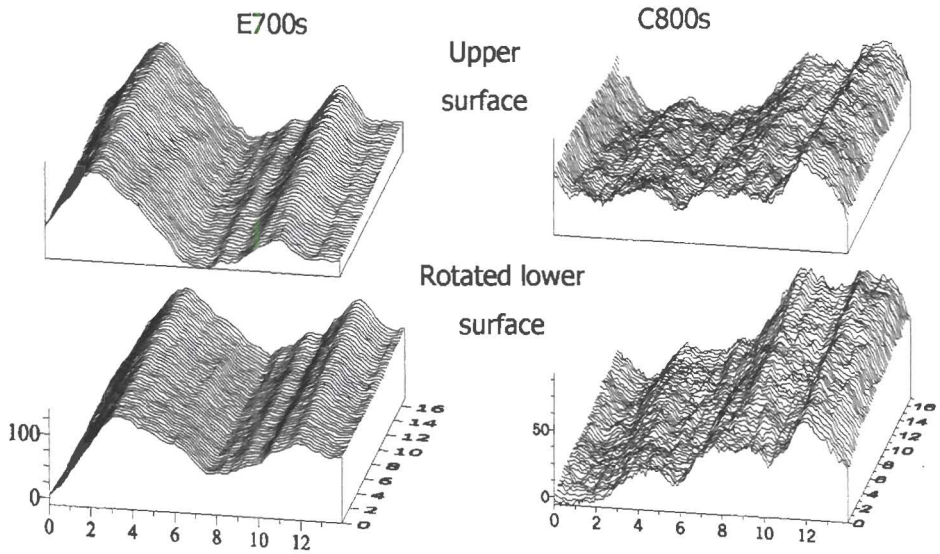

Figure 29. Two samples, E700s and C800s with both their surfaces showing the corrugated ridging.

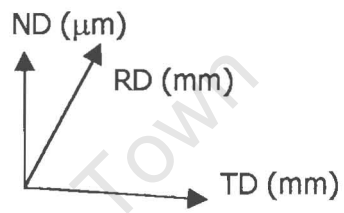

4.1.3 Roughness

The roughness measurements serve to give a reasonable summary of ridging severity of the different samples. Although the ridging frequency was very low for roughness measurements, a long cut-off wavelength of 2.5mm was selected. This cut-off spanned the wavelength of the observed ridges. The trend towards less severe ridging is observed as the HRFT increases. A second, somewhat weaker trend is shown where the columnar samples consistently show more severe ridging than the corresponding equiaxed samples.

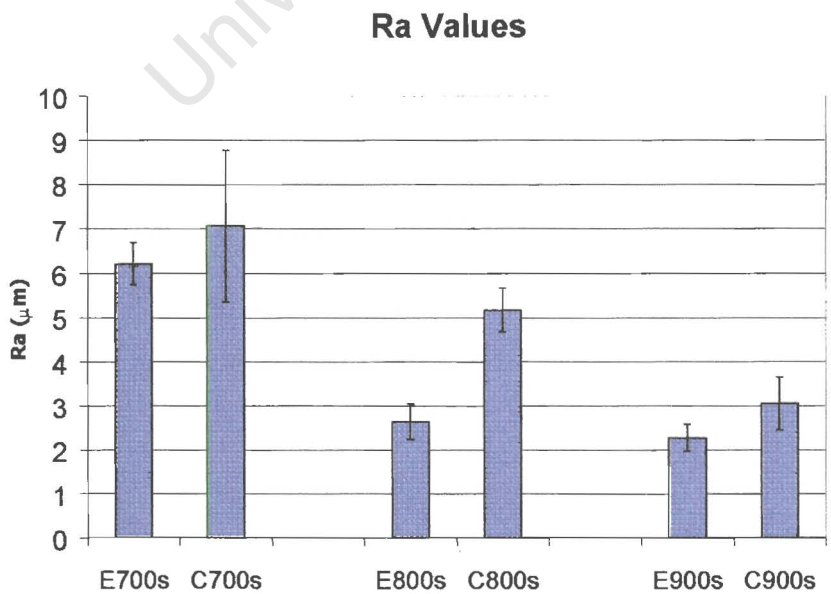

Figure 30. Roughness measurements measured by a profilometer.

4.2 Identifying ridging constituents in the microstructure

The microstructural analysis results are presented here in the same chronological order as the progressive study. Firstly, identifying the constituents in the structure that cause ridging in the final annealed structures. Secondly, they present an explanation, from the microstructures, of the differences in ridging severity between the samples. This section of results examines the microstructural evolution of the samples, starting at the final annealed stage and then the samples after the hot rolled stage. The 700s samples displayed the greatest ridging severity of all the samples, therefore they were used to identify the constituents in the microstructure which, according to previous models, could have lead to ridging. The samples were examined using EBSD giving orientation information as well as grain structure. They were examined in their final annealed state, as this was the state that they displayed ridging after being elongated. The maps Figures 31 and 32 below, represent material from the surface to the centre of the two 700s specimens. Each orientation (defined by Euler angles) on the map is represented by a colour, thus each grain is revealed with a single colour since it has a single orientation. A unique colour is associated with each set of Euler angles, thus microstructure is revealed. Grain boundaries with misorientation >15° are also plotted as black lines.

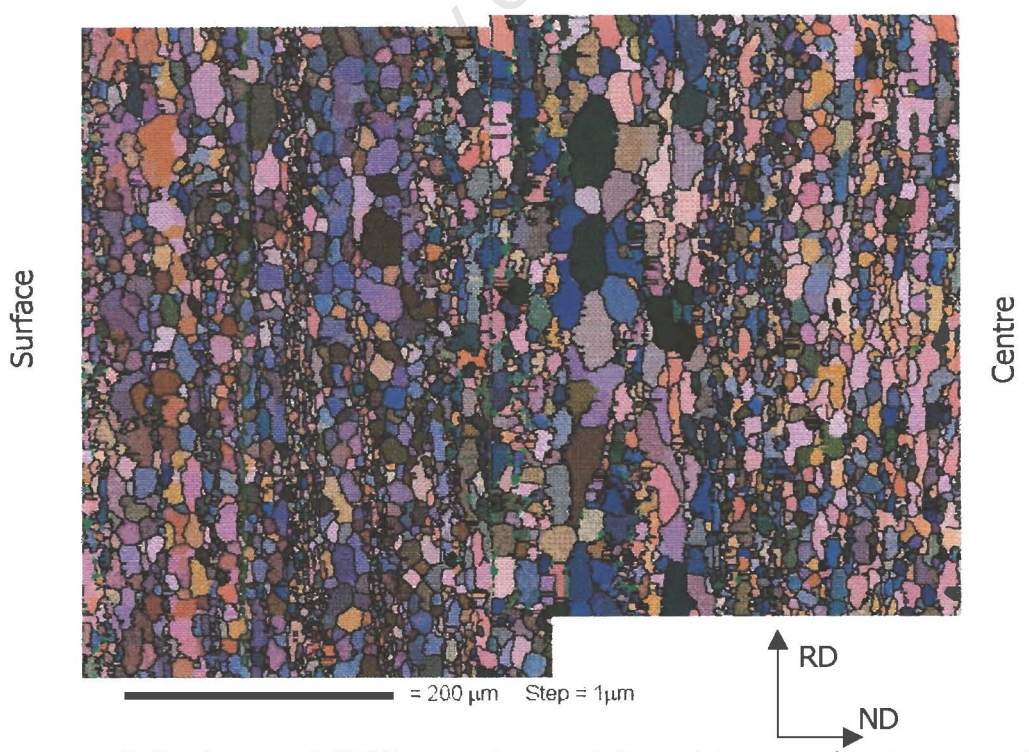

Figure 31. Spliced map of C700s sample, consisting of two overlapping maps that span material from the surface to 0.47 of the thickness of the final annealed sheet.

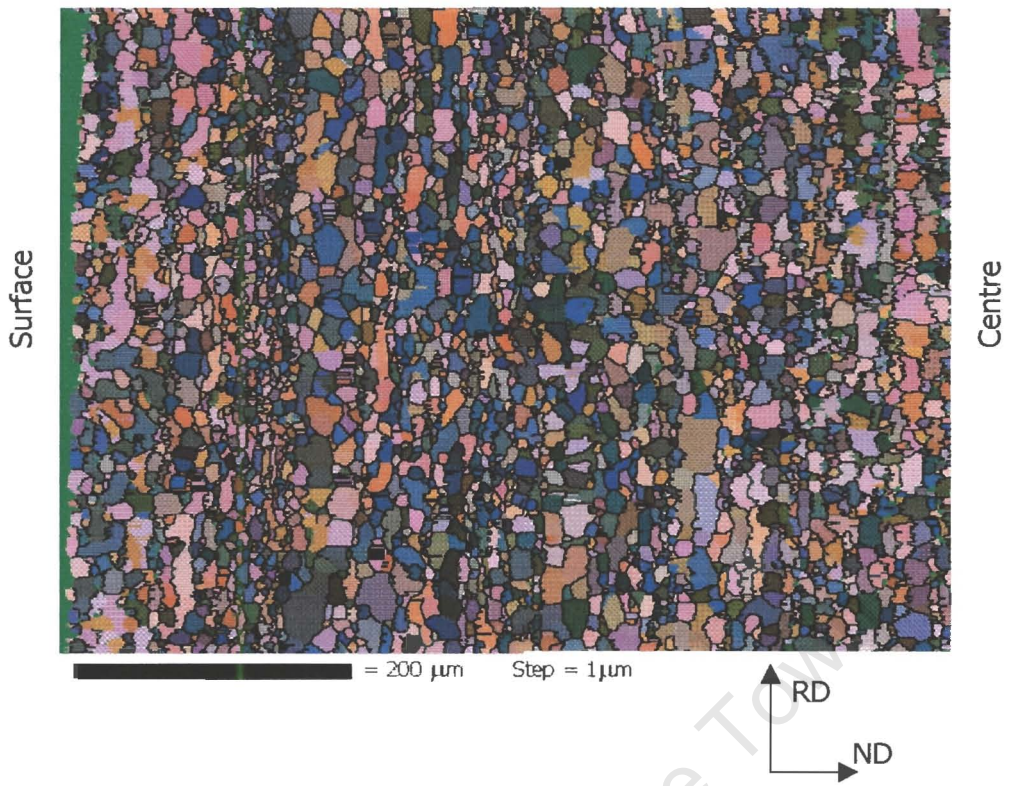

Figure 32. Spliced map of final annealed E700s sample, from surface to 0.51 of the thickness.

4.2.1 Grain size banding analysis in cold-rolled annealed material

From the two spliced maps above, the most noticeable feature in both microstructures is the grain size banding that is extended in the rolling direction. It is especially noticeable in the C700s specimen. Since grain size is related to yield strength by the Hall-Petch relationship, the yield strength was compared for bands of different grain size. This was done by selectively isolating different grain size bands and calculating the average grain size for each band. The grain size was calculated using the EBSD analysis software, which calculates the area of each grain. The average grain size is quoted as the diameter of a circle that has an equivalent area. An example of this method is shown in Figure 33 below using the map measured from the C700s specimen, which showed the most severe grain size banding.

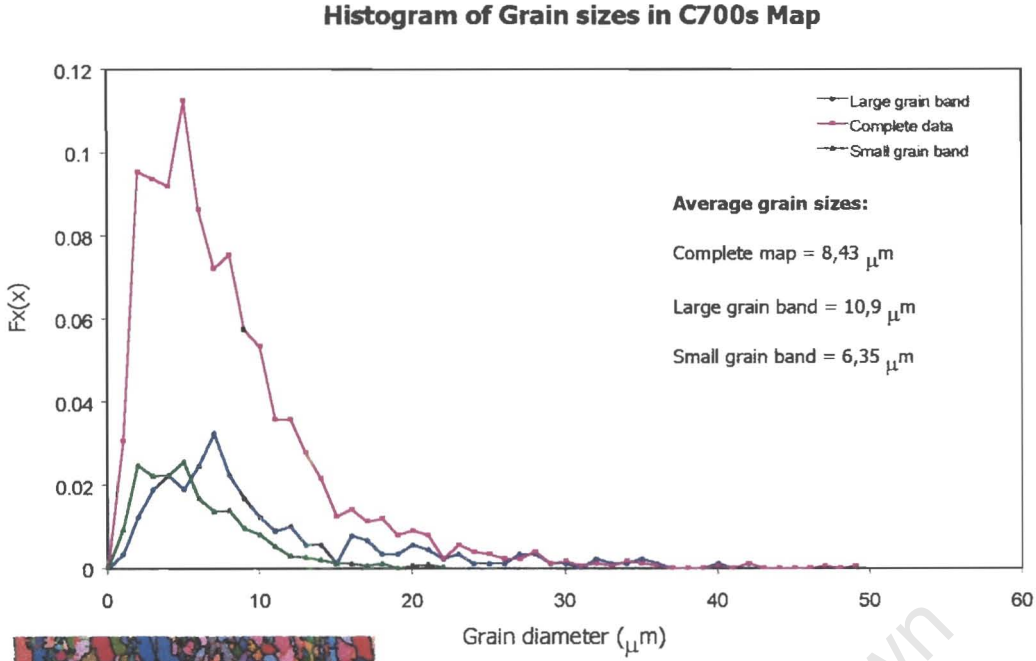

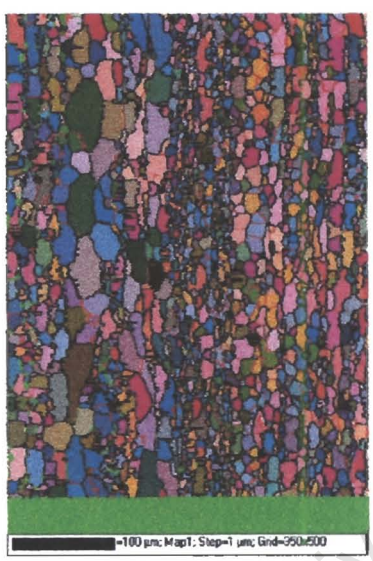

RD

ND

Hall-Petch relation:

$$\sigma = \sigma_o + k_y.d^{-1/2}$$

Friction Stress, $\sigma_o \approx 270$ N.mm^{-2}

(Samples' yield strength in annealed condition measured ≈ 340MPa, average grain size ≈ 8μm)

G.B. resistance, $k_y = 6.57$ N.mm$^{-3/2}$

(Quoted value for ferrite/ferrite boundary interface in duplex stainless steel[4])

Large grain subset

d = 10.9 μm

∴ σ = 333 MPa

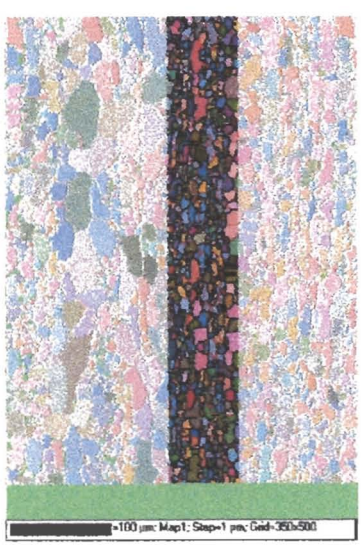

Small grain subset

d = 6.35 μm

∴ σ = 352 MPa

Figure 33. Calculating relative yield strengths in different grain size bands. Achieved by isolating grain size bands, measuring their grain size and calculating yield strength from Hall-Petch relation.

The example above for the C700s sample shows that bands of different grain sizes, which can be adjacent to each other, can have significantly different yield strengths. This difference, calculated in the preceding example to be as great as 22MPa, may be significant in terms of the recent model proposed by Wittridge and Knutsen[14,24]. This model requires bands, elongated in the rolling direction, of different yield properties to develop differential transverse strains during deformation, which, in turn, lead to strain-induced bending.

To relate the extent of grain size banding in the samples to their corresponding ridging severity, a number of qualities of the banding have to be considered in terms of the above ridging model. According to this model, the difference in average grain size between bands, the variation of grain size within each band as well as how coarsely the bands are distributed in the material are all important. Consequently, for this reason, a visual examination of the maps is the best method of comparing banding between the maps and then relating this to the samples ridging severity. The maps of the 700s and 800s samples can be viewed in Appendix 2.a. To show the variation in average grain size in the different samples, the histograms of grain size in the samples, using data from both maps for each sample, are shown below.

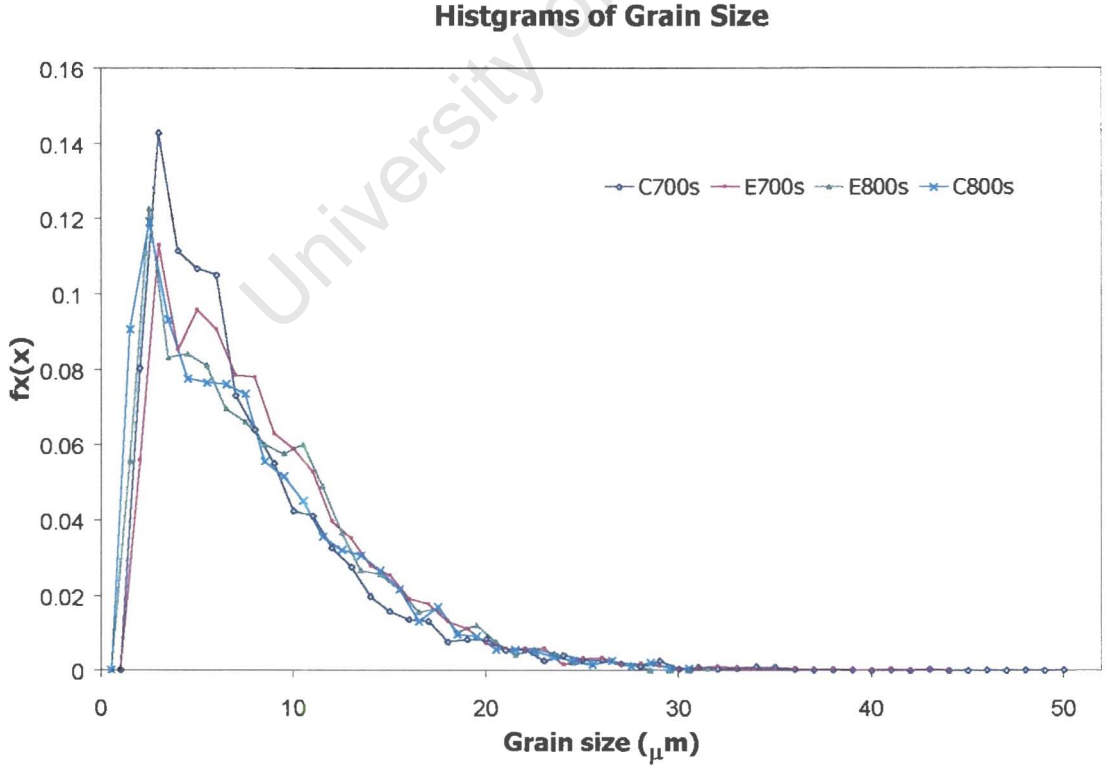

Figure 34. Histograms of grain sizes. Data combined from both maps of each sample after final anneal.

ECC was used to examine the general grain structure of the annealed material. The images obtained displayed a clear correlation between the distribution density of the precipitates and the grain size banding in the microstructure. EBSD is not able to identify precipitates in the microstructure, thus ECC had advantages over the digital technique in this regard. Below are two of the images from the sample that give a clear indication that a fine grain size band is associated with a dense precipitation distribution.

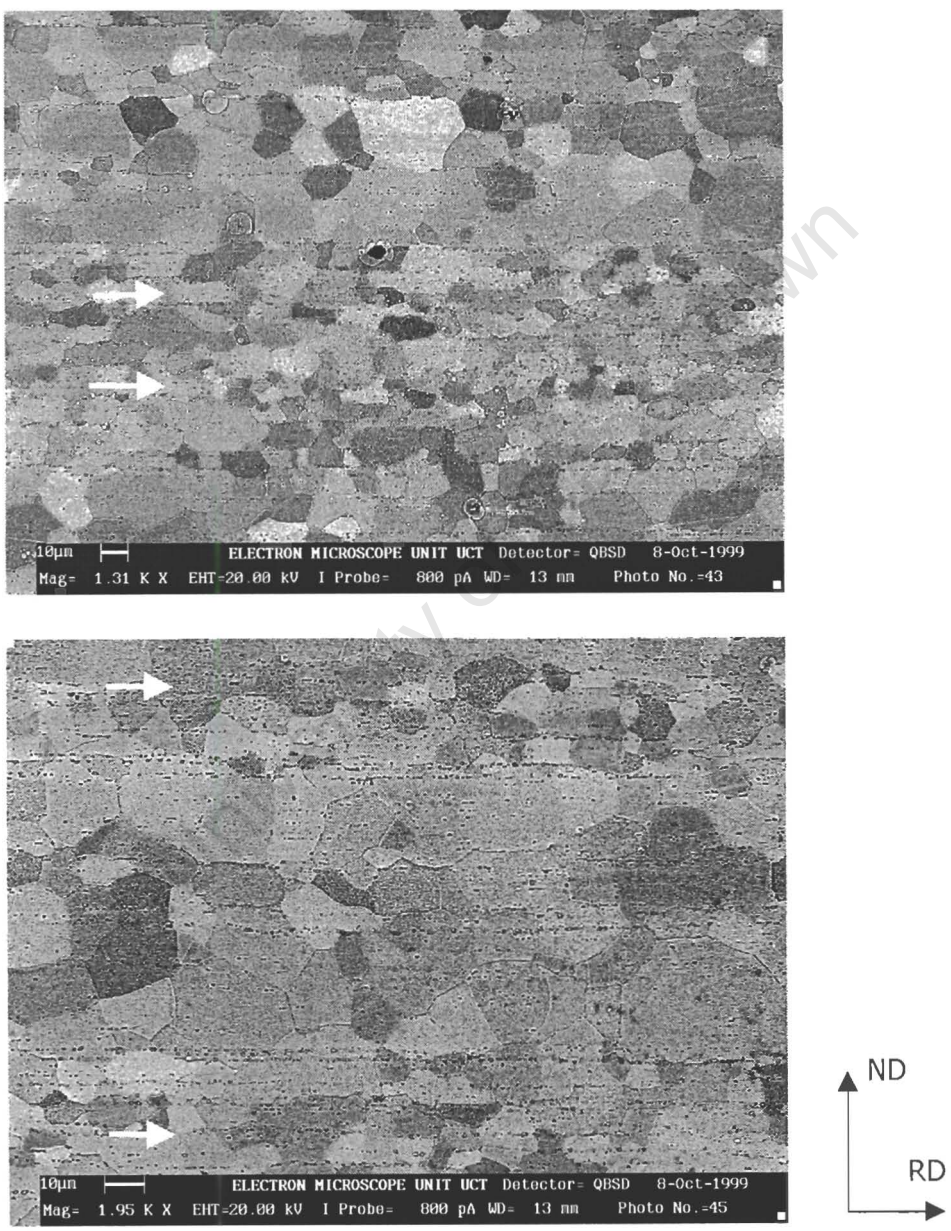

Figure 35. ECC images from E700s sample. Arrows indicating bands, elongated in the rolling direction, of small grain size. These bands are associated with high precipitation density. The precipitate sites appear as dark spots.

4.2.2 Taylor factor analysis cold-rolled annealed material

The second characteristic of the samples that was observed in the maps was their heterogeneous distribution of Taylor factors. This indicates a similarly heterogeneous distribution of yield properties. The Taylor factor can be calculated at each measured point on the map with respect to a prescribed straining direction. Then by assigning to each Taylor factor a shade on a grey scale, a Taylor map can be plotted. Such a map can immediately show variations of yield strengths in a tensile direction across the map since the Taylor factor is directly proportion to the yield strength.

As in the grain size analysis, the Taylor factor analysis started with the samples that displayed the most severe ridging. The C700s was used to observe the distribution of Taylor factors when the prescribed straining direction was in the rolling direction. Such a map, Figure 36, showed a heterogeneous distribution of Taylor factors. The differences in relative yield stresses between bands of different Taylor factors were calculated using the average Taylor factor in each band and the typical critical shear stress (τ). The latter was approximated by using the average Taylor factor measured in the maps, found to be 2.97, and the measured yield strengths from tensile tests, approximately 340 MPa.

The maps of Taylor factors for the spliced maps of 700s and 800s samples can be viewed in Appendix 3.

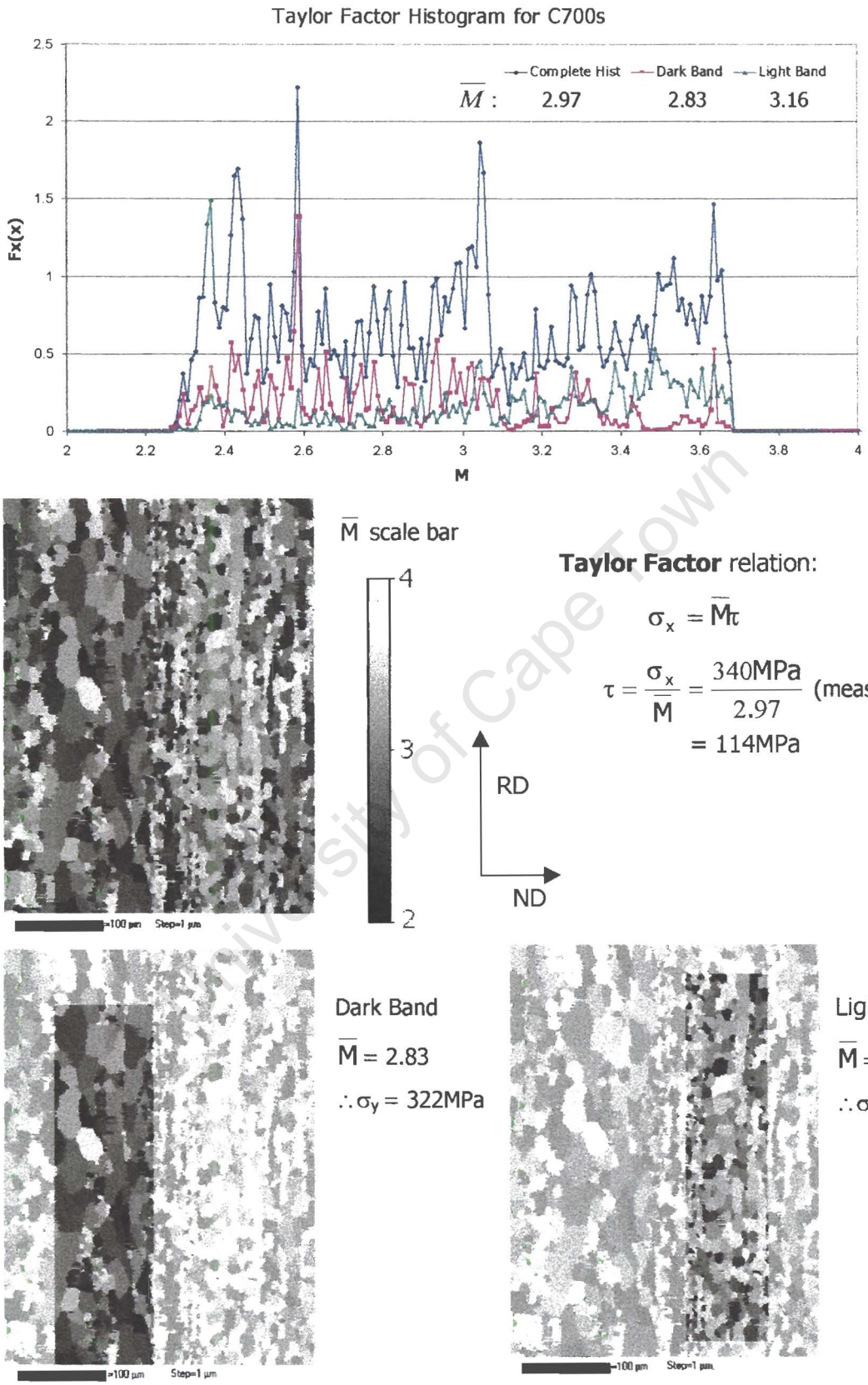

Figure 36. Calculating the difference in relative yield strengths between bands of different average Taylor factors. The bands are isolated into subsets of the map and their average

Taylor factors, $\bar{M}$, are calculated. This figure was used to calculate the yield strength via the Taylor relation.

Since the Taylor factor is dependent on orientation, the bands of different Taylor factors were investigated to find the types and extents of preferred orientations present in each. This was done for the C700s map by plotting the pole figures of the subsets selected in Figure 37 above, and finding the intensities and types of textures in each. The pole figures of data were plotted for the {111}, {110} and {100} sets of planes relative to the rolling geometry.

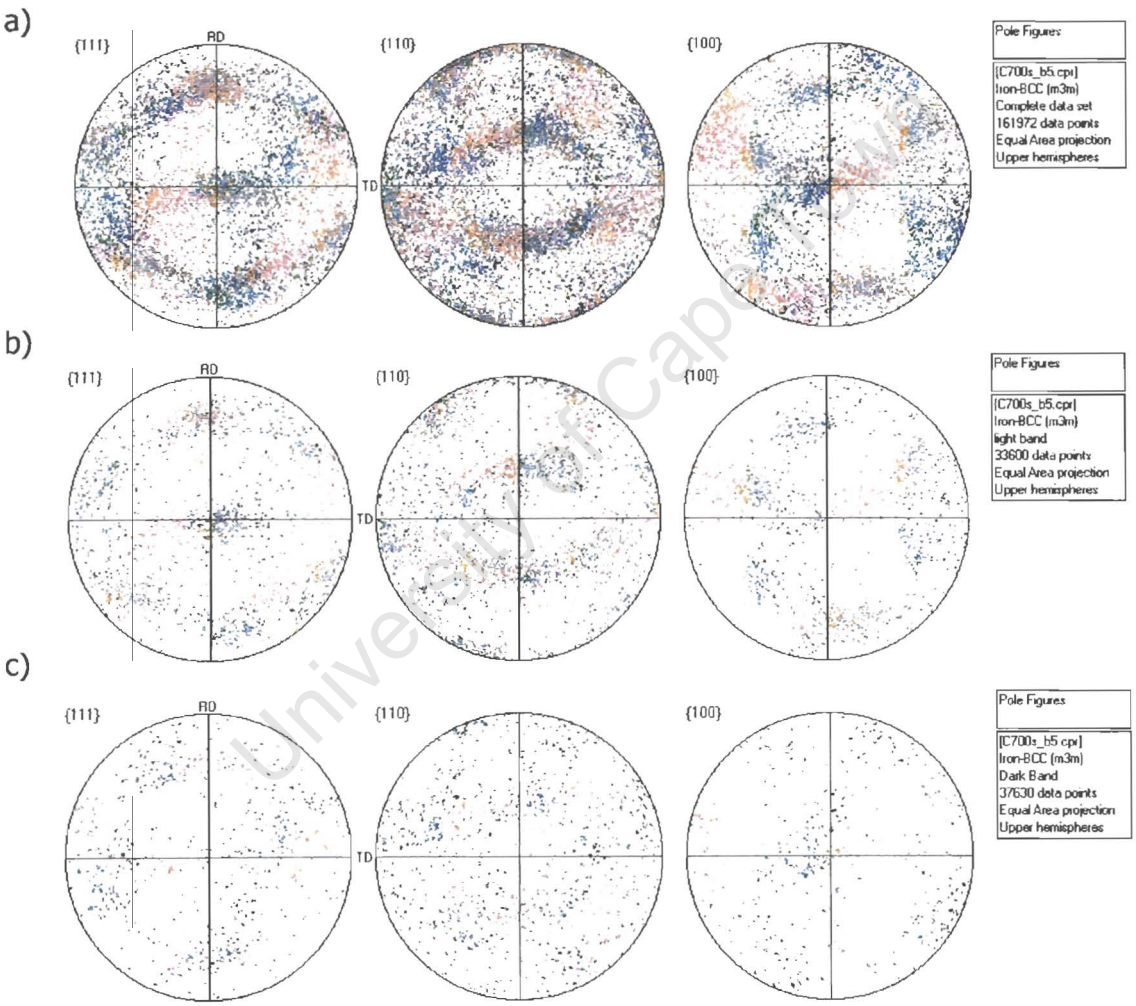

Figure 38. Pole figures for the C700s sample showing data of a) the complete map, b) the light band of high values of $\bar{M}$, and c) the dark band with lower $\bar{M}$ values.

These pole figures show that while the light band has fewer data points than the dark band subset, as well as a higher number of grains, the points are more clustered. This suggests that it is more textured than the dark band. The α-fibre

and γ-fibre textures were identified as being predominant in this sample. The light band shares the same predominant textures in intensity, while the dark band has a more random orientation distribution.

A similar examination of the orientation distributions in the Taylor bands of the E700s sample is displayed below. The bands that are examined are found in the map closest to the surface where the textures were influenced by the shear rolling texture of the η-fibre. From these and other similar examinations of the texturing in the Taylor bands, it is generally observed that a band of high average $\bar{M}$ has strong α-fibre and γ-fibre, or α-fibre and η-fibre components. Whereas, a band of low $\bar{M}$ values has more random orientations.

a)

b)

c)

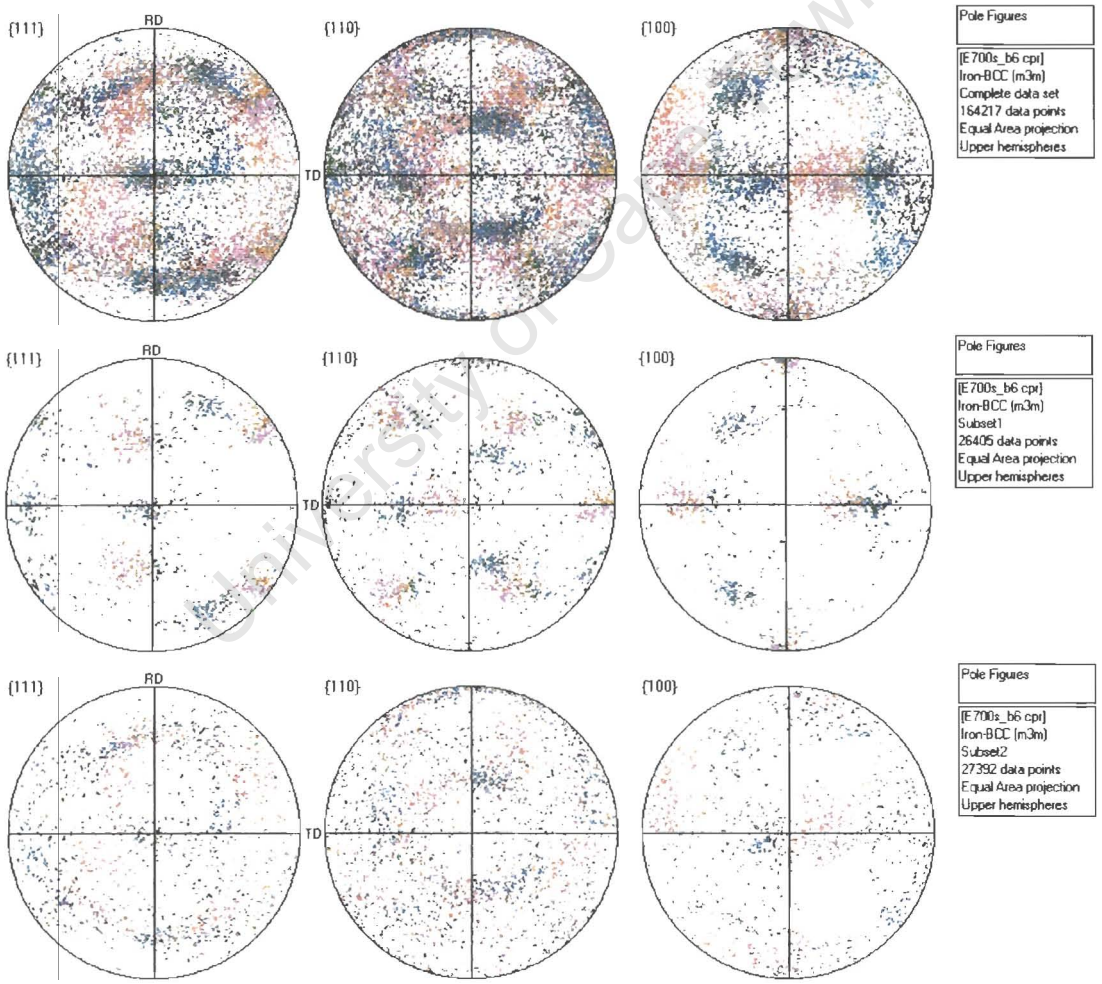

Figure 39. Pole figures from the sample E700s of a) the entire surface map, b) a band of high $\bar{M}$ values with strong Goss and {111}<110> textures, and c) a band of lower $\bar{M}$ values with more random orientation distribution.

By combining the data for both maps of the E700s and C700s samples, their orientation distribution functions (ODF's) could be plotted with a large enough representation of material, see Figure 39 below. The ODFs give an unambiguous representation of the types and strengths of textures present in the material. The ODFs were calculated using the series expansion method and sections were plotted with constant ϕ_1.

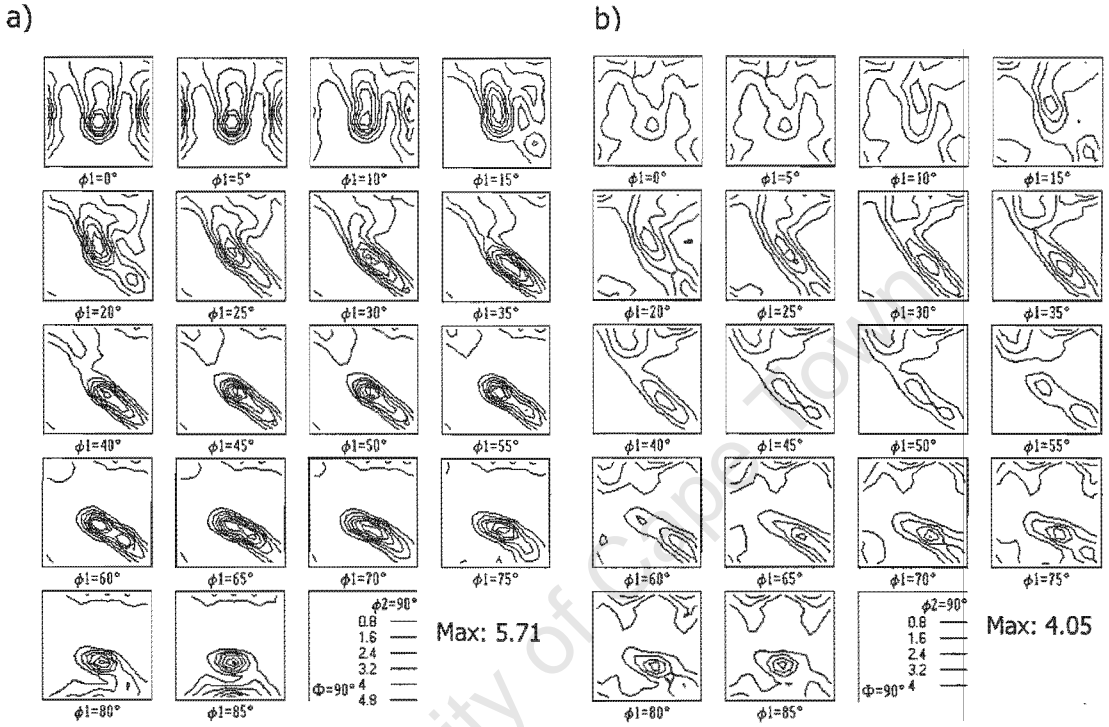

Figure 39. ODFs with maximum contour strengths of the combined maps for a) E700s and b) C700s.

Both maps show essentially the same textures present, namely the typical rolling textures of α-fibre and γ-fibre as well as the shear texture η-fibre with a maximum at the Goss orientation of {110}<100>. However, the E700s map has a higher corresponding texture intensity, with a maximum of 5.71, compared to the C700s sample, with a maximum of 4.05.

4.3 Hot Rolled Structures

After the variation in final annealed structures was observed, the variations after the hot rolling stage were examined to gain an understanding of how the samples differentiated from each other during the TMP.

4.3.1 EBSD

The hot rolled structures were reduced to 90% and contained high degree of stored deformation energy. This deformation was not conducive for EBSD since the pattern quality was too poor. For this reason the 700°C and 800°C samples were given a stress relief treatment at 600°C for 1 hour to allow the material to recover; however, the lower HRFT samples did not show a significant enough improvement. The maps that cover the area from surface to centre are given in Figure 40 below, all with the same orientation and plane of view as indicated.

These maps show that the microstructure has recrystallized during the hot rolling treatment when their grain size and aspect ratio are considered relative to the initial cast structure. The starting grain size in the equiaxed samples was around 2 mm while the columnar samples had a starting grain size averaging 7 mm in length and 2 mm wide (see section 4.4.1). Using the EBSD analysis software, a calculated grain size measurement of these maps yields a far smaller result than expected. This is because deformed maps such as these contain many unindexed areas, discontinuous grain boundaries and small grains around grain boundaries that are not distinguished as bad data. Therefore, a manual estimate of the grain size was made using data displayed for each grain. The E800s sample had an average grain size of 100-200 μm, with smaller grains at the surface, while the C800s sample had an average of 150-300 μm, both an order of magnitude smaller than the starting grain size. All these grains had an aspect ratio between 2 and 12. If no recrystallization had taken place then the grains in each map would be far larger with an aspect ratio of around 100, when considering that the samples were rolled to 90% reduction with minimal lateral spread of material.

The unindexed areas are where too few bands were detected to enable the orientation of the points to be measured. These areas on the map may correspond to areas of high strain on the sample, areas between grains or areas that are martensite. The martensitic areas can be distinguished if the unindexed area is elongated in the rolling direction as a stringer with the same characteristics that were observed using ECC.

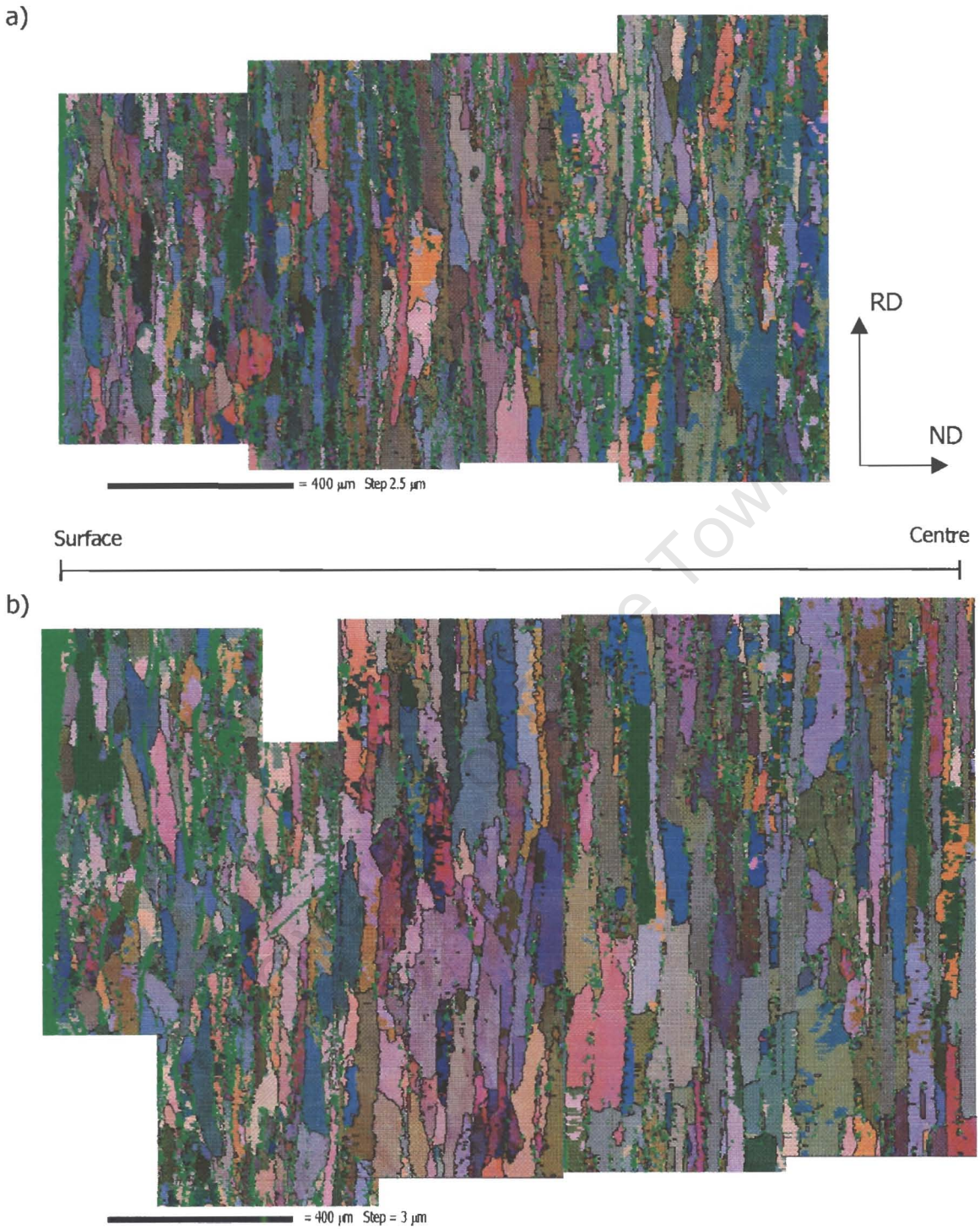

Figure 40. Spliced EBSD maps of a) E800s and b) C800s samples in their hot rolled condition.

Since the 700s specimens could not be mapped using EBSD, the E900s sample was used to compare maps of different HRFT. The specimen used for EBSD mapping was also stressed relieved at 600°C for an hour before being mapped.

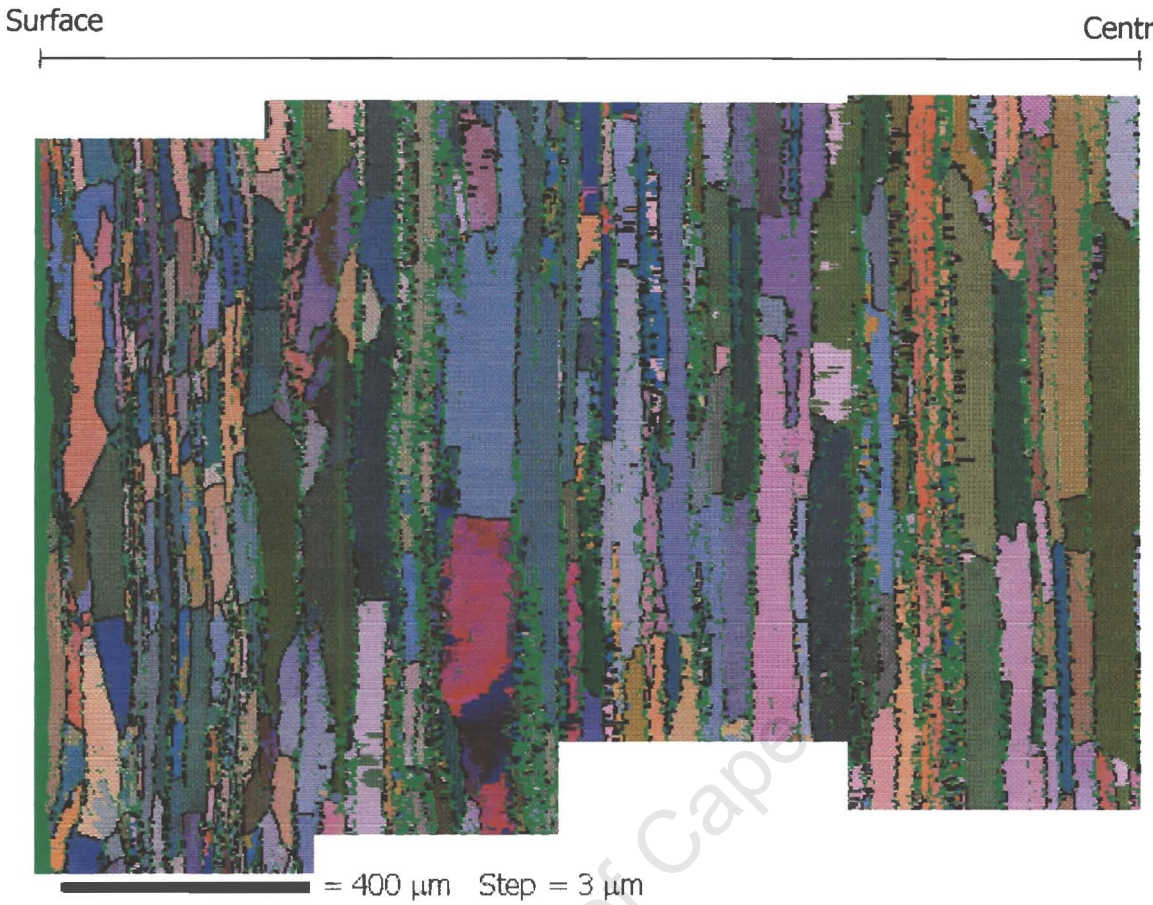

Figure 41. Spliced EBSD maps of the E900s sample from its surface to centre.

The 900s maps, when compared to those of the 800s samples, show a greater average grain size in the higher HRFT samples. The grain size also varies within the specimen probably due to the distribution of austenite during rolling. The unindexed areas are largely contained in bands extending in the rolling direction that correspond to highly dislocated martensite. There is a higher percentage of martensitic bands in the 900s sample, Figure 41, compared to the 800s samples, Figure 40.

4.3.2 Electron Channelling Contrast

The images obtained using ECC were, like EBSD, very sensitive to deformation. The images obtained from the 700s samples did not reveal any distinguishable features due to their high degree of deformation. However, the 800s samples had recovered sufficiently to be useful ECC specimens. These images, Figures 42 and 43, were

used to identify and explain features that were observed under a light microscope after electroetching the same samples. These light micrographs are displayed in the section 4.3.3.

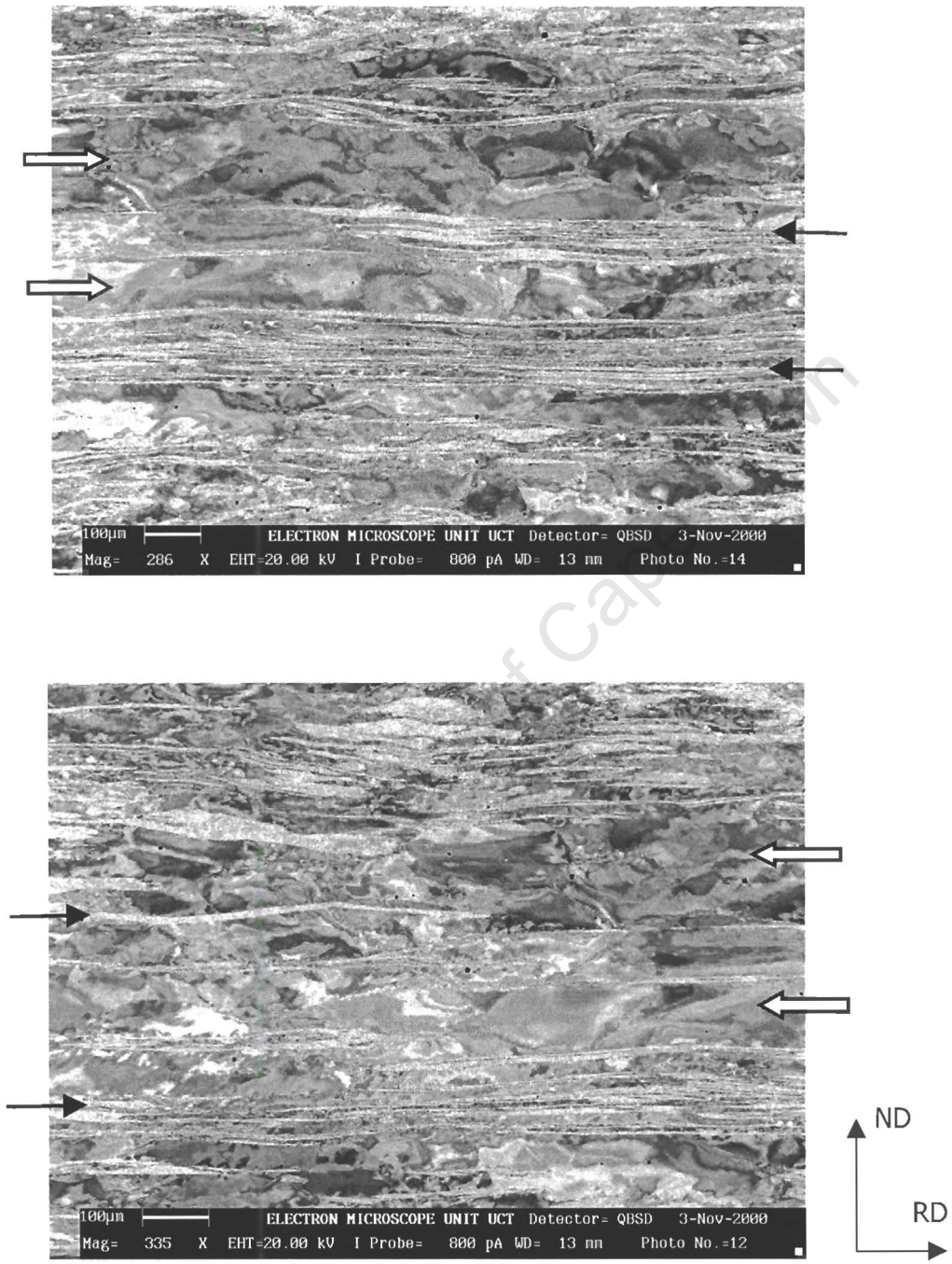

Figure 42. Two ECC images of sample C800s. The small arrows point to some martensite stringers that are elongated in the rolling direction and with a light grainy shade. The block arrows indicate regions of ferrite between the martensite that is partially recovered with a 'mottled' contrast.

a)

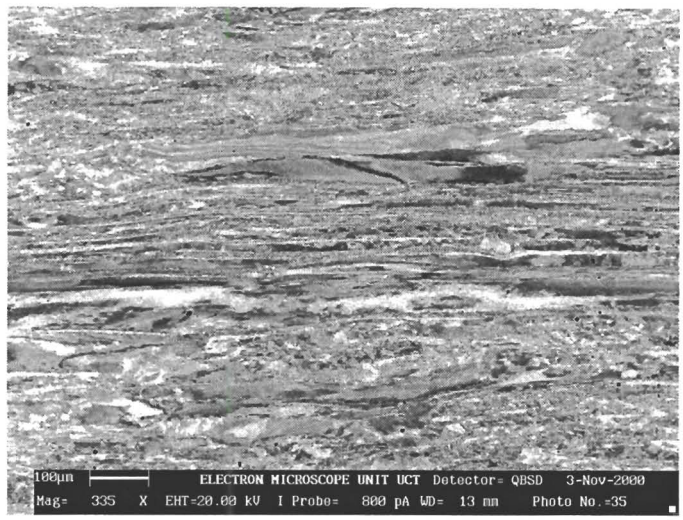

b)

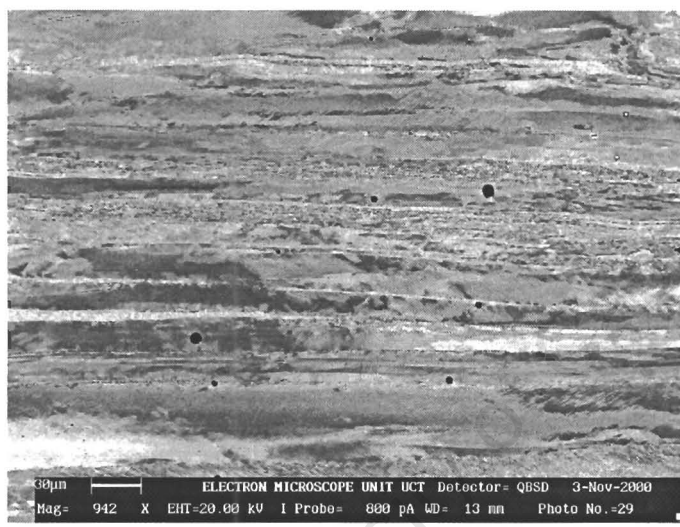

c)

Figure 43. ECC images of the E800s sample with progressively greater magnification in a), b) and c). The features in these images are finer than those in the C800s sample. With increasing magnification, bands of fine substructure that are precipitate rich are observed, as indicated by arrows.

The preceedng images show that in each case the microstructure is divided by bands of martensite, as in the C800s sample, or precipitate rich bands with fine substructure, seen in the E800s sample. The microstructure of the C800s sample is coarser than the E800s sample.

4.3.3 Light Microscopy

The light micrographs below rely on the etching artefacts to reveal the microstructure. The etching is dependent on the phase present as well as the strain and composition of the structure. In this regard, the ECC images and microhardness helped in interpreting the structures observed in the light microscopy images. Both the 700 and 800 series of samples were investigated, although, as in the ridging results, little difference was observed between those that had been quenched only, and those that had been quenched and slow cooled. Colour was retained in the micrographs to help in distinguishing between the features. All the micrographs presented were taken from the same plane of the rolled sheet, namely the rolling/normal plane. The orientation of all these micrographs are the same as that indicated in Figure 44.

These micrographs give evidence to suggest that, during hot rolling, there was austenite present which subsequently cooled to form martensite. During rolling though, the austenite, having a greater hardness than ferrite at high temperatures, partitioned strain energy to the surrounding ferrite, characterised by a darker colour with a higher density of subgrain boundaries. The average temperature of the material cooled around 200°C over the complete rolling procedure. As it cools below the A_1, the driving force for transformation of the austenite to ferrite increases. This results in the partial transformation of austenite to a softer, less strained ferrite from the outer boundaries towards the centre. A remnant of austenite is left at the centre that transforms to martensite after rolling at a lower temperature.

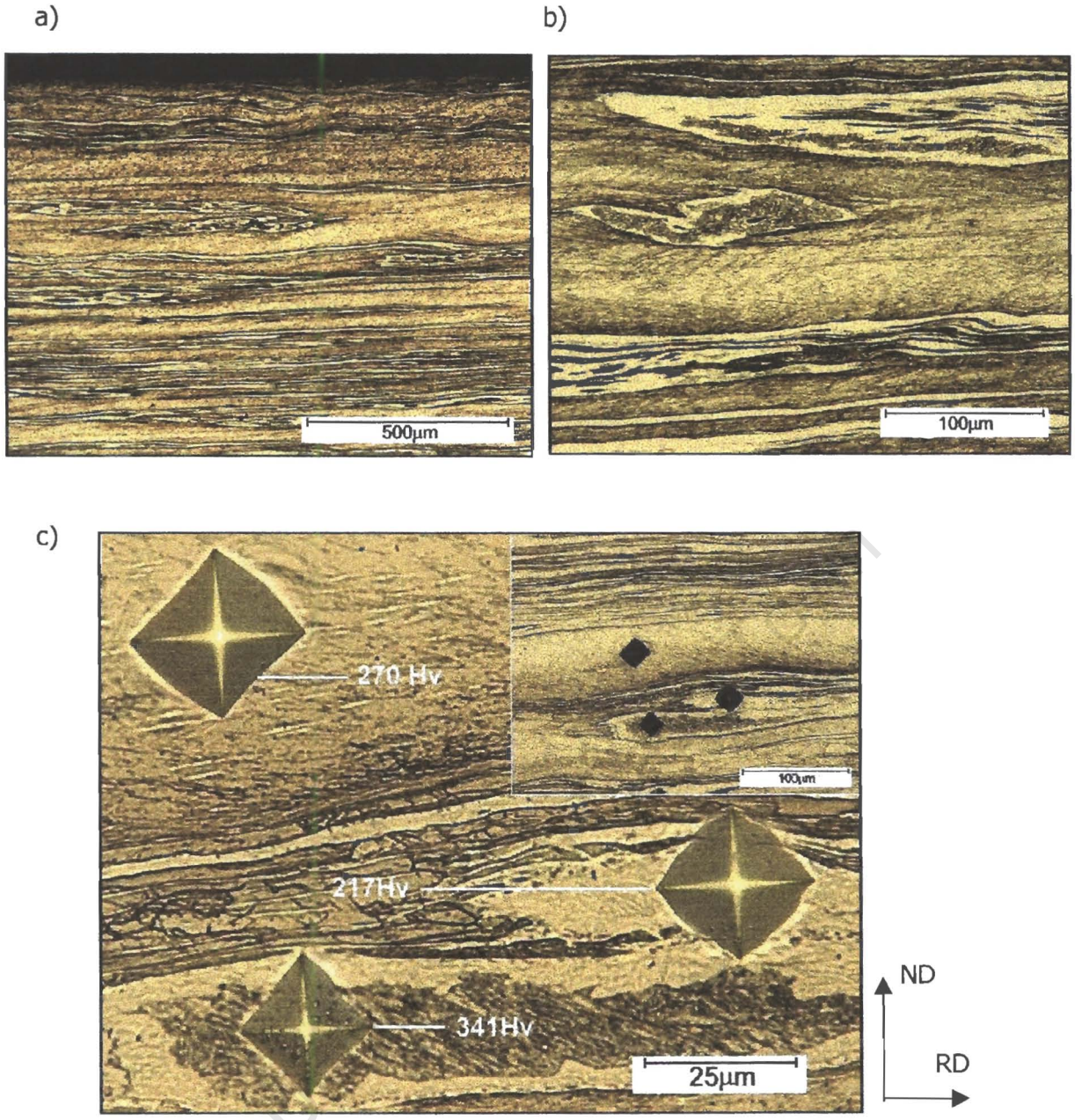

Figure 44. Micrographs of a) E700s and b), c) E700q. a) Shows the surface of the material (top), and light coloured stringers extending in the rolling direction. b) Light stringers under higher magnification showing martensite on their interior. The subgrains are represented in the ferrite by veiny lines. c) Three microhardness indents within martensite, 341 HV, within the strained ferrite, 270 HV, and within the less strained, lighter coloured, ferrite that surrounds the martensite, 217 HV. The insert, top right, shows the region of material where the indents were taken.

a) b)

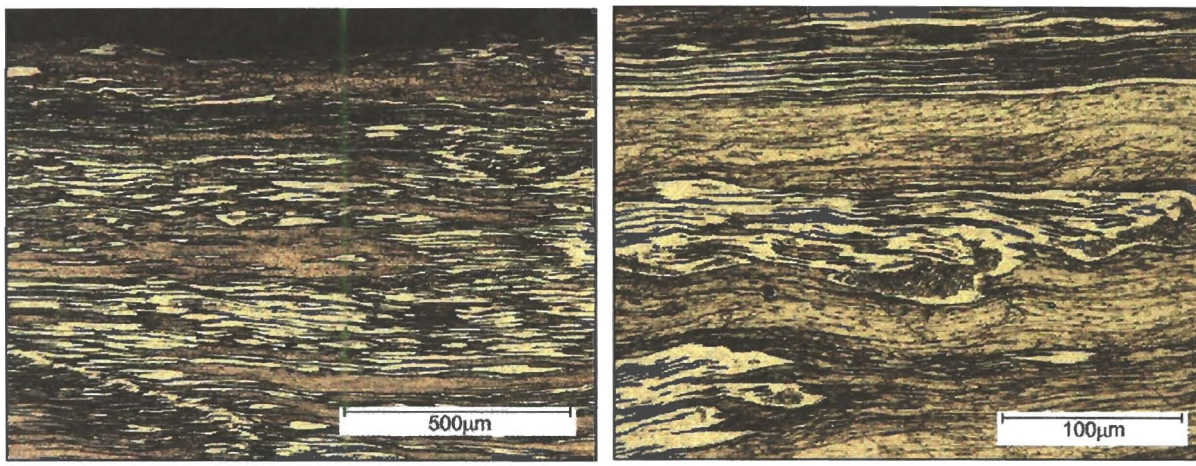

Figure 45. Micrographs of the C700s sample under two magnifications a) low, showing the surface of the material, and b) higher magnification.

a) b)

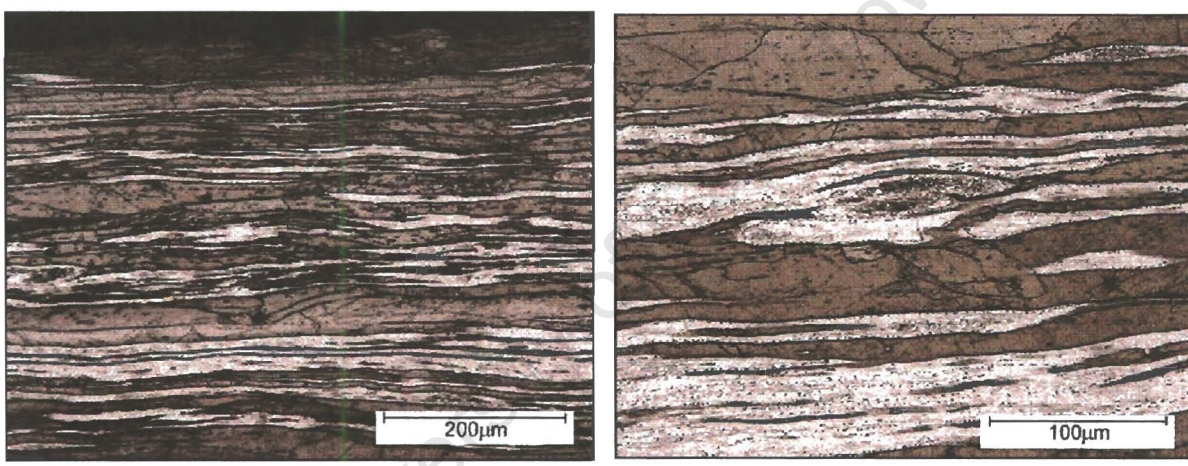

Figure 46. Micrographs of the E800s sample with the surface at lower (a) and higher (b) magnification. The lighter coloured prior austenite stringers contain a higher degree of precipitates.

a) b)

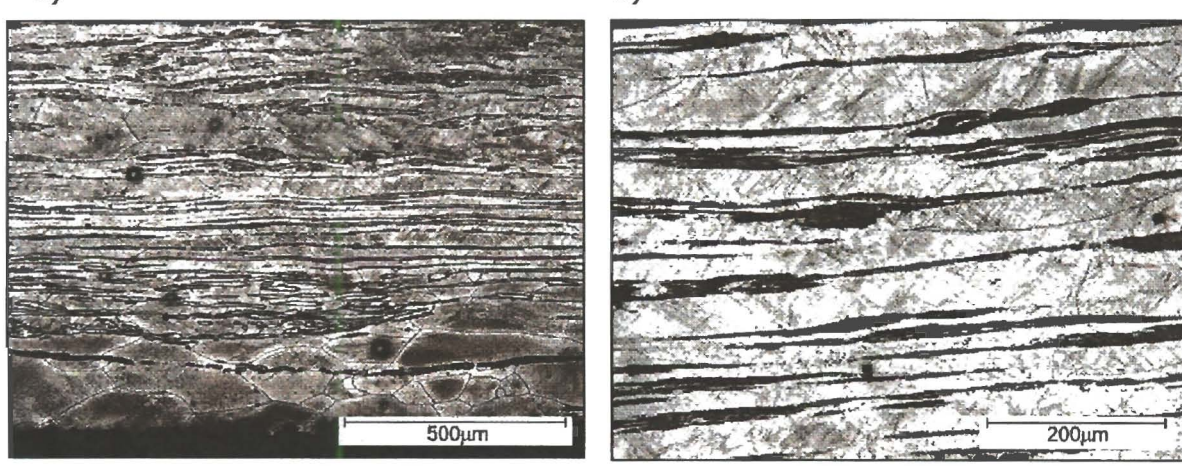

Figure 47. Micrographs of the C800s sample under low (a) and higher (b) magnification.

The features observed in Figure 45, Figure 46 and Figure 47 were observed and discussed in Figure 44. The E800s sample in Figure 46 can be compared to the ECC image in Figure 43, where bands of fine, substructured material with a high density of precipitates correspond to light coloured stringers that also contain many precipitates. Therefore, the above images confirm the fact that some austenite in the samples transformed back into ferrite and precipitates during either the rolling cycle, in the case of the 700 samples, and/or during cooling. [The dilatometry data measured (section 4.4.3) show that with a cooling rate of 2°C/min the Ar_1 temperature is 788°C and with a greater average cooling temperature during rolling this temperature may be suppressed further to a lower temperature, perhaps to 700-750°C].

By a visual estimate, there is a smaller amount of austenite in the 700 samples than the 800 samples, and there is more martensite present in the C800s sample compared to the E800s sample. The latter is probably due to variations of temperature during hot rolling. The martensite distribution is also generally coarser in the columnar samples compared to their equiaxed equivalents; this was also observed in the ECC images. Two micrographs, Figure 48, of the 900 samples display this difference of martensite distribution between the columnar and equiaxed samples below. The columnar samples can show bands with a high density of martensite stringers adjacent to material with a low martensite content. The variation in martensite distribution within the equiaxed samples is not as vast.

a) b)

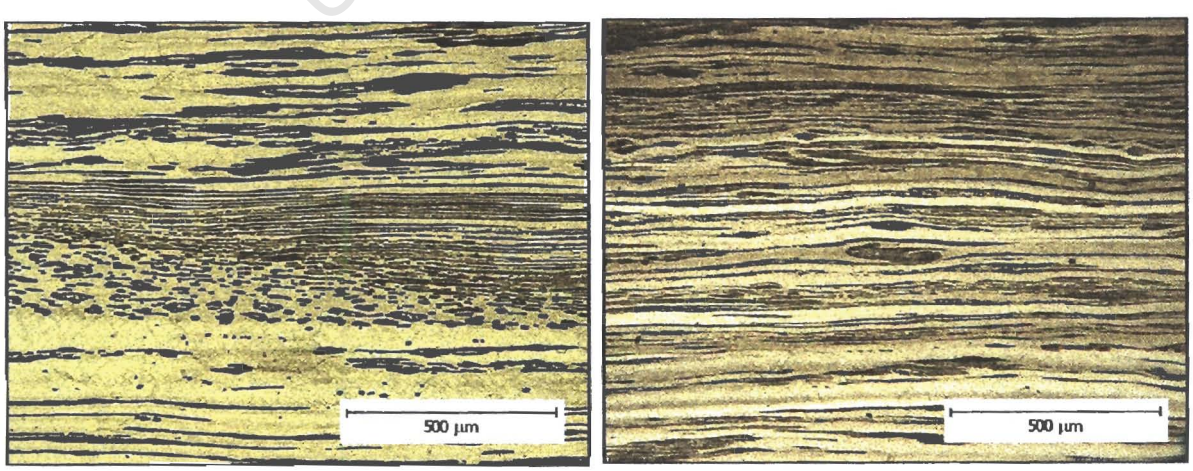

Figure 48. Two micrographs, with same magnification, showing martensite distributions in the a) C900q and b) E900q specimens.

4.4 Miscellaneous Measurements

4.4.1 Starting structure grain size

Grain size of the initial cast structures were made using a macroeteched sample of the cast slab, Figure 49. The line intercept method was used to calculate the grain size within the equiaxed region and the columnar region. The lines of measurement were aligned in the rolling direction and the normal direction to obtain the aspect ratio in each region. A minimum of 16 measurements was taken for each result and the averages are quoted below in Table 5.

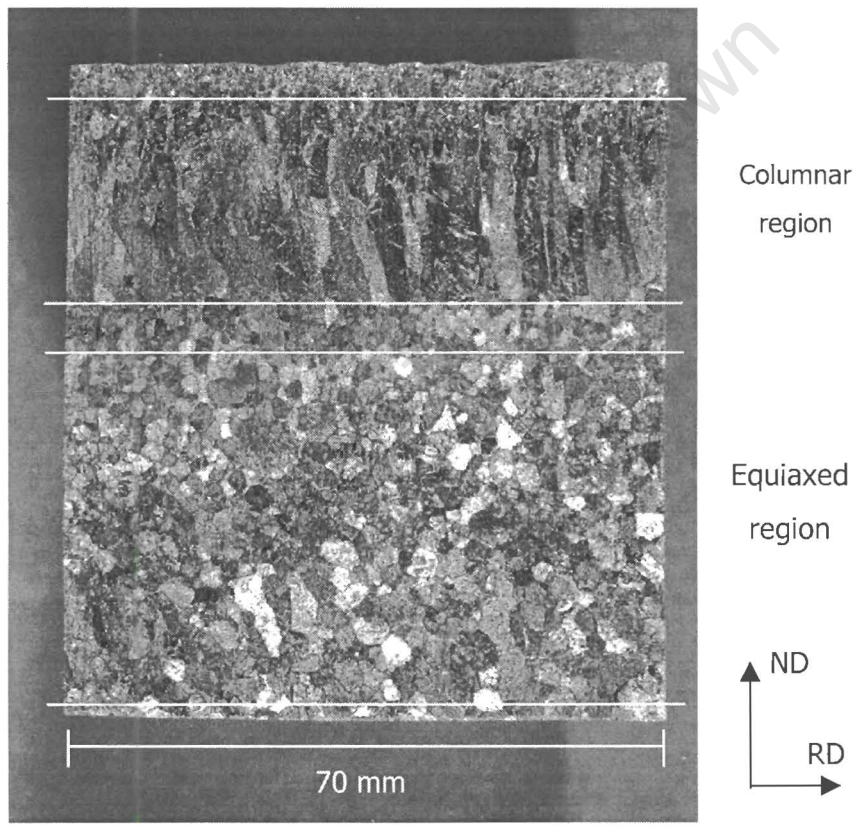

Figure 49. Macroetched cast structure used for grain size measurement.

	Columnar Region	Equiaxed Region
Grain size in RD (mm)	2.12	1.96
Grain size in ND (mm)	6.78	2.15
Aspect ratio	3.20	1.10

Table 5. Results of the line intercept measurements of the cast structure's grain size.

4.4.2 Hardness

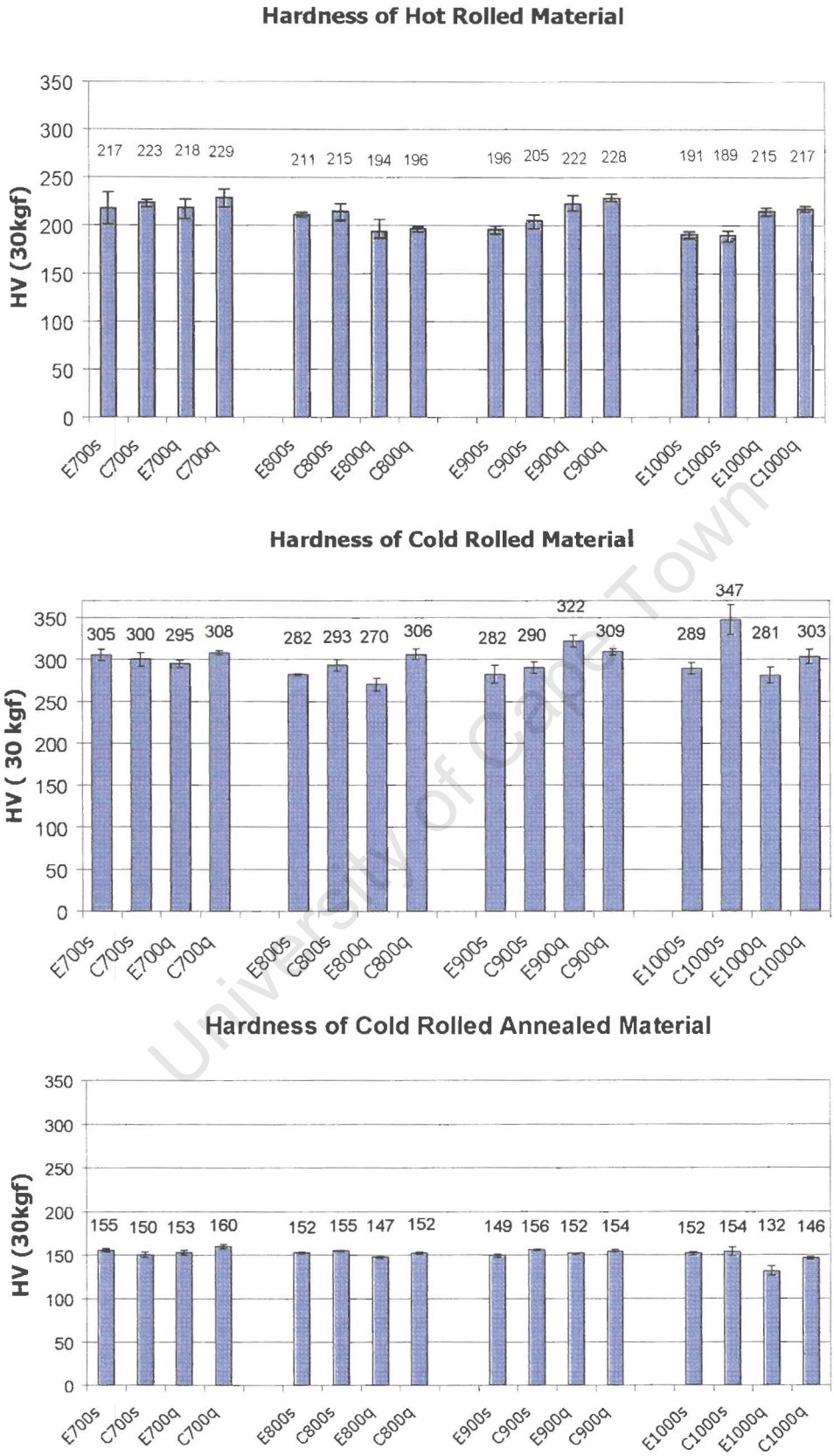

Figure 50. Three hardness measurements on each sample after a) hot rolling b) cold rolling and c) final annealing.

There is little discernible difference between the samples' hardness at each stage. The hardness increases after cold rolling and drops to almost half that value after final annealing, which is to be expected since new strain-free grains would have replaced the harder strained ones. An increase in hardness was expected with decreasing HRFT, since at lower temperatures the material would recover less and withhold more strain energy. This expectation may be compensated by the fact that the higher HRFT samples contain greater amounts of hard martensite within their structure.

4.4.3 Dilatometry

These tests were designed to obtain curves from which the A_1 and the Ms could be measured.

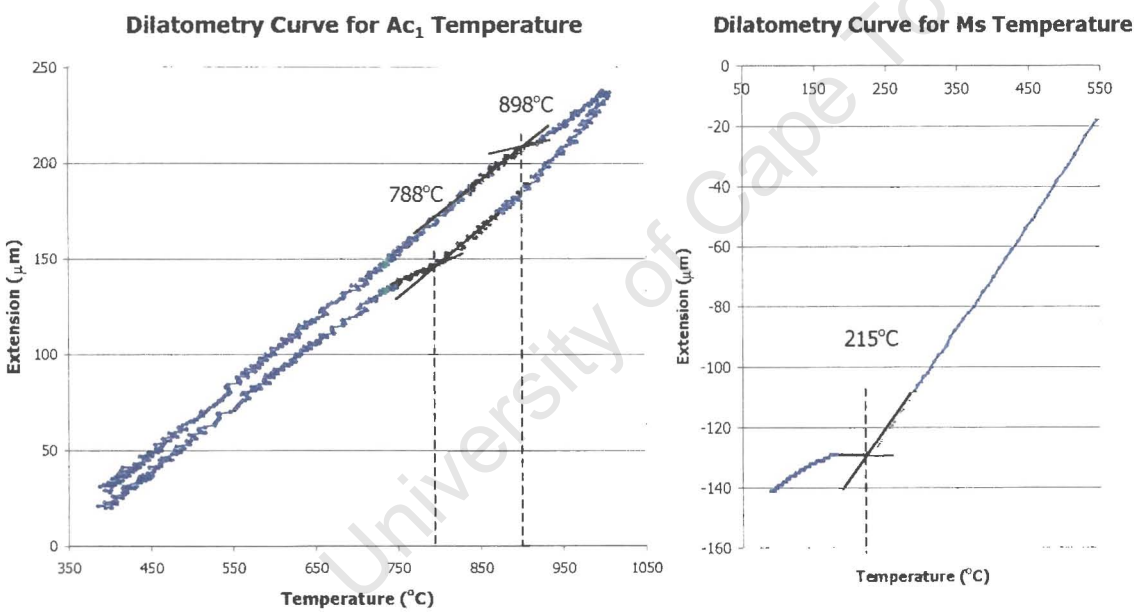

Figure 51. Two dilatometry graphs: a) Heating and cooling curves of the 430 material to obtain the A_1 temperature; b) Cooling curve at the maximum cooling rate showing the Ms.

From the graphs above the A_1 was estimated at 843°C from averaging the measured Ac_1 and Ar_1 temperatures of 898°C and 788°C respectively. The Ms was measured at 215°C.

5 DISCUSSION

5.1 Identifying the Constituents for Ridging

EBSD proved to be a useful tool for analysing the microstructure, when seeking to explain the differences in the ridging profiles between different samples. Its quantitative nature enabled easy objective comparisons to be made. The orientation information that it obtained enabled examination of the microstructure, textures and their spatial distribution, as well as the presence different phases. To gain all this information before the advent of EBSD would have required several different techniques to used, which would have consumed more time. The following discussion details how EBSD was used to identify the constituents that lead to the ridging profiles as well as how they fitted into the models that have been proposed.

5.1.1 Grain size banding

Grain size banding was the first observed heterogeneity in the microstructure of the lower HRFT samples. Grain size banding has been suggested to contribute to the ridging phenomenon by authors such as Sheppard et al.[12], Wittridge[24] and Park et al.[50], and therefore the difference in yield strength between bands was measured in this study. The average grain size of a band of large as well as a band of small grains in a C700s map, which showed the most severe grain size banding, was calculated, Figure 33. The average grain sizes in these bands were 10.9μm and 6.4μm, which corresponded to the yield strengths of 333MPa and 352MPa respectively. These values of yield strengths were calculated using the Hall-Petch relation in which only the grain size is a variable. It does not consider differences of orientation in the material or boundary conditions, thus the values for yield strength obtained are not definitive for those regions. Nevertheless, the values are useful to gauge the effect purely of grain size on the yield strength between bands.

This difference of around 20MPa between bands could be significant in terms of the ridging model, since this would suggest that the large grain size band would start to yield before its adjacent small grain size band. As it yields it will thin in the

transverse/normal plane and will cause stresses in the transverse direction, which is a requirement for the Wittridge and Knutsen model[14,24].

The degree of grain size banding can be described by the difference in average grain sizes in each band. In an attempt to conveniently compare samples, the histograms of grain sizes between the samples were compared, Figure 34. The histogram of the C700s sample, with the greatest observed magnitude of grain size banding, peaked above the other histogram curves for the smaller grain sizes and also it extended to the greatest measured grain size. While the C700s histogram curve stood out amongst the other curves, the other histograms did not as explicitly show the extent of banding even though there was a significant difference between the 700s and 800s samples. This, together with the loss of information about the spatial arrangement of grain sizes, rendered this a poor technique for comparing the degree of grain size banding between samples. Therefore, for this purpose, the best technique is by visually comparing the banding and measuring the average size in the bands.

The small grain size bands were noticed to coincide with regions of high precipitate density using ECC, Figure 35, while the regions of larger grain sizes had a relatively low precipitate density. Therefore, it was concluded that the process governing precipitation distribution is linked with the formation of grain size banding. Some precipitation was likely to occur during cooling, but the majority of the precipitates would have been formed during the annealing of martensite. Areas that were previously austenitic would have had a high affinity for carbon and would have retained the high proportion of carbon while cooling through hot rolling. Therefore, some precipitation was likely to have occurred as a portion of the material transformed from austenite to ferrite, which has a lower carbide solubility, seen in Figure 42. However, most of the precipitation would have occurred after the martensite is annealed and the trapped carbon is released as carbides.

These regions of high precipitation density result in fine recrystallized structures due to three reasons:

- Firstly, at high temperatures the austenite phase is harder than the ferrite since ferrite has 48 slip systems that become activated at high temperature compared to austenite's 12. Therefore, during hot rolling the austenite partitions more

strain energy to its surrounding ferrite, Figure 44, giving it more deformation energy and increasing the driving force for a fine recrystallization. In a similar way, the martensite or areas of high precipitate density partition strain energy to the surrounding ferrite during cold rolling.

- Secondly, the martensite transforms back to a fine ferrite structure during annealing. The two points above are illustrated in the diagram below.

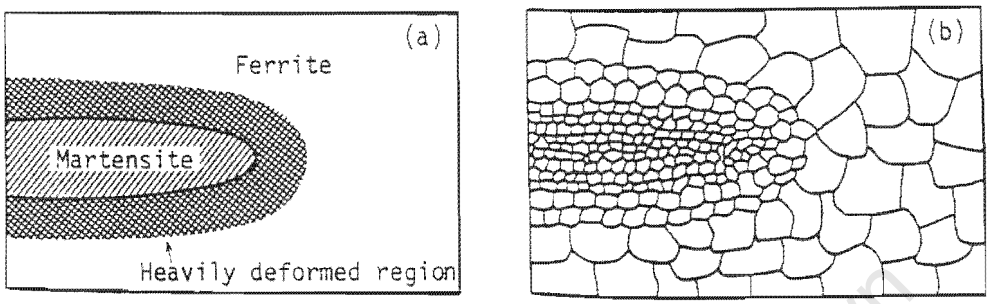

Figure 52. Diagram of microstructural change from a) after cold rolling to b) the annealed state b). The transformations that occur are: martensitic region to a fine ferrite structure plus precipitates, the heavily deformed region to a fine ferrite structure while the surrounding region to a coarse ferrite structure.

- Thirdly, the precipitates will cause grain boundary drag and will inhibit grain growth, thus ensuring the retention of a fine grained structure.

Tsuji et al. showed that the recrystallization kinetics and the resultant recrystallized grain size is strongly dependent on the initial grain orientation[31]. They used the columnar grains of a 19%Cr ferritic stainless steel. Therefore in a similar manner in this material, the difference in grain size in the material may also be dependent, not only on the phases present in the material, but also the orientation of the grains in the cast structure.

Please refer to section 5.2 for discussion on the effect of starting structure on the size and distributions of grain sizes in the cold-rolled annealed material.

5.1.2 Taylor factor banding

Taylor factor (M value) banding was the second heterogeneity found in the EBSD maps of the samples that showed the most severe ridging. Automated EBSD

enabled such spatial distribution of orientations to be observed efficiently, which before would manually be very slow. Previous authors, using the same technique, identified texture clusters and related these to ridging observations[16,17,18,50,51]. In this investigation, however, the distribution of M values was examined as a more direct method of relating heterogeneity in the microstructure to the distribution of plastic properties required in the ridging models.

Again using the C700s sample that showed the most severe ridging, maps of the orientation dependent Taylor factor were plotted, with the prescribed deformation direction chosen as the rolling direction. Bands of grains, extending in the rolling direction, that had similar M values were observed. As in the grain size banding case, these bands were isolated and their average M calculated, Figure 36. The difference in yield stresses, assuming other material properties to be the same, between these bands was around 40MPa.

The bands of high M were examined to find what predominant orientations resulted in them having such M values. These bands were found to consist of grains that were more strongly textured w.r.t. the lower M bands. Both the α-fibre and the η-fibre have rotational symmetry about the rolling direction, therefore each orientation in these fibres would have the same Taylor factor. The grains with orientations close to these two textures had high M values. The γ-fibre has rotational symmetry about the ND and thus the M values for orientations along this fibre texture would vary. The high M bands are produced by bands of material that are strongly textured in a matrix of relatively random orientations.

In summary, the C700s sample mainly consisted of random orientations, with low average M values, interspersed with bands of strong texture, with high average M values. Therefore, the heterogeneity of the M values would suit the requirements of the ridging model, discussed in the next section, with a matrix of random orientation and elongated bands of preferred orientation.

5.1.3 Relating Heterogeneity to the Ridging Mechanism

The Wittridge and Knutsen model[24] will be used to discuss how the bands of different grain size and M values resulted in the ridging severity observed after deformation. This model is a recent one that has been verified using finite element modelling. It also gives a useful description of the stresses involved for the material to obtain the corrugated profile (see section 2.3.4), which is lacking in the most other models. The required structure for ridging to occur before deformation is shown schematically below.

Before deformation

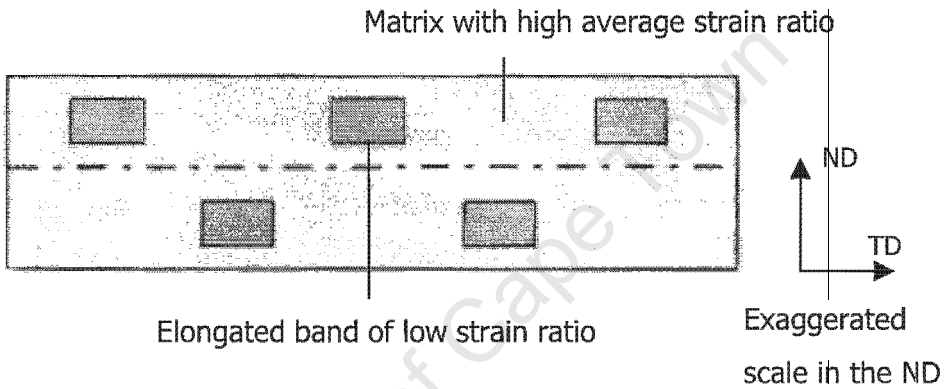

In this model, the difference between the bands and the matrix is in their strain ratios. The bands need to be elongated in the rolling direction and must have an asymmetrical distribution about the centre line. During deformation, such an arrangement will lead to differential transverse strains, resulting in local bending and ultimately causing the ridged profile, seen below.

During deformation

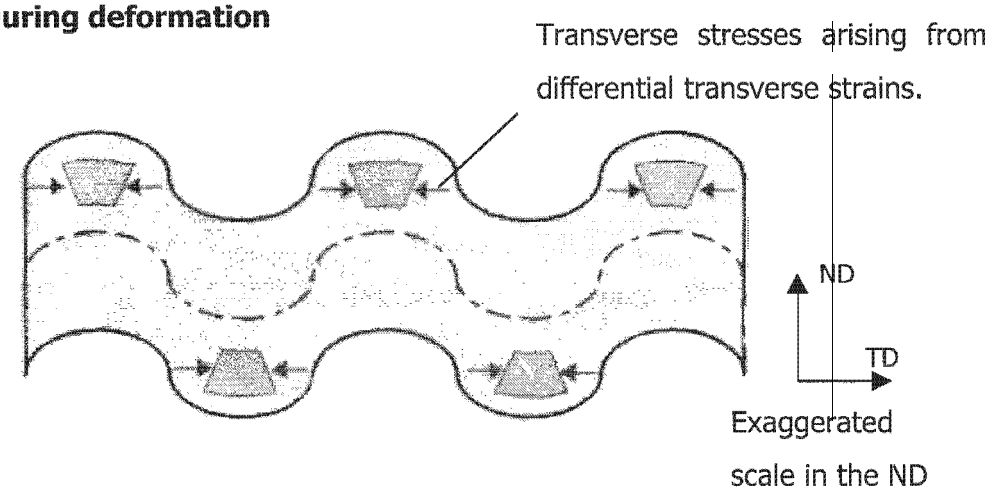

It is the differential transverse strains that the Wittridge and Knutsen model requires to give rise to localised bending. These are satisfied in the model by elongated bands of material differing in strain ratio to the matrix, while the material in this investigation satisfies the requirement with elongated bands differing in flow stress to the matrix. The difference in flow stress between these bands and the matrix is attributed to bands of smaller average grain size or higher Taylor factor than the matrix. These differences will cause preferential thinning in the lower flow stress matrix before the bands leading to differential strains. Transverse stresses will then develop between the matrix and bands, which would enable the strain bending to develop and cause ridging. In this regard, the difference in the M values between bands of high Taylor factor and the matrix were measured at 40 MPa. The difference in Taylor factors most likely has a more profound effect on yield strength heterogeneity than the difference between grain size bands, measured at around 20 MPa. The two effects may interfere constructively to produce a reinforced heterogeneity of yield strengths, as seen in the calculations of Figure 33 and Figure 36, but this is not necessarily the case.

Strain ratios were not calculated in this investigation. However, the literature gives information regarding the relative strain ratios of different orientations. Since the γ-fibre has rotational symmetry about its ND it has a fairly constant high strain ratio[44], the other fibres vary in strain ratios considerably. Other common orientations that have been identified as having above average strain ratios are the {100}<011> orientation in the α-fibre and the Goss texture in the η-fibre. The strain ratios are orientation dependent and therefore can be calculated from the information gained using EBSD. This was not carried out in the present study.

The ODFs of the final annealed 700s material showed that the E700s had a more strongly developed texture than the C700s sample (Figure 39) which showed greater ridging severity. This suggests the ridging severity is dependent not only on the magnitude with which the different bands differ in plastic properties, but also on their distribution in the material. The schematic above describing the Wittridge model has one band of material with low strain ratio per ridging undulation, relating to a single band of small average grain size or high average Taylor factor in this study. The distribution of such bands was however, observed to have a higher frequency in relation to the undulations. The C700s, which showed the lowest

distribution frequency of bands, had several bands of varying grain size and Taylor factors from the surface to the centre of the plane investigated. This suggests that the bending moments that cause the ridging undulations are the cumulative result of a number of bands leading to an overall asymmetrical distribution of properties. Now if the bands are randomly arranged in the material, then the lower their distribution frequency the more asymmetrical will be the result. This is because the greater the frequency of bands in the material, the greater the probability that the bands will align themselves symmetrically about the centre line. If the extreme cases are considered, as the bands are distributed with greater frequency, the more the material will tend towards a homogeneous distribution. The lower the frequency of distribution, however, the closer the material will approximate the model where each band will result in an undulation (see Figure 53).

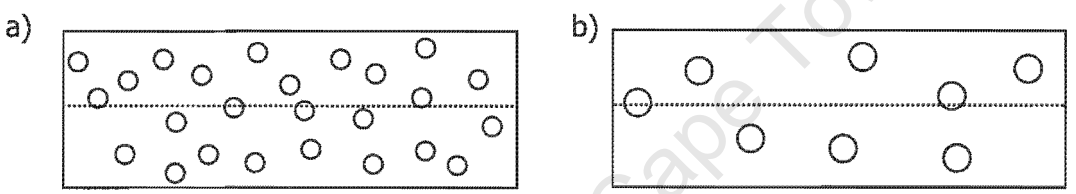

Figure 53. Effect of the distribution of heterogeneous bands in material, a) higher frequency distribution where many bands nullify each other across the midline, b) lower frequency and more asymmetric distribution of plastic properties.

The lower the frequency and the more asymmetrical the distribution of plastic properties is, the greater will be the resulting bending forces and ultimately the greater the amplitude of ridging. Furthermore, as the distribution frequency decreases, the greater the distance between bands, which will result in a greater wavelength of undulations.

5.1.4 Explanation of Observed Ridging Topography

When comparing the Euler colour maps and the Taylor maps for the 700s and 800s samples the following observations can be made. Firstly, the maps of the 800s samples were far more homogeneous in terms of their grain size and the M distributions. Whereas the 700s samples had clear observable bands of similar grain size as well as M values, the 800s samples had bands that were less ordered and

less distinguishable. Secondly, the columnar samples in both the 700 and 800 HRFT had average grain size and M values that were distributed with a lower frequency across the transverse plane than their equiaxed counterparts.

The predominant roughening effect in the 700s specimens was identified as the 'ridging' effect whereas that for the 800s samples was the 'roping' effect. A distinction between the two was made over their wavelength, amplitude and length of the undulations in the rolling direction. Now, with more ordered heterogeneous bands, the 700s samples have a greater difference in average yield strengths between bands. This led to higher differential transverse strains in the tensile specimens, and resulted in profiles with higher amplitude undulations than those of the 800s specimens. The bands in the 800s samples could conceivably be shorter than those in the 700s samples. Although the specimens were not mapped over the length of a single roping 'undulation' (≈ 2-4 mm), the bands seem more fragmented than the bands of the 700s samples. With a higher frequency distribution of bands through the material (Figure 53), and with their shorter continuity in the rolling direction, the 800s samples would result in a high frequency surface roughening effect after deformation. Therefore, the distinction between the surface roughening effects in the 700s and 800s samples are not due to different underlying mechanisms. Rather they are due to the vastly different degree to which the material displayed heterogeneous plasticity banding.

The 'warping' that was distinguished as the longer wavelength surface roughening effect may be produced by the same Wittridge mechanism but with the asymmetry acting over a larger scale. In the random distribution of heterogeneous bands there may be several frequencies at which an asymmetrical distribution of these bands will occur. The observed frequencies of ridging will be the same as the frequencies of bands that lead to the greatest asymmetrical distribution of differential strains. Thus ridging profiles may be superimposed on one another as has been noted by other researchers[15,16,17].

The difference between the ridging profiles of the columnar and equiaxed samples is also connected to the spatial distribution of bands. A lower distribution frequency of bands, as explained in the previous section, would lead to a ridging profile that is

more severe as well as having a lower frequency of waves. This was observed on the ridging profiles.

5.2 Effect of Starting Structure

The constituents of the ridging phenomenon have been identified, with reasonable confidence, to be the heterogeneous distribution of yield strength in the microstructure on a scale greater than the grain size. These are attributed to textural variations and to a lesser extent grain size banding. This enabled the samples that differ in ridging topography to be compared on a microstructural level, which aids the understanding of how different TMP parameters affect surface quality.

By comparing the EBSD maps of the equiaxed verses the columnar samples in the lower two HRFT, the difference in observed ridging severity can be explained. Firstly, the difference in average grain size between grain size bands is far larger in the C700s specimen than the E700s, (Appendix 2.a & 2.b). The same comparison in the 800s specimens is more difficult since the bands are less defined, nevertheless the banding in the C800s specimens is more developed than the E800s specimen. The spacing between the grain size bands is more irregular in the C700s specimen compared to the E700s specimen.

Secondly, the Taylor maps reveal the striking difference of Taylor band spacing between the two starting structures, Appendix 3. In the 700 samples this is more evident where there is four distinguishable bands of high average M value spanning the normal/rolling plane from surface to centre of the E700s specimen, compared to two in the C700s specimen. Again it is difficult to compare the 800 samples, but the C800s does show more clearly defined bands (left side of map) than the E800s sample.

To explain the observed differences in the final annealed material, that led to differences in ridging severity between the two starting structures, the hot rolled material is examined. There is one main difference between the starting structures in the hot rolled material, namely the difference in prior austenite distribution. The prior austenite distribution is very irregular across the columnar samples compared

to the equiaxed ones. It is difficult to capture this variation in a micrograph, but the light micrographs in Figure 45 (a) and Figure 48 (b), together with the ECC images in Figure 42, highlight this characteristic. In the columnar specimens, broad (around 200 μm thick) elongated bands of material with a high density of martensite stringers, were observed. Such bands of martensite stringers were separated by broader sections ferrite, relatively sparsely interspersed with islands of martensite. The equiaxed samples did not show variation in prior austenite distribution on such a large scale, but the distribution was rather more uniform with a higher frequency.

This large scale variation must originate at the starting structures and has its origin in the difference between the starting grain size of the two structures. As the material was heated for a homogenisation treatment at 1100°C it would pass into the dual phase region where austenite would nucleate and grow. The most probable site for this reaction to occur in the undeformed material would be at the grain boundaries. The columnar structure with larger grain size and few grain boundaries would thus have fewer sites for the austenite to nucleate and grow from. It would thus be reasonable to assume that the austenite would be more evenly distributed in the equiaxed cast structure, at the homogenisation temperature, than in the columnar structure. As it is then subsequently rolled and elongated, there would be a more uniform mean free path between the austenite stringers in the equiaxed material compared to the columnar sample. The diagram below illustrates how the large columnar grain size would result in a more uneven distribution of austenite during hot rolling.

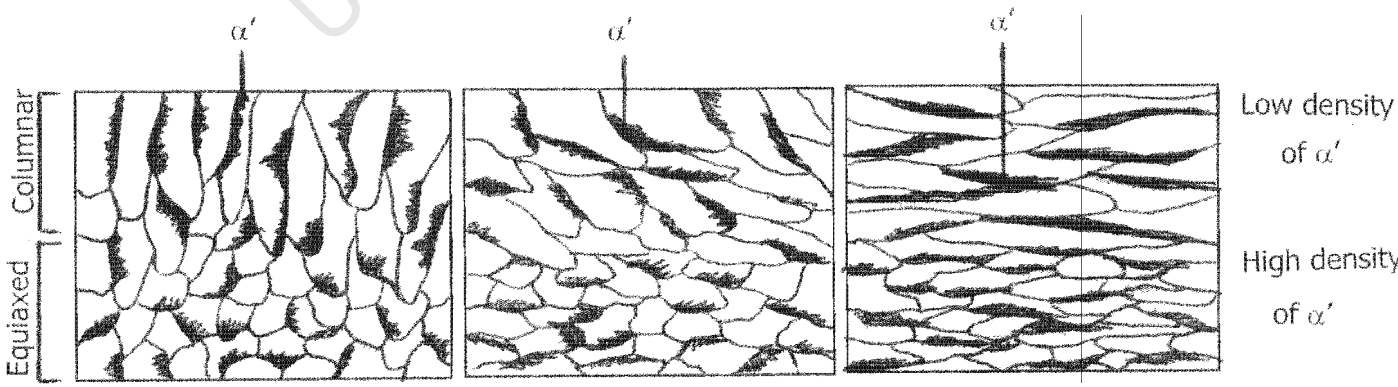

Figure 54. Series of diagrams illustrating the distribution of martensite as the material is hot rolled.

The austenite affects the composition of the material since it has a higher affinity for carbon than ferrite and thus causes partitioning of elements, which in turn causes precipitate banding. The austenite will partition strain energy to the surrounding ferrite during hot rolling and, if it transforms to martensite on cooling, it will partition strain energy during cold rolling. The recrystallization kinetics through the material will therefore also be affected as detailed in section 5.1.1. As the driving force for recrystallization is increased, the more refined the structure and more random its orientations will be after annealing[35,39]. Thus, all these events will contribute towards the development of bands of similar Taylor factors and grain sizes to a greater or lesser extent (see section 5.1.2).

Now with uniform spacing of the austenite, as the equiaxed samples approximate, the more uniform the grain refining effects will be. Therefore, the equiaxed samples would tend to be more regular in grain size banding, with a smaller difference in average grain size between large and small grain size bands. The original columnar grains remain larger than the equiaxed ones while recrystallization is taking place during hot rolling, compared in Figure 40. The larger grain size in the cold rolled structure as well as the larger spacing between prior austenite bands gives the columnar samples a lower distribution frequency of Taylor banding than the equiaxed samples, leading to more severe ridging.

5.3 Effect of HRFT

The HRFT parameter had a more profound effect on the ridging severity than the difference in the starting structure. This has been explained in terms of their microstructures in section 5.1.4. All the changes in the microstructures of the hot rolled samples were examined to discover how they differentiated.

Repeated recrystallization after rolling passes during the hot rolling procedure, which requires thermal energy to be activated, was considered as a possible cause of the randomisation of the heterogeneous bands observed in the higher HRFT samples. With lower HRFT there is less thermal energy for dislocations to glide and cross slip, which is necessary for recovery to take place. Thus after each pass, the lower HRFT samples recovered less and contained more stored strain energy. These samples

also contained a greater driving force for recrystallization. When the material was reheated in the furnace after each rolling pass, it was given an opportunity to recrystallize. During this time in the furnace the lower HRFT samples, even though the reheating temperature was lower, experienced more recrystallization events than the higher HRFT samples. This was deduced from the microstructure comparison of the 800s and 900s specimens in section 4.3.1. Therefore the breakdown of heterogeneous bands in the final microstructures of the 800s samples is not due to repeated recrystallization events in the hot rolled structures. In the case of the higher HRFT's, the temperature during the rolling cycle may have been sufficiently high to induce grain growth. If grain growth occured, grains with a favourable orientation and size would have grown preferentially into others resulting in a lower number of grains and a stronger grain growth texture present. This further suggests that in terms of microstructure evolution (neglecting phase changes), increasing the HRFT will not favourably randomise the orientations present.

The other thermally dependent variable considered was the phase change between ferrite and austenite in the hot rolling schedule. All the material would have the same amount of austenite present in their structure after the homogenisation treatment at 1100°C. As the temperature of hot rolling differs between the hot rolling schedules, the equilibrium proportion of austenite present between the samples would differ, according to the phase diagram. The A_1 was measured at 843°C using dilatometry, and a Ar_1 of 780°C where the cooling rate was 2°C/min. The reaction requires activation energy as well as time for diffusion, therefore during the rolling (with a higher average rate of cooling) the Ar_1 would probably have been suppressed somewhat to a lower temperature, perhaps around 700-750°C. This would suggest that the 700s samples would have very little, if any, austenite present in their structure after their last pass through the hot rolling mill.

The prior austenite would have partitioned strain energy to the ferrite during hot rolling, although this would not have been as effective at randomising the structure as the role the martensite played during cold rolling. The much harder martensite phase would partition strain energy to its surrounding ferrite during cold rolling where all the strain energy is kept within the structure for recrystallization during the final anneal. This has been found to be a very effective way of randomising the structure and destroying texture colonies[12,33,34,35,36]. The higher the martensite

percentage the greater will be the partition of strain energy to the ferrite, which will produce a finer recrystallization grain size. This material produces an amount of austenite that is well below 50% even at the maximum percentage within the γ-loop. Nevertheless, the small amount of martensite produced has a major effect on the structure during cold rolling. It will resist deformation and will affect a large volume of ferrite, which even in the deformed state will be softer than the martensite, as it flows around the martensite.

The martensite contents of the different HRFT samples were compared in the light micrographs and a trend towards higher martensite percentages as the HRFT increased was observed, section 4.3.3. The largest difference in martensite contents between successive temperatures was between the 700s and 800s samples where the 700s samples had very little martensite contents. This coincides with the greatest difference in ridging severity that was observed to be between the 700s and 800s samples. The hardness measurements after the hot rolled stage also give evidence of a greater martensite percentage as the HRFT increased, section 4.4.2. The lower HRFT samples were expected to have a far greater hardness due to their greater stored strain energy. This is not the case with the average hardness in the 700 samples being 221 HV (30kgf) compared to 212 HV (30kgf) in the 800 samples. The increased martensite contents in the higher HRFT samples may compensate for the expected lower residual strain energy. Secondly, the increased standard deviation in hardness as the HRFT increases indicates that there is a greater variation in hardness across the material and this is probably due to islands of martensite in the structure.

The only exception to the trend observed above, was the E800s sample that had little martensite present in its hot rolled structure, seen in the light micrographs and the ECC images. In this sample though, the precipitates were very noticeable after etching or electropolishing indicating that they were larger than those in the 700 samples. This is reasonable since in the higher hot rolling temperatures the carbon was more mobile and once the austenite transformed to ferrite in the E800s sample, the carbon would have been able to form larger precipitates. Hölscher has shown that the precipitate size plays an important role during cold rolling in how it randomises the texture after final annealing[38]. A band with a high density of precipitates would thus act in the same manner as a stringer of martensite in

partitioning strain energy to material surrounding it, which would recrystallize to form less strongly textured material.

In summary, the range in HRFT gives rise to variations in recrystallization behaviour and austenite content during the hot rolling process, and variations in the martensite content during cold rolling. All these parameters influence the final grain size distribution as outlined in the preceding paragraphs. Furthermore, grain growth must also be considered to be prominent at the higher HRFT's.

6 CONCLUSION

6.1 Identifying Ridging Constituents

EBSD was used successfully to identify two microstructural variations that lead to a heterogeneous distribution of yield properties through the material. These were the banding of grains with similar grain size and the banding of similar orientation dependent Taylor factors.

The calculated difference in yield strength between extreme grain size bands was approximately 20 MPa, while between Taylor factor bands the difference in yield strengths was calculated at approximately 40 MPa. This suggests that the variation in Taylor factors through the material has a more profound effect on the variations of yield properties than the differences in grain size. A band of high Taylor factors is typically one that has a strong texture component, either α-fibre or η-fibre, while a region of low Taylor factors had a more random spread of orientations.

A lower distribution frequency of heterogeneous bands and a large variation of yield strengths between the bands and their surrounding matrix will lead to severe ridging. This was supported by observation and explained with the ridging mechanism. The equiaxed cast structure samples had smaller variations in grain size and a higher frequency distribution of Taylor factor clusters, and consequently a lower ridging severity than their corresponding columnar samples.

6.2 Effect of TMP parameters

The HRFT had the most profound effect on the ridging severity of the different TMP parameters investigated. The severity decreased consistently with increasing HRFT. This large difference in severity is due to the quantity of martensite present before cold rolling. With a larger amount of martensite in the structure, the more strain energy is partitioned to the softer ferrite during cold rolling. This leads to a more random orientation distribution after recrystallization, particularly as a result of the

particle stimulated nucleation effect that has been well reported. The martensite content can be controlled by thermally positioning the material in the dual phase γ-loop.

The equiaxed samples consistently had better surface quality than the columnar samples. This improvement in surface quality between the starting structures was not as pronounced as that between HRFTs. The equiaxed samples, with a finer starting structure, produced a higher frequency distribution of austenite in the homogenised material. After hot rolling, the equiaxed samples had a shorter mean free path between martensite stringers and this produced a final structure with a higher frequency distribution of heterogeneous bands.

The different cooling methods of slow cool (s) verses short quench and slow cool (q) had no effect on the ridging severity of the final material.

REFERENCES

[1] *Steel. A Handbook for Materials Research and Engineering*, Volume 2. Applications, Verein Deutscher Eisenhuttenleutte (Ed.),Springer-Verlag, Germany (1993).

[2] R. Castro, *Stainless Steels*, P. Lacombe *et al* (Ed.), Les Editions de Physique Les Ulis, France (1993).

[3] F.B. Pickering, *The Mettalurgical Evolution of Stainless Steels*, American Society for Metals and The Metals Society, U.S.A. (1979).

[4] D. Peckner and I. Bernstein, *Handbook of Stainless Steels*, McGraw-Hill, U.S.A (1977).

[5] Source book on Stainless Steels, American Society for Metals, USA (1976).

[6] http://minerals.usgs.gov/minerals/pubs/metal_prices/., last visited 2000-11-08.

[7] D. R. Askeland, *The Science and Engineering of Materials – 3rd Ed.,* PWS Publishing Company, Boston (1994).

[8] F.J. Humphreys *et al.*, *Recrystallization and Related Annealing Phenomena, Pergamon*, Oxford (1996).

[9] N. Machio, MSc Dissertation, Influence of Composition and Thermomechanical Processing on Microstructure Evolution in AISI 430 Steel, University of Cape Town, 1998.

[10] J.D. Defelippi *et al.*, Metallurgical Transactions, **2**, 3209 (1971).

[11] R.N. Wright, Anisotropic Plastic Flow in Ferritic Stainless Steels and the 'Roping' Phenomenon, Metallurgical Transactions, **3**, 83 (1972).

[12] T. Sheppard and P. Richards, Roping Phenomena in Ferritic Stainless Steels, Materials Science and Technology, **2**, 693 (1986).

[13] R. N. Wright, The Direction of Tensile Strain and The "Roping" Phenomenon in Ferritic Stainless Steels, Metallurgical Transactions, **7A**, 1385-1388 (1976).

[14] N. Wittridge, PhD thesis, University of Cape Town, (1998).

[15] M. Hamasaki, I. Gokyu and S. Okamura, Ridging in 18% Chromium Stainless Steel, Trans. J. I. M., **13**, 238-247 (1972).

[16] K. Sztwiertnia *et al.*, Topological Aspects of Ridging Phenomenon in Ferritic Stainless Steel, Proc. of the 12th Int. Conf. On Textures of Materials, 647-652 (1999).

[17] K. Bethke, M. Hölscher and K. Lücke, Local Orientation Investaigation on the Ridging Phenomenon in Fe 17% Cr Steel, Materials Science Forum, **157-162**, 1137-1144 (1994).

[18] J. Harase *et al.*, Grain Orientation Distribution in a hot rolled 17% Cr Ferritic Stainless Steel, Materials Forum, **14**, 296-303 (1990).

[19] C. M.Vlad, Optimization of Texture of X8cr17 Steel Sheet by Means of ODF Analysis, 8th Int. Conf. on Textures of Materials, The Metallurgical Society, 873 (1988).

[20] H. Chao, The Mechanism of Ridging in Ferritic Stainless Steels, Transactions of the American Society of Metals, **60**, 37 (1967).

[21] H. Takechi *et al.*, The Mechanism of Ridging Formation in 17% Cr Stainless Steels Sheets, Trans.J.I.M, **8**, 233 (1967).

[22] M. Hölscher *et al.*, Steel Research, **12**, 62 (1991).

[23] J.A. Salsgiver *et al.*, The Importance of Fibre Textures and Their Distribution in the Phenomenon of Roping in Ferritic Stainless Steels, Recrystallization '90, The Minerals, Metals and Materials Society, 849-854 (1990).

[24] N.J. Wittridge and R.D. Knutsen, Characterization of Microstructure and Texture Evolution in AISI 430 Ferritic Stainless Steel – Analysis of the Surface Ridging Phenomenon, Thermomechanical Processing in Theory, Modelling & Practice, 390-397 (1997).

[25] K. Kawahara, Effect of Rolling Directions on the Ridging Phenomena in 17 Cr Ferritic Stainless Steels, Trans. of National Research Institute for Metals, **16** no.6, 227-233 (1974).

[26] D. Raabe *et al.*, Textures of Strip Cast 16%Cr, Scripta Metallurgica, **29**, 113 (1993).

[27] D. Raabe *et al.*, Texture Development of Strip Cast Ferritic Stainless Steel, Materials Science Forum, **157-162**, 1039 (1994).

[28] M Ueda, Development of Stainless Steel by Progress of Solidification Process, La Metallurgia Italiana, **87**, n1, 19 (1995).

[29] T. Omori *et al.*, Texture of AISI 430 Steels Rolled by Planetary Mill, Proc. of Int. Conf. On Stainless Steels, ISIJ, 872 (1991).

[30] Y. Hayakawa *et al.*, Initial Orientation Dependence of Texture Evolution in Ferritic Stainless Steels, Proc of the 12th Int. Conf. on Textures of Materials, 1095 (1999).

[31] N Tsuji *et al.*, Effect of Initial Orientation on the Recrystallization Behaviour of Solidified Columnar Crystals in a 19% Cr Ferritic stainless Steel, ISIJ Int., **33**, No. 7, 783 (1993).

[32] Y. Itoh *et al.*, Refining of Solidificatioon of Continuously Cast Type 430 Stainless Steel Slabs by Electromagnetic Stirring, Transactions ISIJ, **22**, 223 (1982).

[33] H. Miyaji and S. Watanabe, Effect of the Distribution of Martensite Phase in a Hot-Rolled Sheet on the Ridging Phenomenon in 17Cr Stainless Steel, Trans of Nat. Research Inst. for Metals, **20**, No. 5, 281 (1978).

[34] J. Harase *et al.*, Metallurgy for the Production of 17% Cr Ferritic Stainless Steel Sheet without Hot Band Annealing, Proc. of Int. Conf. on Stainless Steels, ISIJ, 856 (1991).

[35] M. Koike *et al.*, Development of In-line γ Treatment Process for Elimination of Ridging in AISI 430 Ferritic Stainless Steel Sheets, Proc. of Int. Conf. on Stainless Steels, ISIJ, 864 (1991).

[36]G. Abbruzzese *et al.*, Relationships Between Microstructure, Texture Inhonogeneities and Drawing Properties of 17 Cr Steels: Effect of Intracritical Annealing, Innovation Stainless Steel, Florence, 2.345 (1993).

[37] M. Hamasaki et al., Ridging in 18% Chromium Stainless Steel, Transactions of the Japanese Institute of Metals, **13**, 238-247 (1972).

[38] M. Hölscher and L. Staubwasser, Influence of Hotband Annealing on Texture and Formability of Cold Rolled X6CR17 Ferritic Stainless Steel, Innovation Stainless Steel, Florence, 2.339 (1993).

[39] Y.D. Lee *et al.*, Recrystallization Behaviours of Low Carbon Ferritic Stainless Steels During Hot Rolling and Annealing Process, Recrystallization 1990, The Minerals, Metals and Materials Society, 435-440 (1990).

[40] M. Militzer et al., Modelling the Effect of Pinning Forces on Recrystallization and Grain Growth, Proc. of Symposium: Advances in Hot Deformation Textures and Microstructures, The Minerals, Metals and Materials Society, Pittsburgh, 157-168 (1994).

[41] A.J.DeArdo, Influence of Niobium and Tantalum on Stainless Steels, Proc. of the Int. Symposium on Tantalum and Niobium: Mining, Applications, and New Developments, Brussels, 435-462 (1998).

[42] H. Fujimura and S. Tsuge, Effect of C, Ti, Nb on Recrystallization Behaviour after Hot Deformation in 16% Cr Ferritic Stainless Steel, The 4th Int. Conf. on Recrystallization and Related Phenomena, The Japan Institute of Metals, 763-768 (1999).

[43] U. Kocks, C. Tomé and H. Wenk, *Texture and Anisotropy*, Cambridge University Press, Cambridge (1998).

[44] M. Hölscher, D. Raabe and K. Lücke, Rolling and Recrystallization Textures of BCC Steels, Steel Research, **62**-12, 567-575 (1991).

[45] T. Shindo and T. Furukawa, Colony Structure and its Texture in a Ferritic Stainless Steel, Sixth Int. Conf. on Textures of Materials, I.S.I.J, **2**, 846-855 (1981).

[46] H. Kim and J. Szpunar, Ridging Phenomena in Textured Ferritic Stainless Steel Sheets, Materials Science Forum, **157-162**, 753-760 (1994).

[47] W. Hosford, *The Mechanics of Crystals and Textured Polycrystals*, Oxford University Press, New York (1993).

[48] Columbus Stainless, Research and Development, Middelburg, South Africa (2000).

[49] N.J. Wittridge and R.D. Knutsen, Recovery and Recrystallization Characterization in Ferritic Stainless Steel by Using Electron Channelling Contrast, Materials Characterization, **37**, 31-37 (1996).

[50] S. Park, K. Kim, Y.D. Lee and C. Park, Initial Orientation Dependence of Texture Evolution in Ferritic Stainless Steels, Proc. of 12th Int. Conf. on Textures of Materials, 1095-1100 (1999).

[51] M. Brochu, T. Yokota, S. Satoh, Analysis of Grain Colonies in Type 430 Feritic Stainless Steels by Electron Back Scattering Diffraction, Iron and Steel Inst. of Japan International, **37**-9, 872-877(1997).

APPENDICES

Appendix 1 – Hot Rolling

1.a. Enter and exit temperatures of material during rolling

The table below contains the measurements of temperature of each sample immediately before and after it is hot rolled. The equiaxed samples were rolled with 9 passes and the columnar samples, since they were thinner, were rolled with 8 passes. For a prescribed HRFT, each of its four samples was rolled one after the other for the same pass, before progressing to the next pass in the schedule. Thus, the columnar samples were included in the schedule only on the second pass. No data was obtained for the C800q sample since it was rolled as a test before the rest of the samples. The HRFTs are tabled in chronological order.

Furnace Temp.	Sample	Temperature on entering mill (°C)									Temperature on exiting mill (°C)								
	Pass #	1	2	3	4	5	6	7	8	9	1	2	3	4	5	6	7	8	9
1100°C	E900q	970	-	-	930	-	900	930	930	940	950	920	-	915	840	860	890	870	860
	C900q	/	-	-	-	900	910	910	930	950	/	-	-	910	880	890	890	880	860
	E900s	960	950	930	930	900	960	940	930	930	940	920	915	915	890	940	900	880	850
	C900s	/	-	960	910	900	-	890	915	920	/	920	930	900	860	900	880	890	880
1000°C	E800q	950	910	890	-	860	830	830	820	800	910	900	970	-	850	810	800	770	770
	C800q	/									/								
	E800s	-	-	-	-	870	830	850	790	830	930	-	870	-	840	810	810	-	780
	C800s	/	-	890	860	-	-	-	800	840	/	930	870	850	850	810	810	770	780
900°C	E700q	880	830	-	770	750	740	760	750	-	860	820	780	760	740	730	720	730	720
	C700q	/	850	-	-	-	750	730	710	-	/	830	800	780	760	740	725	720	690
	E700s	820	-	-	-	740	730	750	730	730	810	780	760	750	730	720	740	720	680
	C700s	/	-	-	760	740	720	750	710	700	/	820	780	750	730	715	740	700	690
1200°C	E1000q	-	-	100	-	980	1030	1030	1060	1000	1040	970	990	1030	970	980	980	1000	920
	C1000q	/	1060	990	1040	1030	1050	1030	1060	1040	/	950	960	1020	1000	1030	990	980	940
	E1000s	-	1040	1020	-	990	990	-	1050	-	1030	1020	980	-	970	-	1030	990	990
	C1000s	/	1090	1040	1030	-	960	110	1030	1090	/	1060	1000	-	960	910	950	960	1000

1.b. Gauges and reductions of samples

Reductions of each specimen during Hot and Cold Rolling

Starting thickness: Equiaxed = 42.5mm Columnar = 30.5mm

Specimen	Hot Rolled Gauges				*AVE*	%HR Reduction	Cold Rolled Gauges			*AVE*	%CR Reduction
E1000q	3.04	3.03	3.04	3.06	*3.04*	**92.8**	0.9	0.91	0.9	*0.90*	**70.3**
E1000s	2.89	2.88	2.88	2.91	*2.89*	**93.2**	0.87	0.88	0.87	*0.87*	**69.8**
C1000q	2.98	3.05	3.09	3.04	*3.04*	**90.0**	0.91	0.92	0.9	*0.91*	**70.1**
C1000s	3.09	3.06	3.05	3.04	*3.06*	**90.0**	0.92	0.94	0.91	*0.92*	**69.8**
E900q	3.71	3.74	3.68	3.72	*3.71*	**91.3**	1.1	1.11	1.09	*1.10*	**70.4**
E900s	3.76	3.64	3.68	3.77	*3.71*	**91.3**	1.1	1.11	1.1	*1.10*	**70.3**
C900q	3.53	3.56	3.55	3.59	*3.56*	**88.3**	1.1	1.07	1.07	*1.08*	**69.6**
C900s	3.66	3.67	3.79	3.75	*3.72*	**87.8**	1.13	1.14	1.15	*1.14*	**69.3**
E800q	3.82	3.85	3.9	3.94	*3.88*	**90.9**	1.13	1.13	1.17	*1.14*	**70.5**
E800s	4.12	3.97	3.95	4.03	*4.02*	**90.5**	1.13	1.14	1.13	*1.13*	**71.8**
C800q	4.04	4.11	4.06	4.05	*4.07*	**86.7**	1.22	1.23	1.24	*1.23*	**69.7**
C800s	3.92	3.88	3.79	3.87	*3.87*	**87.3**	1.12	1.13	1.13	*1.13*	**70.8**
E700q	4.3	4.21	4.33	4.37	*4.30*	**89.9**	1.29	1.29	1.3	*1.29*	**69.9**
E700s	4.26	4.15	4.32	4.2	*4.23*	**90.0**	1.24	1.23	1.24	*1.24*	**70.8**
C700q	4.45	4.52	4.43	4.37	*4.44*	**85.4**	1.32	1.34	1.33	*1.33*	**70.1**
C700s	4.5	4.37	4.34	4.84	*4.51*	**85.2**	1.36	1.37	1.38	*1.37*	**69.6**
					MAX	93.2				MAX	71.8
					MIN	85.2				MIN	69.3

Appendix 2 – EBSD Grain Size Maps

2.a. E700s

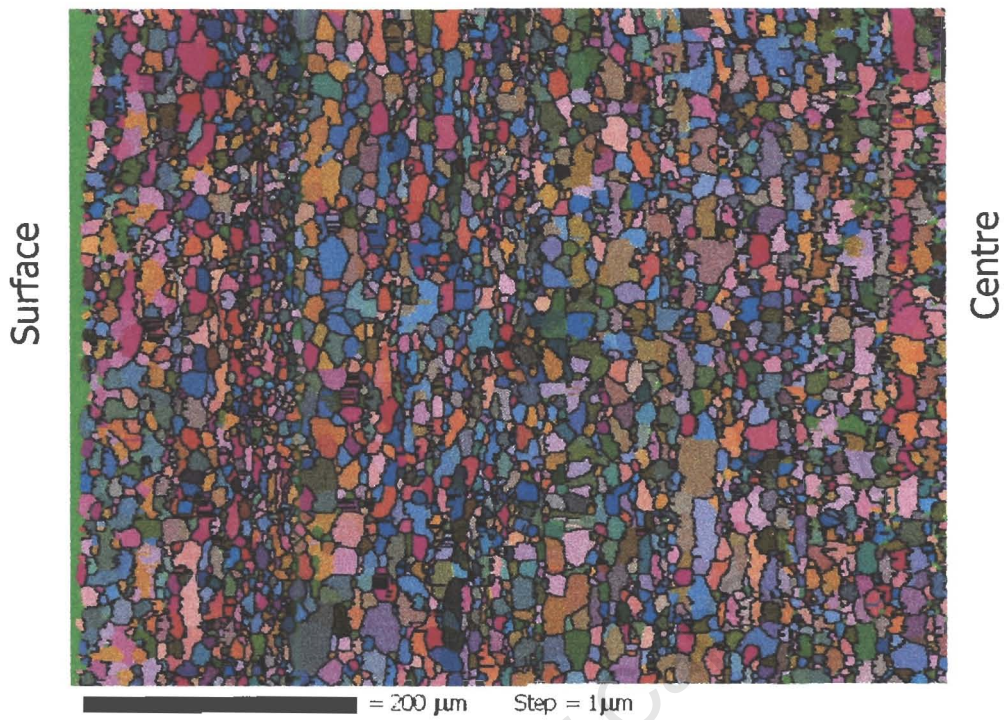

2.b. C700s

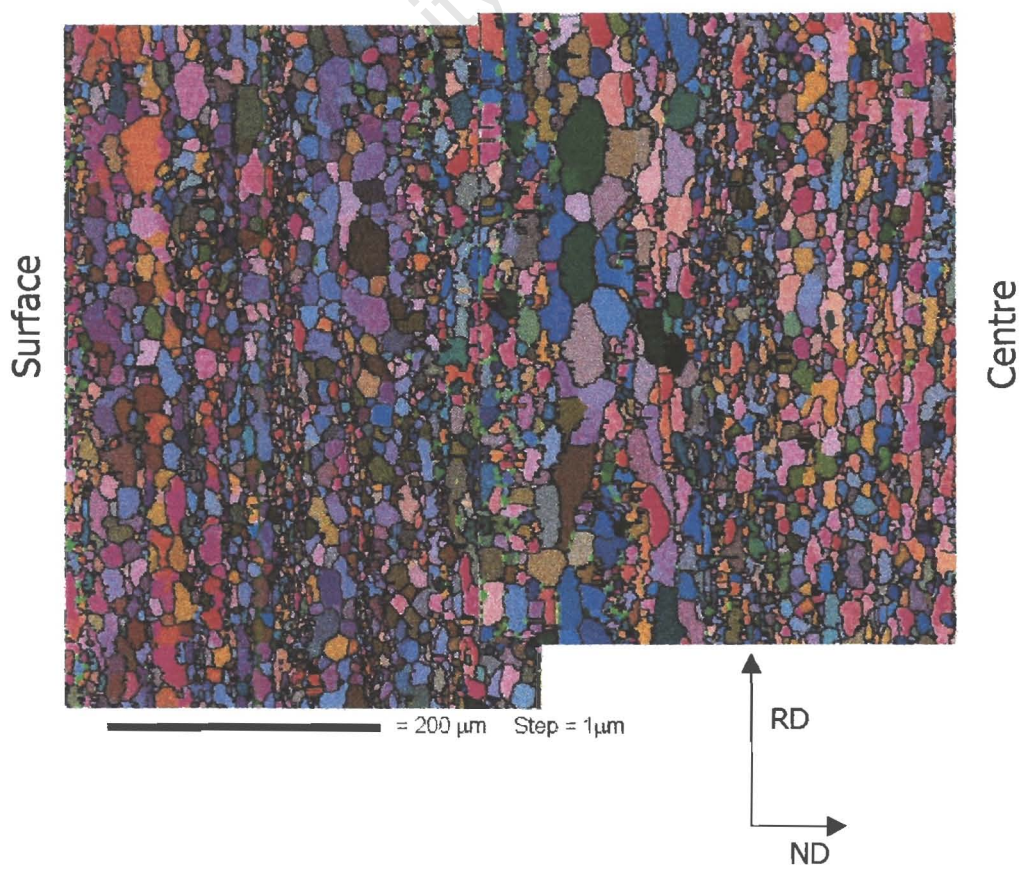

2.c. E800s

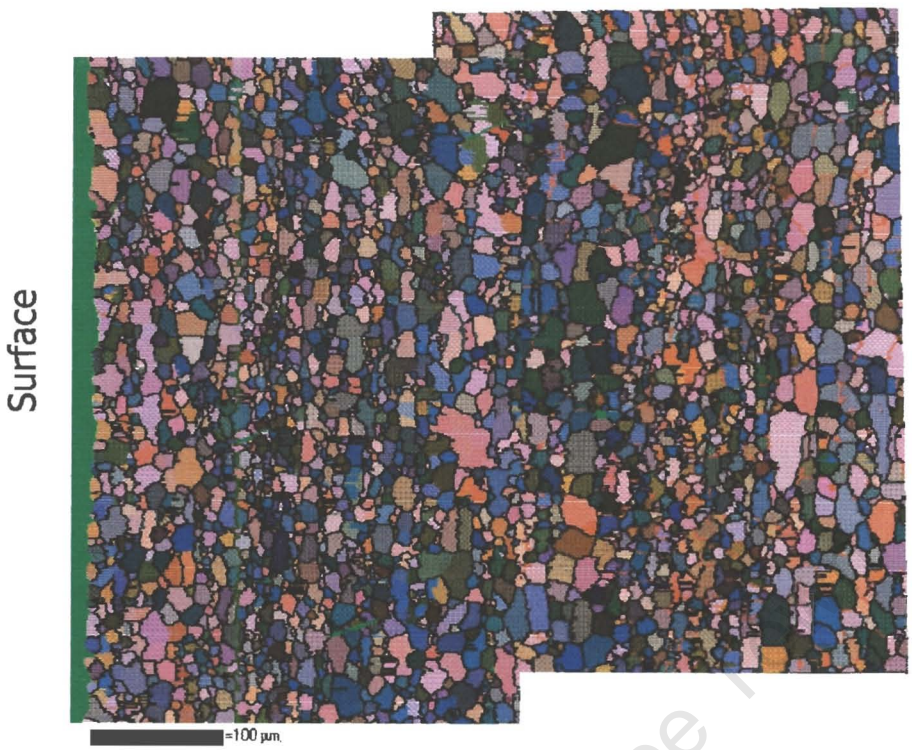

2.d. C800s

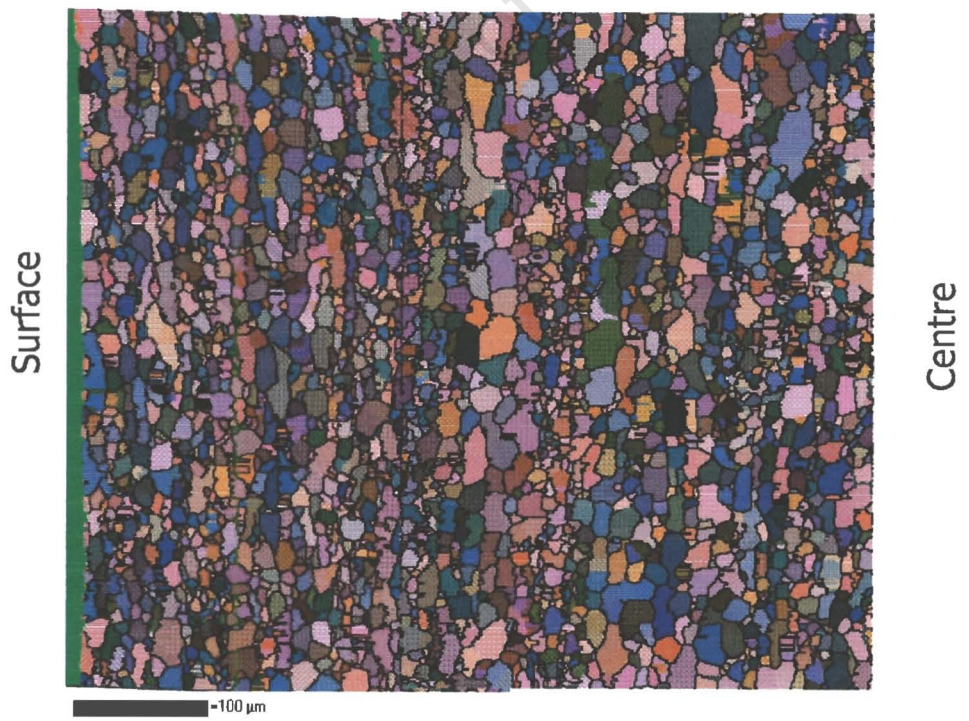

Appendix 3 – EBSD Taylor Factor Maps

3.a. E700s

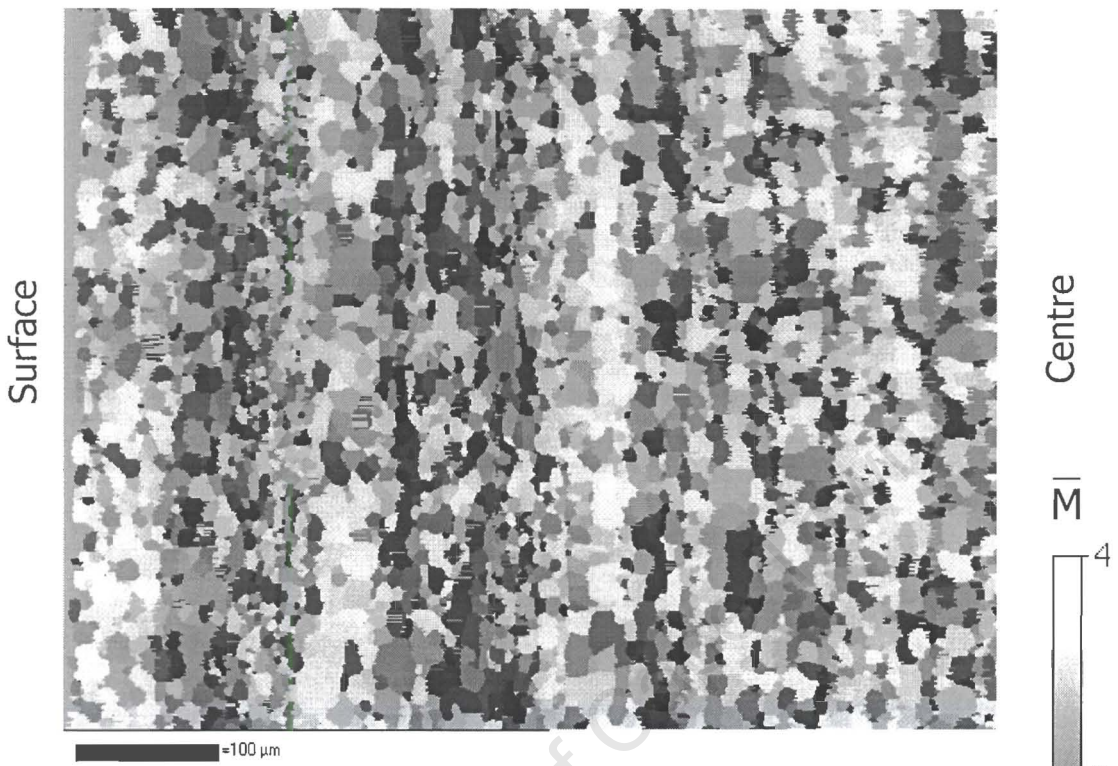

3.b. C700s

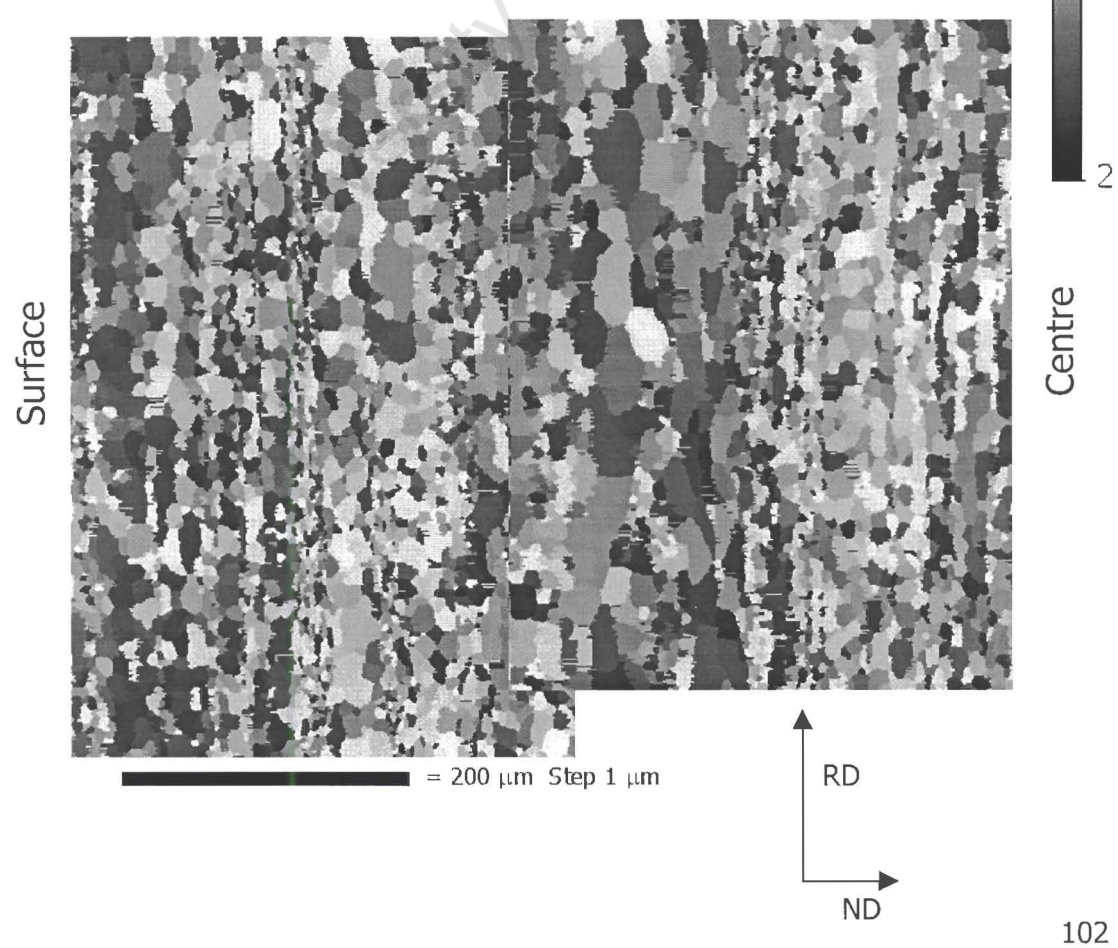

3.c. E800s

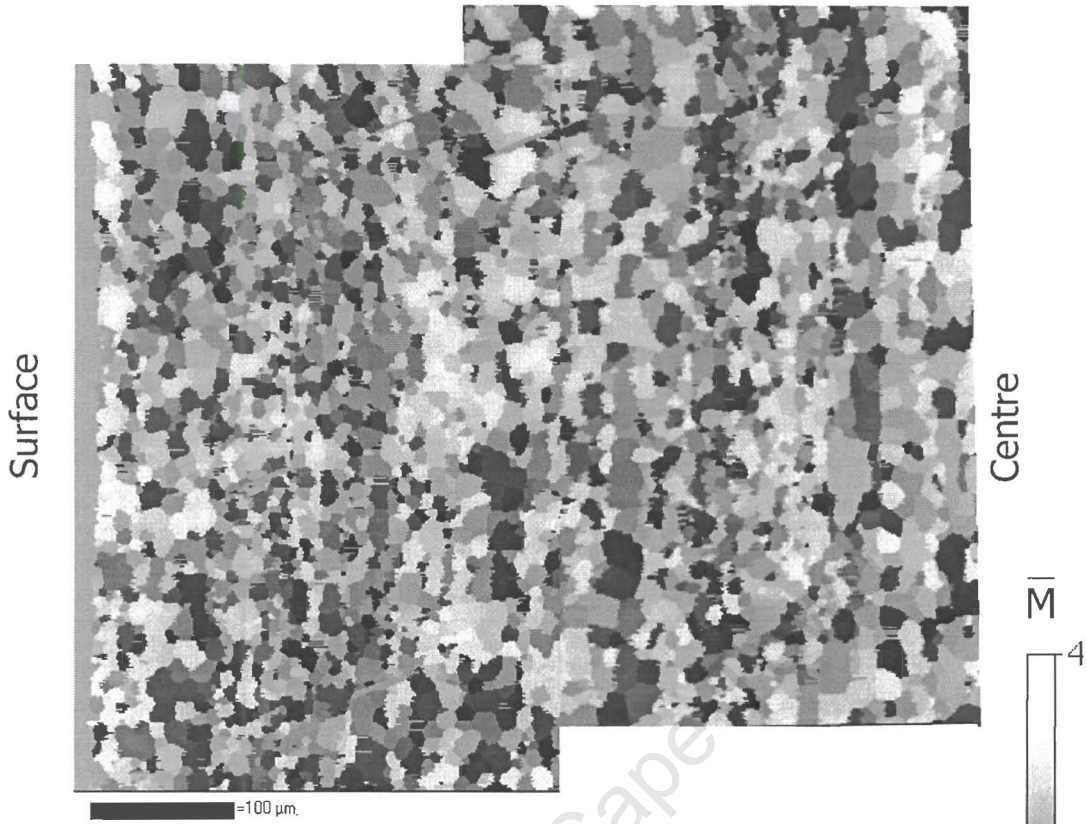

3.d. C800s